The Spherical X-ray Wave Focusing by a Bent Crystal in the Johann Scheme

T. Tchen

Moscow State Academy of Fine Chemical Technology, Moscow, Russia
e-mail: docent65@mtu-net.ru
Received April 28, 2001

Abstract—The focusing of a spherical X-ray beam during the Bragg reflection from a bent crystal in the Johann scheme is considered. It is demonstrated that, with an allowance for the spherical aberration of the beam, the wave intensity in the focus is determined by the square modulus of Airy's function. © *2001 MAIK "Nauka/Interperiodica".*

X-ray radiation focusing according to the Johann scheme [1] is one of the most widely known and attractive methods of obtaining high-intensity beams. A special feature in this scheme is that the reflecting planes of a bent crystal at any point make the same angle with plane harmonics of the incident spherical wave. If no special measures for collimating the beam are taken, the spherical aberration of the reflected (Bragg diffraction) rays may be very significant.

In this study, the Bragg focusing of a spherical X-ray wave by a bent crystal in the Johann scheme is considered (by analogy with the previous analysis [2]) within the framework of the geometric optics (see figure). It is assumed that the diffraction reflection has a coherent elastic character, that is, $\mathbf{k}_0 + \mathbf{h} = \mathbf{k}_h$ and $\mathbf{k}_h^2 = \mathbf{k}_0^2 = k^2$. The reciprocal lattice vector $\mathbf{h}$ of the bent crystal can be presented as $\mathbf{h}(h_x, h_y, h_z) = \mathbf{h}_0 - \nabla(\mathbf{h}_0\mathbf{u})$, where $\mathbf{h}_0$ is the reciprocal lattice vector of the nonbent crystal, $h_0 = 2k\sin\theta$, θ is the Bragg angle, $\mathbf{u}(-xz/R_x, -yz/R_y \approx 0, x^2/2R_x + y^2/2R_y \approx x^2/2R_x)$.

Taking into account all terms proportional to x^2, where x is the coordinate of the point of incidence of an arbitrary beam in the X axis, we obtain the following expressions for the direction cosines of the wavevector $\mathbf{k}_0$:

$$\gamma_{0x} = \sin\varphi_0 + \frac{x}{L_0}\cos^2\varphi_0 - \frac{x^2\cos^2\varphi_0}{L_0^2}\sin\varphi_0$$
$$- \frac{x^2\sin\varphi_0\cos\varphi_0}{2L_0^2}\left(\cos\varphi_0 - \frac{L_0}{R_x}\right), \tag{1}$$

$$\gamma_{0y} = \frac{y}{L_0}\left(1 - \frac{x\sin\varphi_0}{L_0} - \frac{x^2\cos\varphi_0}{2L_0^2}\left(\cos\varphi_0 - \frac{L_0}{R_x}\right)\right) = 0,$$

$$\gamma_{0z} = -\cos\varphi_0 + \frac{x}{L_0}\sin\varphi_0\cos\varphi_0$$
$$+ \frac{x^2}{2R_xL_0} - \frac{x^2}{L_0^2}\sin^2\varphi_0\cos\varphi_0 + \frac{x^2\cos^2\varphi_0}{2L_0^2}\left(\cos\varphi_0 - \frac{L_0}{R_x}\right),$$

$$h_x = -2k\sin\theta(x\cos\Psi/R_x + \sin\Psi),$$

$$h_y = -2k\sin\theta\cos\Psi y/R_y \approx 0,$$

$$h_z = 2k\sin\theta(\cos\Psi - \sin\Psi x/R_x),$$

where Ψ is the sloping angle of the reflecting planes relative to the crystal surface. Note that the radiation focusing in the Johann scheme is one-dimensional
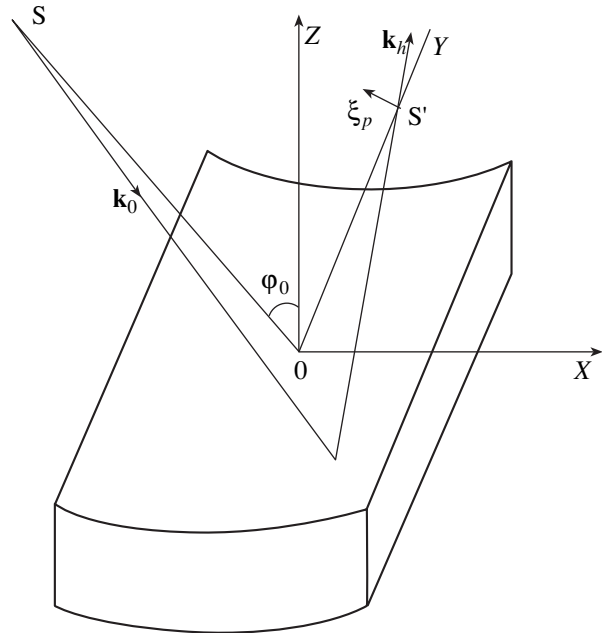

Figure.

$(R_y \gg R_x)$; that is, it takes place in the sagittal plane $Y = 0$.

Considering the case of a symmetric diffraction $(\Psi = 0, \varphi_0 = \pi/2 - \theta)$, we obtain the following relationship for an arbitrary distance L_0 from the source of the spherical wave to the crystal:

$$\Delta\theta = \left| -\frac{x}{R_x} + \frac{x\sin\theta}{L_0} - \frac{x^2(2\sin^2\theta - 1)}{2R_x L_0 \cos\theta} - \frac{x^2\sin\theta\cos\theta}{L_0^2} \right.$$
$$\left. + \frac{x^2\sin\theta}{2R_x^2\cos\theta} + \frac{x^2\sin^2\theta}{2L_0^2\cos\theta}\left(\sin\theta - \frac{L_0}{R_x}\right) \right|, \quad (2)$$

where $\Delta\theta = |\chi_{hr}|/\sin 2\theta$ is the halfwidth of the Bragg reflection and χ_{hr} is the X-ray polarizability. When $L_0 \neq R_x\sin\theta$, we may ignore the spherical aberration. Then, rejecting the terms quadratic in x in relationship (2), we obtain the effective size x_{eff} of the region on the crystal surface in which the partial ray does not spread outside the boundaries of the total reflection region:

$$x_{eff} = \Delta\theta\left|\sin\theta/L_0 - 1/R_x\right|^{-1}, \quad L_0 \neq R_x\sin\theta. \quad (3)$$

In the Johann scheme, when $L_0 = R_x\sin\theta$, we obtain

$$x_{eff}^{Johann} = R_x\sqrt{2\Delta\theta\tan\theta}, \quad L_0 = R_x\sin\theta. \quad (4)$$

Comparing Eqs. (3) and (4), we see that the Johann scheme provides for a gain in the beam-gathering power in comparison to the other schemes, reaching up to 2–3 orders of magnitude since $x_{eff}^{Johann} \sim (\Delta\theta)^{1/2}$. However, an increase in the beam-gathering power is accompanied by a growing spherical aberration of the reflected rays. Estimates of the beam intensity drop at the focal point, related to the spherical aberration in the Johann scheme, and yield a factor of $\sim 10^2$ for the (220) reflection of the CuK_α radiation from a silicon crystal bent with a radius of $R_x \cong 1$ m.

Applying the Huygens–Fresnel principle applied to the X-ray diffraction and expanding the phase of the spherical wave to terms on the order of $\sim x^3$, we obtain an expression for the diffracted wave amplitude $E_h(\xi_p)$ at the focal point

$$E_h(\xi_p) \sim \frac{2\sqrt{\pi}}{(3A_2)^{1/3}}\Phi\left(\frac{A_1}{\{3A_2\}^{1/3}}\right), \quad (5)$$

where

$$\Phi(t) = (\sqrt{\pi})^{-1}\int_0^{+\infty}\cos\left(\frac{u^3}{3} + ut\right)du$$

$$= (2\sqrt{\pi})^{-1}\int_{-\infty}^{\infty}\exp\{i(ut + u^3/3)\}du$$

is the Airy's function and

$$A_1 = -k\xi_p/R_x, \quad A_2 = -k\cos\theta/2R_x^2 < 0.$$

The diffracted wave intensity $I_n(\xi_p) = |E_h(\xi_p)|^2$ at the focal point turns zero for $t_{min} = -2.33811$ (i.e., at the Airy's function zero). The Airy's function $\Phi(t)$ exhibits an oscillatory character for $t < 0$ and monotonically decreases at $t > 0$. According to formula (5), an allowance for the spherical aberration in the Johann scheme leads to a mismatch of the geometric focus ($\xi_p = 0$) and the point of maximum intensity of the focused wave. The greatest peak of the Airy's function ($\Phi = 0.9494$) is attained at $t_{max} = -1.02$. For the (220) reflection of the CuK_α radiation from a silicon crystal bent with a radius of $R_x \cong 1$ m, the coordinate of the point of maximum intensity of the focused wave is $\xi_p^{max} = -0.1$ μm. Taking into account that $\Phi(-2.34) = -0.0024$ and $\Phi(4.00) = 0.0016866$, we obtain an estimate $\Delta\xi \approx 0.6$ μm of the spatial width of the beam intensity maximum (for the same parameters as above). The focus width at half intensity is $\gtrsim 0.1$ μm. Calculation of the diffraction broadening (with neglect of the spherical aberration) by the formula $\Delta\xi = \lambda R_x/x_{eff}$ (taken from [3, 4]) yields $\Delta\xi \approx 1.5 \times 10^{-2}$ μm. Note that an expression for the diffracted wave intensity at the focus $I_h \sim (\sin t/t)^2$ derived in [3, 4] did not take into account the spherical aberration. Moreover, the phase of the incident spherical wave was expressed in a parabolic approximation, and it was assumed that the size x_{eff} of the total reflection region on the crystal surface is limited by a certain value above which the effect of aberration on the focusing can be ignored.

Thus, we have demonstrated that an increase in the beam-gathering power achieved in the Johann scheme is accompanied by the growth of spherical aberration of the diffracted beam. The analytical expression derived above for the intensity distribution at the focal point differs from that derived previously within the framework of the Bragg focusing and takes into account the spherical aberration effect.

REFERENCES

1. H. Johann, Z. Phys. **60**, 185 (1931).

2. T. Chen, V. A. Bushuev, and R. N. Kuz'min, Zh. Tekh. Fiz. **60** (10), 60 (1990) [Sov. Phys. Tech. Phys. **35**, 1148 (1990)].

3. K. T. Gabrielyan, F. N. Chukhovskiĭ, and Z. G. Pinsker, Zh. Tekh. Fiz. **50** (1), 3 (1980) [Sov. Phys. Tech. Phys. **25**, 1 (1980)].

4. K. T. Gabrielyan, F. N. Chukhovskiĭ, and D. I. Piskunov, Zh. Éksp. Teor. Fiz. **96** (3), 834 (1989) [Sov. Phys. JETP **69**, 474 (1989)].

Translated by P. Pozdeev

The Generalized Chester–Whitham Invariant

A. V. Omel'chenko

St. Petersburg State University, St. Petersburg, Russia
e-mail: vmu@peterlink.ru
Received May 28, 2001

Abstract—The problem of interaction of strong and weak discontinuities is solved in the general case for a system of quasilinear hyperbolic equations with two independent variables. It is proved that the product of the left eigenvector of the system by a derivative of the vector function in a strong discontinuity direction remains constant during the interaction. Examples of using this fact in solving the problems of gasdynamics are presented. © 2001 MAIK "Nauka/Interperiodica".

Let us consider a system of quasilinear hyperbolic equations with two independent variables (x, t) that is hyperbolic with respect to variable t in some simply connected domain Ψ of variables (x, t, u) and can be reduced to a normal form of

$$\frac{\partial u}{\partial t} + A\frac{\partial u}{\partial x} = b. \tag{1}$$

Here, $u = u([N])$ is the vector of unknown functions, N is the index space of dimension $|N| = n$, and $A = A[N, N]$ and $b = b[N]$ are the known matrix and vector depending on the vector u and the independent variables x and t. Multiplying Eq. (1) on the left by the left eigenvector $L^{(k)}$ of the matrix A, we obtain a characteristic system equivalent to Eq. (1):

$$L^{(k)}V + \lambda_k L^{(k)}U = L^{(k)}b, \quad k = 1, \ldots, n. \tag{2}$$

Here, $V = \partial u/\partial t$, $U = \partial u/\partial x$, and λ_k is the eigenvalue of the matrix A corresponding to $L^{(k)}$. Below, we assume that the eigenvalues $\lambda_1, \ldots, \lambda_n$ of the matrix A are real and different at any point of the domain Ψ. This implies that we restrict the consideration to a system of equations hyperbolic in the narrow sense [1].

Under certain boundary conditions, system (1) has no continuously differentiable solutions $u(x, t)$. In practice, this implies that the domain Ω of variables (x, t) contains one or several lines of discontinuity of the function $u(x, t)$ (lines of strong discontinuity) or its derivative (lines of weak discontinuity). Let us assume that the domain under consideration contains a single strong discontinuity line (see figure), the trajectory of which is described by the equation $x'(t) = D$. In this case, a solution to system (1) can be constructed by dividing domain Ω into two subdomains Ω_1 and Ω_2 (separated by the strong discontinuity line) and writing (in terms of the conservation laws [1] corresponding to

Eq. (1)) the so-called dynamic compatibility condition on the discontinuity line $x(t)$:

$$D[u] = [\psi(u, x, t)], \quad [u] = u_2 - u_1, \quad D = x'(t),$$

which relates the left ($u_1 \in \Omega_1$) and right ($u_2 \in \Omega_2$) limiting values of the solution on the strong discontinuity line. It was demonstrated (see, e.g., [2]) that the solution constructed in this way satisfies the uniqueness condition and the condition of continuous dependence on the initial values, provided that the following inequalities are valid on the strong discontinuity line $x(t)$:

$$\lambda_k(u_1(t), x(t), t) > D > \lambda_k(u_2(t), x(t), t),$$
$$\lambda_{k-1}(u_1(t), x(t), t) > D > \lambda_{k+1}(u_2(t), x(t), t). \tag{3}$$

The number k for which conditions (3) are satisfied is called the discontinuity index. For certainty, we will
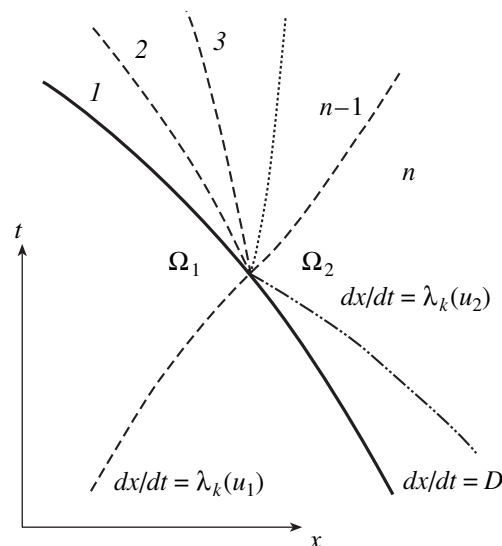
A schematic diagram illustrating the interaction of a strong discontinuity with index 1 and a weak counterdiscontinuity with index k.

assume below that the discontinuity index is $k = 1$. Conditions (3) imply that $n + 1$ characteristics come into any strong point discontinuity point with index 1 (including n characteristics lying in subdomain Ω_1, corresponding to $\lambda_k(u_1(t), x(t), t)$ with $k = 1, \ldots, n$, and a single characteristic from Ω_2 corresponding to $\lambda_1(u_2(t), x(t), t)$), while $n - 1$ characteristics go out of this point, which correspond to $\lambda_k(u_2(t), x(t), t)$ with $k = 2, \ldots, n$.

Now, let us assume that domain Ω contains, in addition to the above strong discontinuity, a weak discontinuity as well. The weak discontinuity line coincides with one of the characteristics of system (2), which implies that a number exists among $k \in (1, \ldots, n)$ such that $dx/dt = \lambda_k$. By analogy with the case of a strong discontinuity, this line will be referred to as a weak discontinuity line with index k.

If a weak discontinuity with index k at $t = 0$ belongs to the subdomain Ω_1 (the so-called counterdiscontinuity with index k), this line contains a point of intersection $(x_1, t_1) \in \Omega$ with a strong discontinuity line (see figure) for any $k = 1, \ldots, n$. As a result of this interaction, there will appear $n - 1$ weak discontinuities with index k ($k = 2, \ldots, n$) in subdomain Ω_2, which go out of the (x_1, t_1) point and coincide in direction with the characteristics corresponding to $\lambda_k(u_2(t), x(t), t)$ ($k = 2, \ldots, n$). In addition, the curvature of the strong discontinuity line will exhibit a jumplike change. Let us introduce the vectors $V^{(n)}$, $U^{(n)}$ and $V^{(1)}$, $U^{(1)}$ of derivatives behind the strong discontinuity in the zones (n) and (1) in front of and behind the interaction point, respectively (see figure), and the vectors $[V]_w = V^{(n)} - V^{(1)}$ and $[U]_w = U^{(n)} - U^{(1)}$ of the derivative discontinuity behind the strong discontinuity.

Lemma. In case when a strong discontinuity with index 1 interacts with a weak counterdiscontinuity, the vectors $[V]_w$ and $[U]_w$ of the derivative discontinuity behind the strong discontinuity are orthogonal to an eigenvector $L^{(1)}$ constructed for $u = u_2$ from subdomain Ω_2:

$$L^{(1)}[V]_w = 0, \quad L^{(1)}[U]_w = 0. \tag{4}$$

Proof. Let $[V]_k = V^{(k+1)} - V^{(k)}$ and $[U]_k = U^{(k+1)} - U^{(k)}$ be the discontinuities of derivatives V and U on a weak discontinuity with index k ($k = 2, \ldots, n$) going out of the interaction point. The difference between derivatives $V^{(n)}$, $U^{(n)}$ and $V^{(1)}$, $U^{(1)}$ in the zones (n) and (1) in front of and behind the interaction point, respectively, is related to the magnitudes $[V]_k$ and $[U]_k$ of the derivative

discontinuities on the outgoing weak discontinuities by the following obvious relationship:

$$[V]_w = V^{(n)} - V^{(1)} = \sum_{k=1}^{n-1} V^{(k+1)} - V^{(k)} = \sum_{k=1}^{n-1} [V]_k,$$

$$[U]_w = U^{(n)} - U^{(1)} = \sum_{k=1}^{n-1} U^{(k+1)} - U^{(k)} = \sum_{k=1}^{n-1} [U]_k. \tag{5}$$

It was proved in [1] that linear combinations of the types $L^{(m)}V^{(k)}$ and $L^{(m)}U^{(k)}$ ($m \neq k$) remain unchanged on passing through a weak discontinuity with index k:

$$L^{(m)}[V]_k = 0, \quad L^{(m)}[U]_k = 0, \quad m \neq k. \tag{6}$$

Multiplying Eqs. (5) on the left by $L^{(1)}$ and taking into account Eq. (6), we obtain the required result (4).

Theorem. The product of a left eigenvector $L^{(1)}$ by the derivative du_2/dt of the vector function u_2 with respect to t in a strong discontinuity direction remains constant during the interaction of the strong discontinuity with a weak counterdiscontinuity, being equal to

$$L^{(1)}\frac{du^{(n)}}{dt} = L^{(1)}\frac{du^{(1)}}{dt} =: L^{(1)}\frac{du_2}{dw} = L^{(1)}b. \tag{7}$$

Proof. Consider the discontinuity line $x(t)$ of the vector function $u(x, t)$, described by the equation $dx/dt = D$. Multiplying the second equation in (4) by D, adding the two equations, and taking into account that the sum $\partial u/\partial t + D\partial u/\partial x$ equals the derivative du/dt of the vector function u with respect to t in the strong discontinuity direction, we obtain

$$L^{(1)}\frac{du^{(n)}}{dt} - L^{(1)}\frac{du^{(1)}}{dt} = 0.$$

This relationship indicates that the derivative of the vector function u in the strong discontinuity direction, multiplied on the left by $L^{(1)}$ does not change upon the interaction of the strong discontinuity with an arbitrary weak counterdiscontinuity:

$$L^{(1)}\frac{du^{(n)}}{dt} = L^{(1)}\frac{du^{(1)}}{dt} = \text{const} =: C. \tag{8}$$

Now we only have to determine the constant in the right-hand part of this relationship. For this purpose, let us consider a characteristic of the first family coming to the interaction point and descried by the equation $dx/dt = \lambda_1(u_2(t), x(t), t)$ (see figure). Since this characteristic is lying in the zone (n) corresponding to $u = u^{(n)}$, the conditions on this characteristic are as follows:

$$L^{(1)}V^{(n)} + \lambda_1 L^{(1)}U^{(n)} = L^{(1)}b. \tag{9}$$

Subtracting (9) from (8), we obtain in the left-hand part

$$L^{(1)}V^{(n)} + DL^{(1)}U^{(n)} - L^{(1)}V^{(n)} - \lambda_1 L^{(1)}U(n)$$

$$= (D - \lambda_1)(L^{(1)}U^{(n)} - L^{(1)}U^{(n)}) \equiv 0.$$

Therefore, $C = L^{(1)}b$ that solves the task.

Apparently, a particular variant of formula (7) was originally obtained by Whitham [3, 4] based on an analysis of the results of Chester [5] and Chisnell [6, 7]. Chester [5] studied a problem concerning the decay of a discontinuity in a channel with a jump in the cross section area, considering the case when the jump is so small that the formulas can be linearized. As a result of this linearization, Chester obtained the following relationship between a small change in the relative velocity $M = D/a$ of a shock wave and a change in the tube cross section area A:

$$d\ln A = -\frac{dM^2}{(M^2 - 1)k(M)}, \qquad (10)$$

where

$$k(M) = 2\left[\left(1 + (1 - \varepsilon)\frac{1 - g^2}{g}\right)\left(2g + 1 + \frac{1}{M^2}\right)\right]^{-1},$$

$$g(M) = \frac{(\gamma - 1)M^2 + 2}{2\gamma M^2 - (\gamma - 1)}.$$

Whitham [3] established that the same result can be obtained by writing a condition for the characteristic of the second family in the cocurrent flow behind the shock wave,

$$d\ln p_2 + \frac{\gamma}{a_2}du_2 + \frac{\gamma u_2}{u_2 + a_2}d\ln A = 0$$

and replacing p_2, u_2, a_2 by their expressions through M derived from conditions on the shock wave. For a shock wave propagating in a resting gas with the parameters p_1, u_1, a_1, these conditions can be written as

$$\frac{p_2}{p_1} = (1 + \varepsilon)M^2 - \varepsilon, \quad \frac{u_2}{a_1} = (1 - \varepsilon)\left(M - \frac{1}{M}\right),$$

$$\frac{a_2}{a_1} = \sqrt{\left[(1 + \varepsilon) - \frac{\varepsilon}{M^2}\right][(1 - \varepsilon) + \varepsilon M^2]}.$$

Whitham called this approach the characteristic rule [3]. The results obtained above indicate that this rule follows immediately from a solution of the problem of interaction of a strong discontinuity with a weak counterdiscontinuity.

Chisnell [6] suggested using formula (10) for describing the trajectory of a shock wave propagating in a resting gas in a channel of variable cross section. In the Chisnell theory, a channel with a continuously varying cross section was approximated by a sequence of cylindrical channels adjoining each other, and the transition of a shock wave from one cylindrical part to another was described by formula (10). The Chisnell theory ignores additional interaction of the secondary waves reflected from the channel walls and overtaking the primary shock wave. However, a comparison of the approximate analytical solution based on formula (10) with the exact numerical solution shows excellent coincidence.

Based on relationship (7) derived above, which can be called the generalized Chester–Whitham formula, it is possible to use an analogous approach in solving a broad class of problems involving the interaction of strong discontinuities. For example, Eq. (7) can be used in the stationary gasdynamics for solving the problems related to the interaction of shock waves with the Prandtl–Meyer isentropic waves [8] and shear bands [9]; in the stationary gasdynamics, this relationship can be used for solving the problems related to the interference of shock waves with the Riemann waves.

REFERENCES

1. B. L. Rozhdestvenskiĭ and N. N. Yanenko, *Systems of Quasilinear Equations and Their Applications to Gas Dynamics* (Nauka, Moscow, 1968).
2. P. D. Lax, Commun. Pure Appl. Math. **10**, 537 (1957).
3. G. B. Whitham, *Linear and Nonlinear Waves* (Wiley, New York, 1974; Mir, Moscow, 1977).
4. G. B. Whitham, J. Fluid Mech. **4**, 337 (1958).
5. B. Chester, Mekhanika, No. 6, 76 (1954).
6. R. F. Chisnell, J. Fluid Mech. **2**, 286 (1957).
7. R. F. Chisnell, Proc. R. Soc. London **232**, 350 (1955).
8. V. R. Meshkov, A. V. Omel'chenko, V. N. Uskov, and M. V. Chernyshov, Prikl. Mekh. Tekh. Fiz. **42** (2001) (in press).
9. A. L. Adrianov, *On a Model of Flow behind a Curvilinear Shock Wave Front*, Available from VINITI, No. 3357, B-97 (1997).

Translated by P. Pozdeev

Anomalous Dielectric Properties of Amorphous Lead Titanate

L. N. Korotkov, S. A. Gridnev, A. A. Khodorov,
S. A. Konstantinov, and S. V. Kashirskiĭ

Voronezh State Technical University, Voronezh, Russia
e-mail: korotkov@nsl.vstu.ac.ru
Received June 4, 2001

Abstract—We studied the effect of a thermal treatment below the crystallization temperature on the dielectric properties of amorphous lead titanate obtained by melt quenching and containing silicon impurity. Anomalies in the permittivity and dielectric losses were observed at 200°C and at a temperature (463°C) corresponding to the ferroelectric phase transition in the crystallized material. The magnitude and shape of these anomalies depend on the thermal prehistory of a sample. The features in the dielectric properties are explained by the presence of a relict polar phase region interacting with the mobile charge carriers. © *2001 MAIK "Nauka/Interperiodica".*

Crystalline lead titanate ($PbTiO_3$) is a well-known ferroelectric compound with a perovskite structure. Possessing unique physical properties, this material has been drawing the attention of researchers for a long time, including both fundamental investigations and numerous practical applications [1, 2]. While the physical properties of $PbTiO_3$ single crystals and polycrystalline samples were thoroughly studied [1, 2], our knowledge of the properties of this compound in the amorphous state is not as exhaustive. At present, only a limited number of publications are available that are devoted to noncrystalline lead titanate. In this context, our purpose was to study the dielectric properties of amorphous $PbTiO_3$ and determine the role of the thermal prehistory of a sample.

The samples for investigation were prepared in the form of plates cut to size $\sim 3 \times 3 \times 0.2$ mm from a melt-spun material. To this end, a powder of synthesized lead titanate was melted in a quartz ampule at a temperature of 1300°C and quenched on a rapidly rotating copper disk. An analysis of the chemical composition of the quenched samples using an electron-probe microanalyzer of the JXA-840 type showed the presence of a silicon impurity (about 6.85 at. %). The X-ray diffraction measurements using graphite-monochromated CoK_α radiation confirmed the amorphous state of the base material. The crystallization temperature determined by DTA was $T_{cr} \approx 590$°C.

The dielectric measurements were performed on the $PbTiO_3$ plates with platinum electrodes pressed against the side surfaces. The samples were placed into a thermostat controlling the temperature in a range from 20 to 662°C with an accuracy no worse than ±1°C. The temperature variation of the real (ε') and imaginary (ε'') parts of the complex permittivity was monitored using a capacitive bridge (E7-12) operating at a frequency of 1 MHz and a probing field amplitude of ≈0.25 V/cm.

All measurements were taken in a cyclic mode at a sample heating rate of ~2 K/min. A special feature of the experiment was that every other cycle reached a greater maximum heating temperature, at which the material was annealed in air for ~8 h.

The results of the dielectric measurements are presented in Figs. 1 and 2. As one can see judging by the $\varepsilon'(T)$ and $\varepsilon''(T)$ curves, the temperature range studied
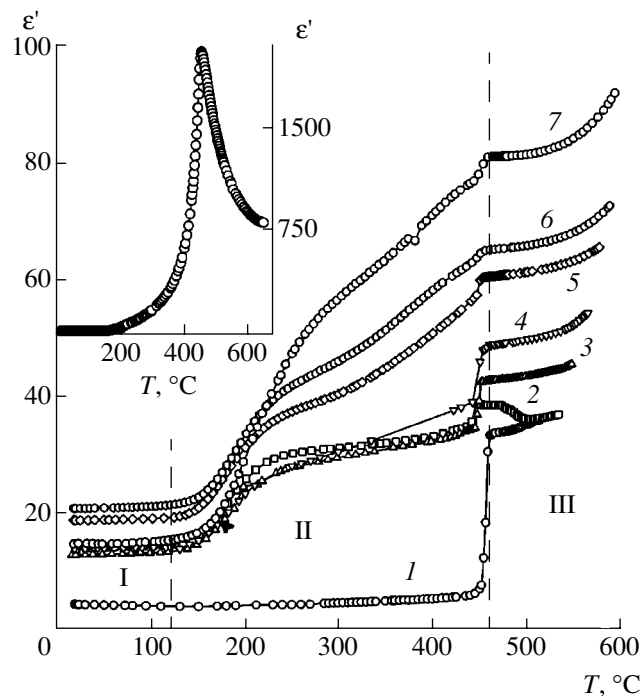

Fig. 1. The temperature variation of ε' in amorphous lead titanate (*1*) in the initial state and after thermal annealing for ~8 h at T = 513 (*2*), 532 (*3*), 544 (*4*), 563 (*5*), 575 (*5*), 587 (*6*), 592°C (*7*). The inset shows the $\varepsilon'(T)$ curve for a crystalline lead titanate sample.

can be subdivided into three regions showing a different behavior of both real and imaginary components of the complex permittivity.

In region I (20°C ≤ T ≤ 120°C), both the ε' and ε" values show a relatively weak variation with increasing temperature. Therefore, thermal annealing in this temperature interval leads to an insignificant increase in the permittivity and dielectric losses. In region II (120°C ≤ T ≤ 460°C), all ε' curves (except those obtained during the first heating) exhibit a significant increase with the temperature (Fig. 1). The rate of this growth also markedly increases in each subsequent cycle of the thermal treatment.

In the same region II, the curves of ε"(T) exhibit two maxima (Fig. 2, curves *2–7*). The position of the first peak (~200°C) weakly depends on the thermal prehistory, while both the position and shape of the second (significantly asymmetric) peak occurring between 350 and 420°C significantly change in each cycle of measurements. The thermal treatment at $T < T_{cr}$ gives rise to increase both anomalies in ε". As a result, the high-temperature peak shifts leftward and partly overlaps with the low-temperature peak. At the same time, the right-hand edge of the high-temperature peak appears as "fixed" at a strictly determined temperature (~460°C), where all the ε"(T) curves exhibit a sharp minimum. Note that the ε'(T) curves also show jumplike anomalies at this temperature.

In region III ($T > 460°C$), the rate of increase in ε' with the temperature changes (Fig. 1) to become approximately the same in all measuring cycles irrespective of the annealing temperature (provided that the maximum temperature does not exceed T_{cr}).

Thus, we may assert that amorphous $PbTiO_3$ is characterized by a significant difference in behavior of ε'(T) and ε"(T) at temperature above and below a certain point T^* coinciding with the temperature of the ferroelectric phase transition (T_C) in a crystalline material (see the inset in Fig. 1). Apparently, this difference reflects certain internal transformation of the object studied. For this reason, the anomalies in the ε'(T) and ε"(T) observed in the vicinity of $T = T^*$ are naturally attributed to some local structural transitions in the regions where a relict crystalline structure of $PbTiO_3$ was retained. According to the data of small-angle X-ray scattering (SAXS) and extended X-ray absorption fine structure (EXAFS) [3], such regions (with a size of ~15 nm) actually exist in the amorphous lead titanate obtained by quenching from the melt. According to [4], this approximately corresponds to a minimum crystal grain size (~10 nm), for which a transition to the polar phase still takes place below T_C.

At the same time, the contribution of the polar phase regions to the permittivity is quite small. This is evidenced by a relatively small ε' value (compared to that in the crystalline sample) and by a significant difference in shape of the anomaly at T^* observed for samples in the amorphous and crystalline states (compare,
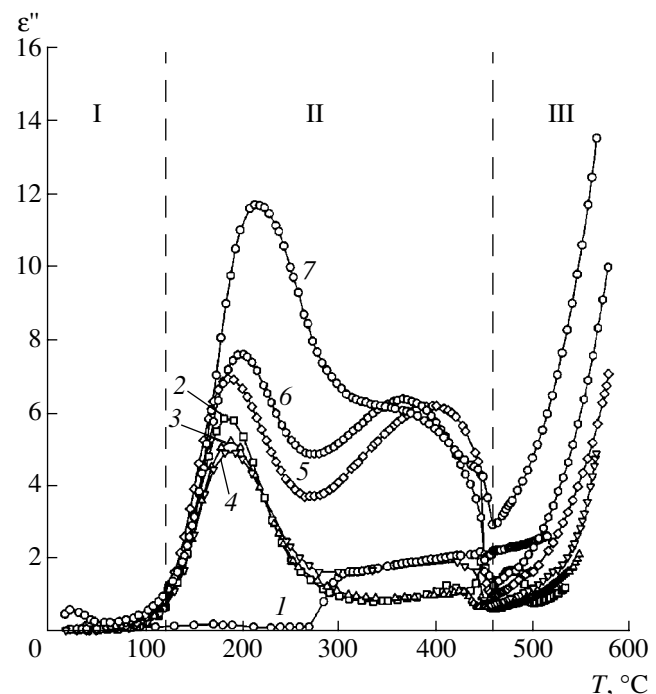

Fig. 2. The temperature variation of ε" in amorphous lead titanate (*1*) in the initial state and after thermal annealing for ~5 h at T = 513 (*2*), 532 (*3*), 544 (*4*), 563 (*5*), 575 (*5*), 587 (*6*), 592°C (*7*).

e.g., curve *1* and the inset in Fig. 1). The amorphous samples show a jumplike increase in ε' in the vicinity of T^*, which is especially clearly pronounced in the first heating cycle. In contrast, the crystalline material exhibits an ε' peak characteristic of the intrinsic ferroelectric phase transition.

The special shape of the dielectric anomaly observed in amorphous samples is probably related to a phenomenon of the internal field switch-off caused by vanishing of the spontaneous polarization in the crystal-like regions at temperatures above T^*. The jump in ε' decreases after each heating cycle, which is naturally attributed to enhanced screening of the polar regions by mobile charge carriers. Indeed, the concentration of charge carriers seems to increase as a result of annealing, as indicated by a considerable growth in the electric conductivity of $PbTiO_3$ after thermal treatment [5]. Evidently, an increase in the concentration of mobile charge carriers must lead to a "general" increase in both permittivity and losses [6], and this actually takes place (see Figs. 1 and 2).

As indicated above, the maximum rate of increase in ε' is observed in region II. Remarkably, this steep growth in ε' coincides with the maximum of ε" near 200°C. An analogous maximum was previously reported for single crystal lead titanate in [7], where it was demonstrated that the peak appeared due to the presence of weakly bound electrons localized on dou-

bly charged centers devastated on heating the sample above ~200°C.

Apparently, a similar situation takes place in the amorphous material as well. In this case, a significant increase in the concentration of carriers must lead to their accumulation near the polar regions and result in the screening of these regions. The growth of the dielectric losses and the leftward shift of the loss peak after each heating cycle can be explained by the fact that the interaction between the mobile carriers and the polar regions gradually decreases with increasing screening of the latter.

Thus, our experiments revealed a significant influence of the thermal prehistory on the dielectric properties of amorphous lead titanate. The analysis shows that the anomalies observed in the temperature dependence of the real and imaginary parts of the complex permittivity are related to the presence of relict polar phase regions in the initial material and the interaction of these regions with mobile charge carriers.

REFERENCES

1. E. G. Fesenko, *Perovskite Family and Ferroelectricity* (Atomizdat, Moscow, 1972).

2. Yu. N. Venevtsev, E. D. Politova, and S. A. Ivanov, *Ferroelectrics and Antiferroelectrics in the Barium Titanate Family* (Khimiya, Moscow, 1985).

3. T. Nakamura, M. Takashige, H. Terauchi, *et al.*, Jpn. J. Appl. Phys. **23** (10), P1265 (1984).

4. S. Chattopadhyay, P. Ayyub, V. R. Palkar, *et al.*, Phys. Rev. B **52** (18), 13 177 (1995).

5. L. N. Korotkov, S. A. Gridnev, S. A. Konstantinov, *et al.*, in *Abstract Book of Third Seminar on Relaxor Ferroelectrics, Dubna, 2000*, p. 44.

6. N. F. Mott and E. A. Davis, *Electronic Processes in Non-Crystalline Materials* (Clarendon Press, Oxford, 1971; Mir, Moscow, 1974).

7. L. A. Barabanova, V. G. Gavrilyachenko, E. S. Tsikhotskiĭ, *et al.*, Izv. Akad. Nauk SSSR, Neorg. Mater. **15** (9), 1612 (1979).

Translated by P. Pozdeev

A Dynamic Bistability
in Two-Layer Magnetically-Coupled Films

D. I. Sementsov* and A. M. Shutyĭ

Ul'yanovsk State University, Ul'yanovsk, Russia
* e-mail: sdi@sdi.ulsu.ru
Received May 15, 2001

Abstract—The dynamic behavior of magnetic moments in a two-layer magnetically coupled film system was studied in the region of ferromagnetic resonance with large amplitudes of the precession angle. The system exhibits manifestations characteristic of the nonlinear phenomena, including (i) a shift in the resonance frequency with increasing microwave field strength and (ii) the existence of dynamic bistability regions with respect to the microwave frequency and the magnetizing field strength. © *2001 MAIK "Nauka/Interperiodica".*

Introduction. The interaction of a high-frequency high-power radiation with magnetically ordered crystals under ferromagnetic resonance (FMR) conditions is accompanied by a number of effects related to a sharp increase in the amplitude of oscillations of the magnetization [1–5]. These manifestations include bistability and the related hysteresis behavior in the absorbed power as a function of the magnetizing field strength [6–9]. In recent years, increased attention of researchers has been attracted to the resonance properties of multilayer systems comprising alternating layers of ferromagnetic and nonmagnetic metals. These systems, exhibiting various types of magnetic ordering in the component layers, show various types of the magnetic behavior [10, 11].

We have studied the features of nonlinear FMR in a magnetically coupled system comprising two layers of a ferromagnetic metal separated by a thin nonmagnetic spacer ensuring collinear orientation of the magnetic moments. An analysis of the magnetic behavior of this system revealed manifestations characteristic of the nonlinear phenomena, including (i) a shift in the resonance frequencies of the ferromagnetic layers with increasing microwave field strength and (ii) the existence of bistability regions in the amplitude of magnetic moment oscillations as a function of the microwave frequency and the magnetizing field strength.

System description. Let us consider a system of two magnetically coupled layers magnetized in the *xy* plane. Each layer is characterized by a thickness d_i, a magnetization $\mathbf{M}_i$, a plane uniaxial anisotropy with a constant K_i, and an easy axis coinciding with the *y* axis. The external magnetizing field vector **H** is lying in the film plane and oriented at an angle α relative to the *y* axis. The alternating microwave magnetic field **h**(*t*) is linearly polarized in the film plane and is perpendicular to the magnetizing field direction.

A solution to the dynamic Landau–Lifshits equation for the magnetically coupled layer system in a linear approximation leads to the following expression for the high-frequency magnetic susceptibility:

$$\chi = (d_1\chi_1 + d_2\chi_2)(d_2 + d_2)^{-1}, \tag{1}$$

$$\chi_i = 4\pi\gamma^2 M_i$$

$$\times \frac{M_i\Delta_{3-i}\cos(\alpha - \varphi_{0i}) - 4\pi\gamma^2 D_i M_{3-i}\cos(\alpha - \varphi_{03-i})}{\Delta_1\Delta_2 - 16\pi^2\gamma^4 D_1 D_2}.$$

Here, γ is the gyromagnetic ratio; $D_i = Ad_{12}M_1M_2/d_i$ is a parameter; $d_{12} = d_1d_2(d_1 + d_2)^{-1}$ is the reduced layer thickness; *A* is the magnetic coupling constant (depending in the general case on the spacer material, thickness, and structure); φ_{0i} is the equilibrium magnetization orientation (for *h* = 0); and Δ_i are the parameters given by the formulas

$$\Delta_i = \omega_{0i}^2 - \omega^2 - 4\pi\gamma^2 D_i + 4\pi i\lambda_i\omega, \tag{2}$$

where λ_i are the damping parameters, ω_{0i} are the resonance frequencies of the individual layers

$$\omega_{0i}^2 = 4\pi M_i\gamma^2[H\cos(\alpha - \varphi_{0i}) + H_{ki}\cos 2\varphi_{0i}], \tag{3}$$

and $H_{ki} = 2K_i/M_i$ are the anisotropic magnetic fields.

Using Eq. (1), we can determine the resonance frequencies of the two-layer system studied. Ignoring the damping ($\lambda_i = 0$), we obtain

$$\omega_{1,2}^2 = \frac{\omega_{01}^2 + \omega_{02}^2}{2} - 2\pi\gamma^2 A M_1 M_2$$

$$\pm \sqrt{\frac{(\omega_{01}^2 - \omega_{02}^2)^2}{4} + 2\pi\gamma^2 A M_1 M_2 \frac{d_1 - d_2}{d_1 + d_2}(\omega_{01}^2 - \omega_{02}^2) + (2\pi\gamma^2 A M_1 M_2)^2}.$$

(4)

As can be seen from this formula, the resonance frequencies of the two-layer system in the absence of interaction between layers ($A = 0$), that is, normal frequencies, coincide with the individual resonance frequencies; for $A \neq 0$, the resonance frequencies shift from these values.

In particular, in the case when the individual resonance frequencies of the two layers coincide ($\omega_{0i} = \omega_0$), the resonance frequencies of the coupled layers are $\omega_1^2 = \omega_0^2$ and $\omega_2^2 = \omega_0^2 - 4\pi\gamma^2 A M_1 M_2$. This allows the coupling constant to be determined if the difference of resonance frequencies is known. Depending on the sign of the coupling constant A, a shift of the resonance frequency ω_2 relative to ω_0 can be either positive or negative.

Results and analysis. The nonlinear effects become significant for a microwave field amplitude close to the threshold value $h_{thr} \cong (\Delta H_i^3 / 4\pi M_i)^{1/2}$, where ΔH_i is the linear resonance linewidth for which the homogeneous precession becomes unstable [3]. The features of the magnetization precession with an allowance for the

nonlinear effects will be considered based on a numerical solution of the dynamic Landau–Lifshits equation. To simplify the analysis, we will assume that $A < 0$ (which corresponds to the case of parallel magnetic moments for the two layers in the equilibrium state at $H = 0$) and that the magnetizing field is directed along the easy axes (i.e., $\alpha = 0$).

The calculation is performed for the values of parameters close to the characteristics of real films of the permalloy type: $\lambda_1 = \lambda_2 = 5 \times 10^7$ s^{-1}; magnetization and anisotropic field in the first film, $4\pi M_1 = 8 \times 10^3$ G and $H_{k1} = 5$ Oe, and those in the second film, $4\pi M_2 = 1.1 \times 10^4$ G and $H_{k2} = 10$ Oe, respectively; $\gamma = 1.76 \times 10^7$ (Oe s)$^{-1}$; film thicknesses $d_1 = d_2 = 0.1$ μm. For these parameters, the nonlinear effects become significantly manifested for the microwave field amplitudes $h \sim 1$ Oe.

Figure 1 shows the frequency dependence of the high-frequency magnetic susceptibility $\tilde{\chi}$ ($M_1 \cos \tilde{\varphi}_1 + M_2 \cos \tilde{\varphi}_2$)/$h$, where $\tilde{\varphi}_i$ are the amplitudes of the angles of stationary magnetic moment oscillations determined for various microwave field amplitudes $h = 0.1, 0.3, 0.5, 0.7$, and 0.9 Oe (curves 1–5, respectively) at the same magnetizing field $H = 0$ and the coupling constant $|A| = 5 \times 10^{-3}$. The dashed curve corresponds to a linearized solution constructed based on (4).
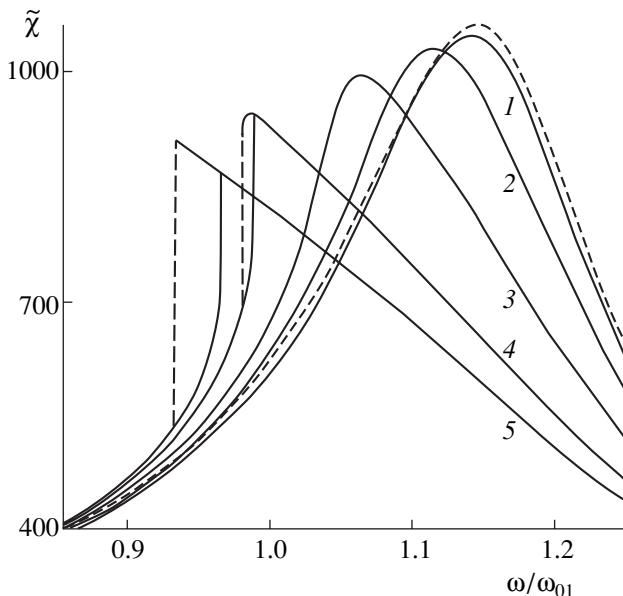
An analysis of the data presented in Fig. 1 shows that the resonance frequencies tend to decrease relative to the linearized solution even for a rather small microwave field strength. As the microwave field strength increases, the nonlinear effects grow: the frequency shift of the resonance peaks becomes more significant and the resonance curves exhibit an increasing asymmetry, which eventually leads to the appearance of a bistability interval. For equal microwave field strengths, the bistability interval is greater for a smaller energy of coupling between the magnetic moments of layers. An increase in the microwave field strength is also accompanied by a decrease in magnitude of the resonance magnetic susceptibility.

For the state with a greater amplitude of the magnetic moment oscillations to be realized in a bistability regime, it is necessary that the initial direction of the magnetization vectors $\mathbf{M}_i$ would be close to the direction of the microwave field, that is, $\varphi_0 \approx \pm\pi/2$. This condition can be satisfied by using an additional magnetizing field directed along the x axis, which is switched off upon application of the microwave field h at $t = 0$. The realization of a dynamic state in the bistability regime

Fig. 1. The frequency dependence of the microwave magnetic susceptibility $\bar{\chi}$ of a two-layer magnetically coupled film system calculated for various microwave field amplitudes $h = 0.1, 0.3, 0.5, 0.7$, and 0.9 Oe (curves 1–5, respectively) at the same magnetizing field ($H = 0$) and the coupling constant $|A| = 5 \times 10^{-3}$. The dashed curve corresponds to a linearized solution.
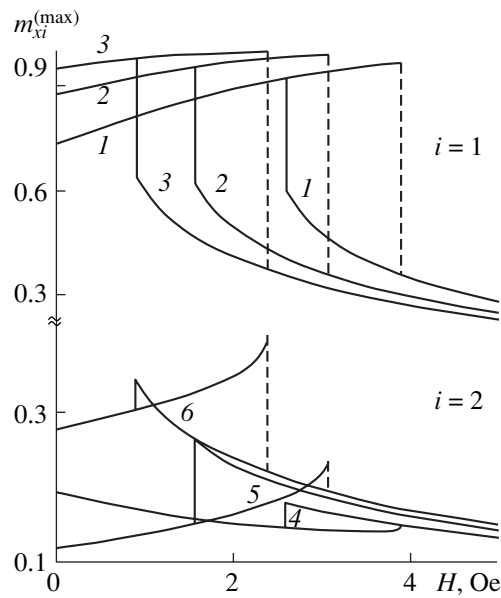
Fig. 2. The plots of the high-frequency magnetization $m_{x2}^{(max)}$ versus the magnetizing field strength H calculated for the same microwave field amplitude $h = 1.5$ Oe and various coupling constants $|A| = 1 \times 10^{-3}$ (curves *1* and *4*), 5×10^{-3} (curves *2* and *5*), and 9×10^{-3} (curves *3* and *6*).

is also affected by the initial phase of the microwave field.

Figure 2 shows the plots of the *x*-component amplitudes of the magnetic moments $m_{xi}^{(max)}$ of the first (curves *1–3*) and second (curves *4–6*) films in the course of a steady-state precession versus the magnetizing field strength H. The cures were calculated for the frequencies $\omega = \omega_{01}$, the microwave field amplitude $h = 1.5$ Oe, and various coupling constants $|A| = 1 \times 10^{-3}$ (curves *1* and *4*), 5×10^{-3} (curves *2* and *5*), and 9×10^{-3} (curves *3* and *6*). As the H value increases, the amplitude of the magnetization oscillations in the film possessing the intrinsic resonance frequency equal to that of the microwave field shows a smooth initial increase followed by a sharp drop, which corresponds to the onset of bistability. This is also manifested in an asymmetry in the shape of the resonance curve relative to the resonance frequency ω_i, which is observed for sufficiently large microwave field amplitudes h. For the second film, the $m_{x2}^{(max)}$ versus H curves show a different behavior. At a small value of the coupling constant $|A|$, the amplitude of the magnetization oscillations slightly decreases with the magnetizing field strength; for large $|A|$ values, $m_{x2}^{(max)}$ initially grows and then (past the

bistability region) begins to decrease. In the region of bistability, the two branches of the $m_{x2}^{(max)}$ versus H curves intersect: there is a magnetizing field strength H_c for which the two stationary dynamic states of the system differ by the amplitude of magnetization oscillations only in the first film. However, this feature in the bistability regime is absent for both very small and very large values of the coupling constant.

The results of the above analysis showed that a system of two magnetically coupled layers with a nonmagnetic spacer providing for a ferromagnetic interaction ($A < 0$) of the magnetic moments of component layers features nonlinear effects leading to a shift in the precession frequency with increasing amplitude of the microwave field and to the appearance of dynamic bistability regions. A strong (severalfold) difference between amplitudes of the magnetic moment precession virtually in the entire region of the dynamic bistability makes this system extremely sensitive to a change in the parameters of both high-frequency and static field. This property can be used for creating various microwave devices based on systems of the type described above.

REFERENCES

1. A. G. Gurevich and G. A. Melkov, *Magnetic Oscillations and Waves* (Nauka, Moscow, 1994).
2. B. Neite and H. Doetsch, J. Appl. Phys. **62** (2), 648 (1987).
3. S. M. Rezende and F. M. de Aguiar, Proc. IEEE **78** (6), 893 (1990).
4. A. G. Temiryazev, M. P. Tikhomirova, and A. V. Maryakhin, in *Proceedings of the International Workshop "New Magnetic Materials for Microelectronics", Moscow, 1998,* Part 1, p. 270.
5. A. M. Shutyĭ and D. I. Sementsov, Zh. Éksp. Teor. Fiz. **118** (3), 110 (2000) [JETP **91**, 531 (2000)].
6. K. Gnatzig, H. Doetsch, M. Ye, *et al.*, J. Appl. Phys. **62** (12), 4839 (1987).
7. A. D. Bordman, S. A. Nikotov, and Q. Wang, IEEE Trans. Magn. **MAG30** (1), 1 (1994).
8. A. Prabhakar and D. D. Stancil, J. Appl. Phys. **85** (8), 4859 (1999).
9. Yu. K. Fetisov and C. E. Patton, Radiotekh. Élektron. (Moscow) **45** (6), 735 (2000).
10. N. G. Bebenin and V. V. Ustinov, Fiz. Met. Metalloved. **84** (2), 29 (1997).
11. A. B. Drovosekov, N. M. Kreĭnes, D. I. Kholin, *et al.*, in *Proceedings of the 16th International Workshop "New Magnetic Materials for Microelectronics," Moscow, 1998*, Part 1, p. 14.

Translated by P. Pozdeev

Excitation of the Opposite Acoustic Flows in Thermodynamically Nonequilibrium Gaseous Media

N. E. Molevich

Samara State Aerospace University, Samara, Russia
e-mail: molevich@mb.ssau.ru

Abstract—It is shown that the acoustic wind direction may change in an acoustically active gaseous medium. © 2001 MAIK "Nauka/Interperiodica".

As is known, high-power acoustic beams spreading in a liquid or gaseous medium give rise to an aperiodic motion of the medium called the acoustic wind. In the general case, this flow is caused both by the viscous losses of the acoustic wave momentum and by inertial (nonlinear) losses [1–3]. Below, we will consider the acoustic wind in a gas caused by the first mechanism. This kind of flow is described by the equation

$$\frac{\partial \mathbf{U}}{\partial t} + (\mathbf{U}\nabla)\mathbf{U} - \frac{\eta}{\rho}\Delta\mathbf{U} = -\frac{\nabla P}{\rho} + \mathbf{F}, \qquad (1)$$

where P is the pressure, ρ is the density of the medium, η is the shear viscosity coefficient, and $\mathbf{F}$ is the radiation force (per unit mass) inducing the flow in the gas with a velocity $\mathbf{U}$. If an acoustic flow is caused by the absorption of a plane wave with the amplitude V_0 running along the x axis, the radiation force can be expressed as [2]

$$F \approx \alpha V_0^2 \exp(-2\alpha x), \qquad (2)$$

where

$$\alpha = \frac{\omega^2}{2u_s^3(\omega)\rho_0}\left[\mathrm{Re}\xi(\omega) + \frac{4}{3}\eta + \chi\left(\frac{1}{C_V} - \frac{1}{C_P}\right)\right]$$

is the acoustic decrement; ω is the wave frequency; u_s is the velocity of sound; ξ is the second viscosity coefficient (in the general case of arbitrary frequencies, this is a complex quantity [4], $\mathrm{Re}\xi$ being the real part of ξ); χ is the thermal conductivity coefficient; and C_V and C_P are the heat capacities at constant volume and pressure, respectively.

In a thermodynamically nonequilibrium medium, the second viscosity coefficient (specifically, $\mathrm{Re}\xi$) may become negative [5]. Examples of the media where this phenomenon can take place are offered by gases with nonequilibrium excited internal states of molecules, nonisothermal plasmas, chemically active gas mixtures, and some other media with volume heat evolution sources. A medium obeying the condition $\mathrm{Re}\xi + 4\eta/3 +$

$\chi\left(\frac{1}{C_V} - \frac{1}{C_P}\right) < 0$ is acoustically active ($\alpha < 0$). In such a medium, according to Eqs. (1) and (2), the radiation force and the acoustic wind directions must change to opposite: a nonequilibrium medium with $\alpha < 0$ gives energy to the propagating acoustic wave and moves in the opposite direction.

We will study this opposite motion in the case of an Eckert flow. The velocity U_0 of a stationary Eckert flow in an acoustically active gas at the axis of a cylindrical tube of large diameter (compared to the sound wavelength) can be evaluated by analogy with the case of a passive medium [1, 6]. According to the Poiseuille formula,

$$U_0 = \frac{\Delta P R^2}{4\eta x}, \qquad (3)$$

where R is the radius of the acoustic beam (assumed to be homogeneous in the cross section, with zero flow velocity at the boundaries) and ΔP is the static pressure difference between two cross sections spaced by the distance x. For $U_0 \ll u_s$, the pressure difference ΔP is simply a drop of the radiation pressure [1, 6], that is, a change in the momentum transferred by the acoustic wave to the medium per unit area and unit time. The radiation pressure can be expressed through a difference of the time-average acoustic energy densities in the cross sections with the coordinates 0 and x [6]:

$$\Delta P = \bar{E}(0) - \bar{E}(x) = \bar{E}(0)[1 - \exp(-2\alpha x)]. \quad (4)$$

Substituting Eq. (4) into (3) and assuming that $|\alpha|x \ll 1$, we obtain

$$U_0 = \frac{I_0 R^2 \alpha}{2u_s\eta}, \qquad (5)$$

where I_0 is the acoustic beam intensity at $x = 0$. In an absorbing medium, relationship (5) coincides with the well-known expression for the velocity of the Eckert flow propagating in the direction of the acoustic wave at the axis of a cylindrical tube with hard walls [1–3, 6].

For an acoustically active medium with $\alpha < 0$, relationship (4) yields $\Delta P < 0$, which implies that the static pressure in the cross section x is greater than that in the initial cross section. Since the radiation force and the flow velocity are proportional to ΔP, the projections of both quantities onto the direction of sound propagation will be negative (in contrast to the case of an absorbing medium).

An analogous phenomenon, previously observed in piezoelectric semiconductors, is known as the acoustoelectric effect [6]. According to this effect, representing the solid-state analog of an acoustic flow in gaseous and liquid media, the acoustic wave propagating in a piezoelectric solid excites an electron current $J_e \sim \mu \alpha I_0/u_s$, where μ is the mobility of electrons. For $\alpha > 0$ (sound absorption), the acoustic wave gives energy to electrons and the current flows in the direction of sound propagation. For $\alpha < 0$ (sound amplification), the energy and momentum are transferred from electrons to the acoustic wave. As a result, the drift current decreases by J_e (this current component is opposite to the acoustic wave).

Experimental observations of the opposite acoustic flows in a thermodynamically nonequilibrium gas might provide additional evidence for the acoustic activity of such media.

REFERENCES

1. L. K. Zarembo and V. A. Krasil'nikov, *Introduction to Nonlinear Physical Acoustics* (Nauka, Moscow, 1966).
2. O. V. Rudenko and S. I. Soluyan, *Theoretical Foundations of Nonlinear Acoustics* (Nauka, Moscow, 1975; Consultants Bureau, New York, 1977).
3. L. K. Zarembo and V. I. Timoshenko, *Nonlinear Acoustics* (Nauka, Moscow, 1984).
4. L. D. Landau and E. M. Lifshitz, *Course of Theoretical Physics*, Vol. 6: *Fluid Mechanics* (Nauka, Moscow, 1986; Pergamon, New York, 1987).
5. N. E. Molevich and A. N. Oraevskiĭ, Tr. Fiz. Inst. Akad. Nauk **222**, 45 (1992).
6. V. A. Krasil'nikov and V. V. Krylov, *Introduction to Physical Acoustics* (Nauka, Moscow, 1984).

Translated by P. Pozdeev

A Functional for the Input Impedance of Thin Electric Vibrator

V. A. Neganov, D. S. Klyuev, and S. V. Medvedev

State Academy of Telecommunications and Informatics, Samara, Russia
e-mail: _neganov_@mail.ru
Received May 10, 2001

Abstract—A functional for the input impedance of electric vibrator is derived for the variation of the distribution of vibrator current. Using the approximation of sinusoidal current distribution, a simple approximate formula for the input impedance of a symmetric electric vibrator is derived. The active and reactive components of impedance are calculated versus the ratio of the length of vibrator arm to wavelength for three values of the vibrator diameter. © *2001 MAIK "Nauka/Interperiodica".*

1. Formulation of the problem. Thin electric vibrators find numerous applications as both individual antennas and elements of complex antenna systems. Usually, the input impedance of an electric vibrator is determined from the voltage-to-current ratio at the feeding point: $Z = U/I_0$. The input impedance is an important parameter determining the possibility of matching the antenna input in a required frequency band. The current I_0 at the feeding point can be determined numerically by solving the Pocklington and Harrington integro-differential equations or the Hallen integral equation [1–4]. However, a numerical solution of these equations as the integral equations of the first kind with Fredholm kernels leads to ill-conditioned problems [5]. Therefore, it may be difficult to determine whether the solution obtained is close to a true one and is adequate to the physical problem under study.

A mathematically correct calculation for the characteristics of an electric vibrator was performed in [6, 7] with the help of singular integral equations [8, 9]. However, this method requires a rather complicated numerical procedure for determining the distribution of vibrator current. There is also a heuristic method of equivalent circuits [2, 3], in which the vibrator is associated with a section of an open-ended two-wire lossy transmission line. However, this method has a limited domain of applicability. Below, we derive a functional for the input impedance of electric vibrator, which allows us to obtain simple analytic formulas for the impedance Z.

2. The input impedance functional. Let us consider a thin wire of length $2l$ and radius a. The wire has a gap at $z \in [l_0 - b, l_0 + b]$ where it is connected to an oscillator (Fig. 1). We will use the Pocklington integro-differential equation for an unknown current I:

$$\left(k^2 + \frac{d^2}{dz^2}\right)\int_{-l}^{l} I(z')\frac{e^{-ikR}}{R}dz' = -\frac{i4\pi k}{Z_c}E^{\text{ext}}, \quad (1)$$

where

$$E^{\text{ext}} = \begin{cases} E_0 & z \in [l_0 - b, l_0 + b], \\ 0 & z \notin [l_0 - b, l_0 + b], \end{cases}$$

is the external electric field, $R = \sqrt{(z - z')^2 + a^2}$, $k = \omega/c$ is the wave number, and Z_c is the characteristic impedance of the medium surrounding the vibrator.

Rewrite the Pocklington equation (1) as follows:

$$k^2\int_{-l}^{l} I(z')\frac{e^{-ikR}}{R}dz' + \frac{d}{dz}\int_{-l}^{l} I'(z')\frac{e^{-ikR}}{R}dz' = -\frac{i4\pi k}{Z_c}E^{\text{ext}}, \quad (2)$$

where $I'(z') = \dfrac{dI}{dz'}$.

Deriving Eq. (2), we used the boundary conditions for the current at the vibrator ends ($I(l) = I(-l) = 0$) and the following evident equality:

$$\frac{d}{dz}\frac{e^{-ikR}}{R} = -\frac{d}{dz'}\frac{e^{-ikR}}{R}.$$

Multiplying relationship (2) by $I(z)$ and integrating from $-l$ to l, we obtain the equality

$$\int_{-l}^{l}\int_{-l}^{l} [k^2 I(z)I(z') - I'(z)I'(z')]\frac{e^{-ikR}}{R}dz'dz$$

$$= -\frac{i4\pi kE_0}{Z_c}\int_{-b}^{b} I(z)dz, \quad (3)$$

which, for narrow gaps ($kb \ll 1$), transforms into a

functional for the vibrator input impedance:

$$Z = \frac{U}{I_0}$$

$$= \frac{iZ_c}{4\pi k} \frac{\int\limits_{-l-l}^{l\,l} [k^2 I(z)I(z') - I'(z)I'(z')] \frac{e^{-ikR}}{R} dz' dz}{I_0^2}, \quad (4)$$

where I_0 is the current at the feeding point, $z = l_0$, and $U = 2E_0 b$.

It can readily be shown that, if the function $I(z)$ obeys condition (2) and, consequently, the Pocklington equation (1), relationship (4) is a stationary functional for the variation of function $I(z)$.

3. Formula for the input impedance. Numerical results. To simplify the subsequent analysis, let us consider a symmetric vibrator fed at $l_0 = 0$. For the trial function, we will use a well-known approximate current distribution over a symmetric vibrator [2, 3]:

$$I(z) = \frac{I_0 \sin k(l - |z|)}{\sin kl}. \quad (5)$$

Substituting formula (5) into functional (4) and using a well-known formula [10]

$$\frac{e^{-ikR}}{R} = \frac{-i}{2} \int\limits_{-\infty}^{\infty} e^{-ih(z-z')} J_0(-ia\sqrt{h^2 - k^2}) H_0^{(2)}$$

$$\times (-ia\sqrt{h^2 - k^2}) dh \quad (6)$$

(where $J_0(x)$ and $H_0^2(x)$ are the zero-order Bessel function of first kind and the zero-order Hankel function of second kind, respectively), we can write the following approximate formula for the input impedance:

$$Z = \frac{-Z_c}{8\pi} \int\limits_{-\infty}^{\infty} K_+(\beta)K_-(\beta)$$

$$\times J_0(-i\sqrt{\beta^2 - (ka)^2}) H_0^{(2)}(-i\sqrt{\beta^2 - (ka)^2}) d\beta, \quad (7)$$

where

$$K_\pm(\beta) = \int\limits_{-kl}^{kl} \{ \sin(kl - |t|)$$

$$+ \operatorname{sgn}(t)\cos(kl - |t|)\} e^{\pm i\frac{l}{a}\beta} dt. \quad (8)$$

Note that integrals (8) can readily be evaluated analytically. (Since the corresponding expressions are rather cumbersome, we do not present them here.) As a result, formula (7) for the input impedance contains only one integral with respect to the parameter β, which should be calculated numerically.
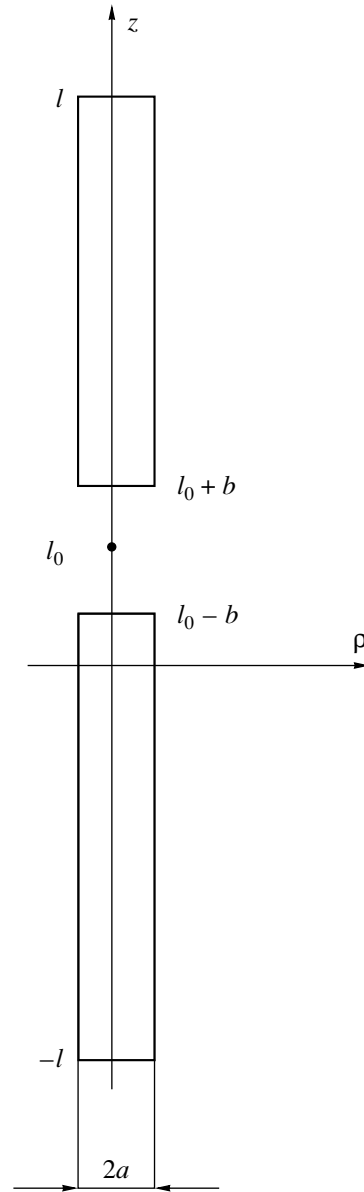

Fig. 1.

Figures 2a and 2b depict the active and reactive components of the input impedance of a symmetric vibrator versus the parameter l/λ for three values of the wire diameter. The solid, dotted, and dashed lines in Fig. 2b are the reactive components calculated for $a/l = 1/100$, $1/60$, and $1/20$, respectively. Note that active components of the input impedance calculated for the same a/l virtually coincide with each other. Therefore, Fig. 2a presents only one plot (for $a/l = 1/100$). When the parameter l/λ varies from 0 to 1, the input impedance passes three resonance regions. The first (series) resonance is located near $l/\lambda = 0.25$, the second (parallel) resonance is located at l/λ slightly below 0.6, and the third resonance is observed at $l/\lambda \approx 0.75$. For $l/\lambda < 0.25$, the reactive part of input impedance is neg-
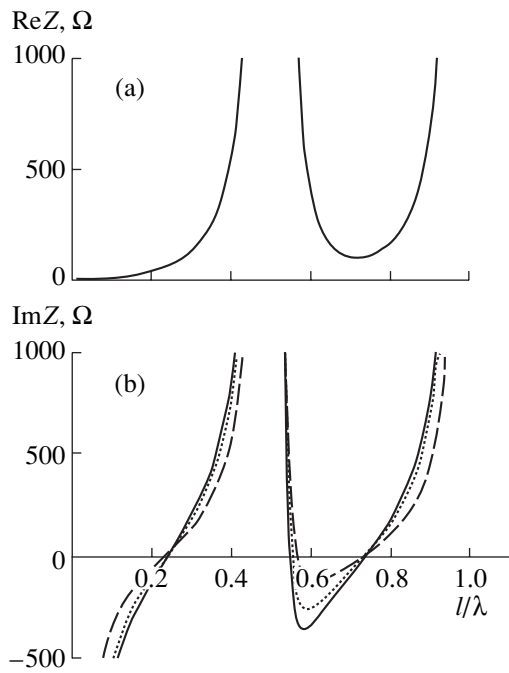
ReZ, Ω

(a)

ImZ, Ω

(b)

Fig. 2.

ative (capacitive). At $0.25 < l/\lambda < 0.55$, it is positive (inductive). At $0.55 < l/\lambda < 0.75$, the reactive part of the input impedance changes to negative (capacitive). At $l/\lambda > 0.75$, it again becomes positive (inductive).

These curves qualitatively agree with those calculated by the method of equivalent circuits in [2], according to which the vibrator was replaced with a section of an open-ended two-wire lossy transmission line.

Thus, stationary functional (4) allows us to derive analytical formulas for the input impedance of a vibrator. Functional (4) can also be used to derive the input

impedance of a nonsymmetric vibrator. To do this, one should only substitute into the functional an appropriate expression for the current distribution. Note that, if characteristics of a nonsymmetric vibrator are analyzed by the method of equivalent circuits, it may be difficult to choose an appropriate substituting equivalent circuit.

REFERENCES

1. *Computer Techniques for Electromagnetics*, Ed. by R. Mittra (Pergamon, Oxford, 1973; Mir, Moscow, 1977).

2. D. M. Sazonov, *Antennas and Microwave Devices: Textbook for Radio Engineering Specialty of Colleges* (Vysshaya Shkola, Moscow, 1988).

3. G. A. Erokhin, O. V. Chernyshev, N. D. Kozyrev, *et al.*, *Antenna–Feeder Devices and Radio Wave Propagation: Textbook for Colleges,* Ed. by G. A. Erokhin (Radio i Svyaz', Moscow, 1996).

4. V. A. Neganov, S. B. Raevskiĭ, and G. P. Yarovoĭ, *Linear Macroscopic Electrodynamics,* Ed. by V. A. Neganov (Radio i Svyaz', Moscow, 2000), Vol. 1.

5. A. N. Tikhonov and V. Ya. Arsenin, *Solutions of Ill-Posed Problems* (Nauka, Moscow, 1986; Halsted Press, New York, 1977).

6. V. A. Neganov and I. V. Matveev, Dokl. Akad. Nauk **373** (1), 36 (2000) [Dokl. Phys. **45**, 317 (2000)].

7. V. A. Neganov and I. V. Matveev, Izv. Vyssh. Uchebn. Zaved., Radiofiz. **43** (3), 335 (2000).

8. V. A. Neganov, E. I. Nefedov, and G. P. Yarovoĭ, *Strip Lines and Slot Lines for Microwave and Extremely High Frequencies* (Nauka, Moscow, 1996).

9. V. A. Neganov, E. I. Nefedov, and G. P. Yarovoĭ, *Modern Methods for Designing Transmission Lines and Resonators of Microwave and Extremely High Frequencies* (Pedagogika-Press, Moscow, 1998).

10. G. P. Markov and A. F. Chaplin, *Electromagnetic Wave Excitation* (Énergiya, Moscow, 1967).

Translated by A. Kondrat'ev

The Conditions for Realization of the Boltzmann Distribution of Negative Ions in a Plasma

E. A. Bogdanov and A. A. Kudryavtsev*
St. Petersburg State University, St. Petersburg, Russia
* e-mail: akud@ak2138.spb.edu
Received May 10, 2001

Abstract—The self-consistent electric field acting in a plasma retards the most mobile charged particles, which usually leads to a Boltzmann distribution of electrons. If negative ions cross the discharge volume several times during their lifetime in the volume processes, these particles also obey the Boltzmann distribution. It is demonstrated that this condition is usually satisfied when the characteristic time of electron attachment is small as compared to the time of ambipolar diffusion of the negative ions (ion diffusion at an electron temperature). In the opposite case, the profiles of electrons and negative ions are similar. © 2001 MAIK "Nauka/Interperiodica".

In the late 1950s, Oskam [1] and Tompson [2] virtually simultaneously suggested simple relationships between the concentrations and concentration gradients of charged particles in a stationary electronegative gas plasma. Oskam postulated that the concentration profiles of electrons and negative ions are similar [1],

$$\nabla n_e / n_e = \nabla n_n / n_n, \quad n_e(x)/n_n(x) = \text{const}, \qquad (1)$$

while Tompson assumed that both n_e and n_n profiles are described by the Boltzmann distribution [2]

$$T_e \nabla n_e / n_e = T \nabla n_n / n_n. \qquad (2)$$

Condition (2) leads to a relationship $n_e(x)/n_e(0) = n_n(x)/n_n(0)^{1/k}$ that sharply depends on the temperature ratio $k = T_e/T$ and coincides with the distribution (1) only in the special case of $T_e = T$. Since a discharge plasma is usually characterized by $k \gg 1$, relationship (2) describes an almost flat profile with $n_e(x) \approx n_{e0} \approx \text{const}$.

The boundaries of applicability of relationships (1) and (2) were not strictly determined and various researchers still deliberately prefer one or another (see, e.g., [3–11]). For example, Lichtenberg *et al.* [5–7] used condition (2) as the basic relationship in constructing the concentration profiles and describing the similarity laws in an electronegative plasma. Recently, Franklin and Snell [11–13] argued in favor of the proportionality condition (1), which was previously employed in [8–10]. The very possibility of using the Boltzmann equilibrium condition for the negative ions in a collisionless plasma was sharply criticized in [11–13] without any possibility for a compromise.

In the context of this renewed discussion (for detail, see [11–13]), which dates back for more than half a century, it was expedient to consider the problem more thoroughly. The following analysis is based on the approach developed previously [14, 15].

The problem formulation, which is virtually the same in [5–15], employs the drift–diffusion equations and the Boltzmann distribution for electrons $E = -T_e \nabla n_e / n_e$. In a plane-parallel geometry ($x = \pm L$), the initial system of equations is as follows ($dn/dx \equiv n'$):

$$-D_p(n_p' + k n_p n_e'/n_e)' = Z_i n_e - K_r n_n n_p, \qquad (3)$$

$$-D_n(n_n' - k n_n n_e'/n_e)' = K_a n_e - K_d n_n - K_r n_n n_p, \qquad (4)$$

$$n_p = n_n + n_e, \qquad (5)$$

where K_a, K_d, and K_r are the electron attachment, detachment, and ion–ion recombination constants, respectively, which are considered as preset; Z_i is the ionization frequency representing an eigenvalue of the boundary problem (3)–(5). Since the latter quantity is unknown a priori, we believe that it is inexpedient to pass in Eqs. (3)–(5) to dimensionless variables in terms of this undetermined Z_i value (see, e.g., [8–13]).

The boundary conditions to Eqs. (3) and (4) are as follows [5–15]:

$$n_n = n_p = dn_n/dx = 0 \quad \text{at} \quad x = \pm L,$$
$$dn_n/dx = dn_p/dx = 0 \quad \text{at} \quad x = 0. \qquad (6)$$

Since the flux of negative ions to the walls is absent, the cross-section-average concentrations ($\bar{n}$) in Eq. (4) obey the relationship [5–15]

$$K_a \bar{n}_e = K_d \bar{n}_n + K_r \bar{n}_n \bar{n}_p. \qquad (7)$$

The system of equations (3)–(5) was used with various simplifications in all papers cited above [5–15]. It was established that a spatial distribution of charged particles in the plasma is characterized by a sharply inhomogeneous profile (Fig. 1). Almost all negative ions are concentrated in the inner region of the ion–ion plasma having the thickness $x = x_0$ (values referred to
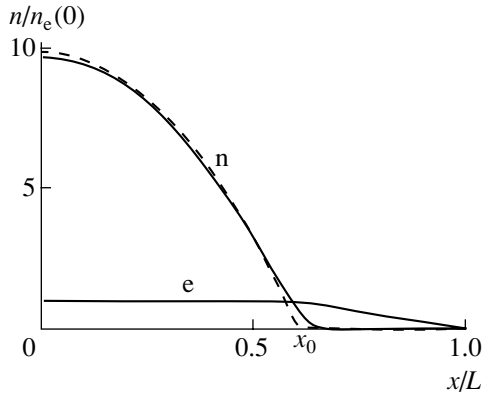
Fig. 1. The spatial distributions of charged particle concentrations calculated for $k = 33$, $\tau_{an}K_a = 0.1$ and $K_a/K_d = 4$. Solid curves represent the exact solution of system (3)–(5), dashed curves show the approximation by formulas (15) and (16).
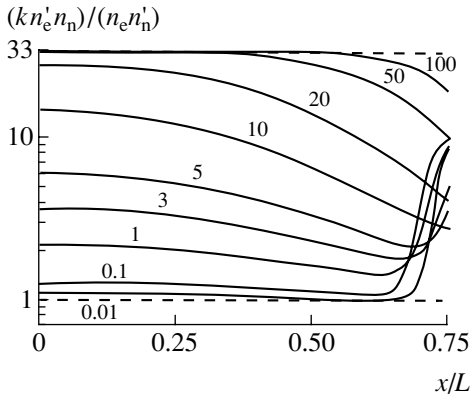

Fig. 2. A relationship between the spatial distributions of electron and negative ion concentrations calculated for $k = 33$, $K_a/K_d = 4$, and various values of the parameter $\tau_{an}K_a$ (indicated by figures at the curves). Dashed lines show the limiting values 1 and 33 corresponding to relationships (1) and (2), respectively.

this region are indicated by subscript "0"). The outer region, featuring the electron–ion plasma (indicated by subscript "1"), contains electrons and positive ions, while negative particles are virtually absent. Relationships of the type of Eqs. (1) and (2) make sense only in the former region "0."

The structure of a solution to system (3)–(5) is most simply determined from an overall equation derived in [14]. Dividing Eqs. (3) and (4) by the corresponding diffusion coefficients and adding the resulting expressions, we obtain for $k \gg 1$

$$-2n_n''/k - n_e'' = n_e/l_e^2 - 2n_n/kl_n^2. \quad (8)$$

This equation involves two characteristic spatial scales l_e and l_n such that

$$1/l_e^2 = 1/l_{ion}^2 + 1/l_a^2$$
$$= Z_i/D_{ap} + K_a/D_{an} = \tau_{ap}Z_i/L^2 + \tau_{an}K_a/L^2, \quad (9)$$

$$1/l_n^2 = 1/l_{nd}^2 + 1/l_{nr}^2$$
$$= K_d/2D_n + n_pK_r/D_{np} = \tau_nK_d/L^2 + \tau_{np}K_rn_p/L^2, \quad (10)$$

where $D_{an, ap} = D_{n, p}(k + 1)$ and $D_{np} = 2D_nD_p/(D_n + D_p)$ are the coefficients of the electron–ion and ion–ion ambipolar diffusion and $\tau_j = L^2/D_j$ are the corresponding characteristic times.

The characteristic length l_e determines the maximum possible thickness of the outer region "1." In this region, the concentration of negative ions is very small ($n_n(x) \approx 0$) and, hence, $n_e(x) \approx n_p(x)$, because these ions are collected in the inner plasma region under the action of the ambipolar field. With neglect of the terms involving n_n, Eq. (8) for $x \geq x_0$ reduces to $-n_e'' = n_e/l_e^2$ to yield [14]

$$n_e(x) = n_e(x_0)\sin((1 - x)/l_e)/\sin((1 - x_0)/l_e). \quad (11)$$

In the inner region, the distribution of particle concentrations significantly depends on the ratio of L and l_n, the latter representing the distance through which a negative ion diffuses during its lifetime in the volume processes (see [14, 15]). Since $\tau_{ap}Z_i \geq 1$ (the equality only reached for negligibly small electron attachment and recombination times), we obtain the following estimate using relationship (7):

$$l_n^2/l_e^2 < (\bar{n}_n/k\bar{n}_e)(1 + 1/(\tau_{an}K_a)). \quad (12)$$

Under strong attachment conditions ($\tau_{an}K_a > 1$) and typical $\bar{n}_n/\bar{n}_e < k \approx 100$, the characteristic lengths obey the condition $l_n < l_e < L$. In this case, we may neglect (as it was done in [8–10]) the terms related to the ion diffusion in Eqs. (3)–(5) and take $x_0 \approx l_e$ [14]. For the central regions of the plasma value ($x < l_e$), Eq. (8) yields the following local balance of the plasmachemical processes involving the production and loss of ions: $n_e/l_e^2 = 2n_n/kl_n^2$. This leads to the condition (see [14])

$$(Z_i/D_p + K_{at}/D_n)n_e$$
$$= K_{dt}n_n/D_n + K_rn_n(n_n + n_e)/(1/D_p + 1/D_n). \quad (13)$$

When negative ions are lost as a result of detachment (detachment regime, $K_d \gg n_pK_r$), a trivial consequence of Eq. (13) is relationship (1). Figure 2 shows the results of solving Eqs. (3)–(5) in this case ($K_r = 0$) for various values of the parameters $\tau_{an}K_a$. As this parameter increases in the range $\tau_{an}K_a > 1$, the concentration ratio in the inner region asymptotically tends to that given by distribution (1) (for $\tau_{an}K_a > 10$). For the recombination regime ($K_d < n_pK_r$), condition (12) leads to the relationship (see [14]) $\nabla n_e/n_e = \nabla n_n/n_n + \nabla n_p/n_p \approx 2\nabla n_n/n_n$. According to this (and in contrast with (1)), ions exhibit a more flat distribution than electrons.

If the characteristic length l_n is such that $l_n > L$, the diffusing ions are capable of crossing the entire dis-

charge volume. To be confined in the inner region, the negative ions must obey (like electrons) the Boltzmann distribution (2). According to Eq. (12), the self-diffusion of negative ions dominates ($l_d > L$) only if the role attachment is small in comparison to the ambipolar diffusion of negative ions ($\tau_{an}K_a < 1$). As the parameter $\tau_{an}K_a$ decreases, relationship (2) is obeyed with increasing precision in the inner plasma region (Fig. 2). Thus, depending on the parameter $\tau_{an}K_a$ (which is a quadratic function of the gas pressure), both relationships (1) and (2) can be realized in the system. The transition from the Boltzmann distribution (2) corresponding to weak attachment ($\tau_{an}K_a < 1$) at low gas pressures to the condition of proportionality (1) at higher pressures ($\tau_{an}K_a > 1$) is clearly manifested in Fig. 2.

As noted above, the validity of relationship (2) for $k \gg 1$ implies a flat electron profile $n_e(x) \approx n_{e0}$. Under these conditions, both terms in the left-hand part of Eq. (3) for $n_p(x)$ are approximately equal and we obtain $-2n_n''/k = Z_i n_{e0}$. This relationship corresponds to a parabolic distribution of the ion concentration (see [14] and in more detail [5–7]):

$$n_n(x) = n_{n0}(1 - x^2/x_0^2), \quad n_{n0} = Z_i x_0^2/4D_p. \quad (14)$$

The unknown quantities x_0 and Z_i in Eqs. (13) and (14) are most simply determined from the integral balance of concentrations given by relationship (7) for n_n and by the corresponding expression for n_p. Integrating Eqs. (3) and (4) with respect to the coordinate and using formulas (11) and (14), we obtain the following relationships for determining x_0 and Z_i:

$$K_a n_{e0}(x_0 + l_e \tan(L - x_0)/l_e)$$
$$= 2K_d n_{n0} x_0/3 + 8K_r x_0 n_{n0}^2/15, \quad (15)$$

$$Z_i n_{e0}(x_0 + l_e \tan(1 - x_0)/l_e) - 8K_r x_0 n_{n0}^2/15$$
$$= D_{ap} n_{e0}/(l_e \sin((1 - x_0)/l_e)). \quad (16)$$

The results of calculations using simple formulas (14)–(16) agree well with the solution of system (3)–(5) (Fig. 1). For rough estimates, we may restrict the analysis to first terms in the expansions of sine and tangent in (15) and (16). Taking into account that, in the case of relationship (2), $Z_i > K_a$, and substituting n_{n0} from (14), we arrive at the simple relationships

$$Z_i = 2D_{ap}/(L^2 - x_0^2), \quad (17)$$

$$3K_a/(2kK_d)$$
$$= x_0^3/(L^2 - x_0^2)(L + x_0) \approx (x_0/L)^3 + (x_0/L)^6 \quad (18)$$

for the detachment regime and

$$15K_a/(4k^2K_r n_{e0})$$
$$= x_0^5/(L^2 - x_0^2)^2(L + x_0) \approx (x_0/L)^5 + (x_0/L)^{10} \quad (19)$$

for the recombination regime.

Since the ratios in the left-hand parts of relationships (18) and (19) are usually small (below unity), while the right-hand parts strongly depend on x_0, the x_0 values proper vary within a rather narrow interval of $0.5 \leq x_0 \leq 0.8$. Note that, with neglect of the ion diffusion, the case of weak attachment ($\tau_{an}K_a \ll 1$) for $l_e \approx L$ corresponds to the formation of a narrow ion–ion plasma column with $x_0 \approx \tau_{an}K_a L \ll L$ (see [9, 10]).

Thus, in the case of weak attachment (when the self-diffusion of negative ions prevails over the bulk processes), the Boltzmann distribution is realized for both electrons and negative ions. In all cases of interest, this situation takes place for a small role of attachment in comparison to the ambipolar diffusion of negative ions. In the opposite case of strong attachment, the concentration balance in the inner plasma region is determined by the volume processes and the concentrations of ions and electrons obey similar distributions.

REFERENCES

1. H. J. Oskam, Philips Res. Rep. **13**, 335 (1958).

2. J. B. Tompson, Proc. Phys. Soc. London **73**, 818 (1959).

3. H. S. W. Massey, *Negative Ions* (Cambridge Univ. Press, Cambridge, 1976; Mir, Moscow, 1979).

4. G. L. Rogoff, J. Phys. D **18**, 1533 (1985).

5. A. J. Lichtenberg, V. Vahedi, M. A. Lieberman, and T. Rognlien, J. Appl. Phys. **75**, 2339 (1994).

6. A. J. Lichtenberg, I. G. Louznetsov, T. D. Lee, *et al.*, Plasma Sources Sci. Technol. **6**, 437 (1997).

7. A. J. Lichtenberg, M. A. Lieberman, I. G. Louznetsov, and T. H. Chung, Plasma Sources Sci. Technol. **9**, 45 (2000).

8. C. M. Ferreira, G. Gousset, and M. Touzeau, J. Phys. D **21** (3), 1403 (1988).

9. P. R. Daniels and R. N. Franklin, J. Phys. D **22**, 780 (1989).

10. P. R. Daniels, R. N. Franklin, and J. Snell, J. Phys. D **23**, 823 (1990); **26**, 1638 (1993).

11. R. N. Franklin and J. Snell, J. Phys. D **32**, 2190 (1999).

12. R. N. Franklin and J. Snell, J. Plasma Phys. **64**, 131 (2000).

13. R. N. Franklin, Plasma Sources Sci. Technol. **10**, 174 (2001).

14. L. D. Tsendin, Zh. Tekh. Fiz. **55** (12), 2318 (1985) [Sov. Phys. Tech. Phys. **30**, 1377 (1985)]; Zh. Tekh. Fiz. **59** (1), 21 (1989) [Sov. Phys. Tech. Phys. **34**, 11 (1989)].

15. A. V. Rozanskiy and L. D. Tsendin, *Collision Transport in Partially Ionized Plasma* (Énergoatomizdat, Moscow, 1988; Gordon and Breach, New York, 2001).

Translated by P. Pozdeev

Coherence Resonance in a Closed Chain of Biased Multivibrators

A. P. Nikitin

Saratov State University, Saratov, Russia
e-mail: nikitin@chaos.ssu.runnet.ru
Received May 16, 2001

Abstract—It is demonstrated that a growth in the coherence of oscillations in a closed chain of biased multivibrators can be explained by the unidirectional cyclic coupling of the devices. There is an optimum value of the effective noise voltage for which the multivibrators are most coherent. © *2001 MAIK "Nauka/Interperiodica".*

The coherence of oscillations in a stochastic system may exhibit an increase followed by decrease with increasing noise level in the system [1]. Drawing considerable attention of researchers, this nontrivial phenomenon was studied both in isolated systems [1–3] and in interacting neuron models [4–6]. In the case of coupled systems, it is most interesting to study the regimes of synchronized oscillations [5–6], since it is assumed that this synchronization and the averaging of statistically independent fluctuations of the individual oscillators lead to an increase in the coherence of oscillations in the entire ensemble [6–7]. Below, we demonstrate that, alternatively, a growth in the coherence of oscillations can be explained by unidirectional cyclic coupling of elements in the system. Moreover, the statistical independence of fluctuations in the elements is not a necessary condition.

Biased multivibrators are widely used devices capable of producing, similarly to neurons, an electric response to external perturbations [8, 9]. It should be noted that the excitation of both neurons [10] and multivibrators takes place only when the perturbation exceeds a certain threshold level. Thus, the biased multivibrators are the electronic analogs of neurons and can be used in modeling the stochastic dynamics of neuron chains [4].

Figure 1 shows a schematic diagram of a chain of unidirectionally coupled multivibrators excited by noise. A nonlinear current–voltage characteristic of each element and the diode connection provides for a predominantly unidirectional coupling of the chain elements. This mode of coupling is typical of neurons [10]. The multivibrators are excited by a wideband noise voltage U_n with a Gaussian distribution. The random excitation of, for example, the first multivibrator leads to discharge of capacitor C_2 (belonging to the circuit of the second multivibrator) through diode D_1. Note that the potential on the capacitor determines the excitation threshold of the element. Therefore, the excitation of one multivibrator increases the excitation threshold of the subsequent element, thus reducing its activity. In

turn, the spontaneous excitation of the third multivibrator suppresses activity of the first element. In this case, the second multivibrator occurs in the relaxation regime, the duration of which is determined by the time necessary to charge capacitor C_1. After relaxation, the biased multivibrator is ready to operate.

When a noise fluctuation exceeding the operation threshold enters the second multivibrator, this device operates, switching the third multivibrator into a suppressed state and the first multivibrator into a relaxation regime. Thus, the excitation wave passes from the first to third multivibrator, then proceeds from the third to second, and returns from the second to first. A time interval during which the wave passes through this chain consists of three components: τ_a, the time required for transition into the excited state; τ_b, the time of stay in the excited state; and τ_c, the relaxation time.
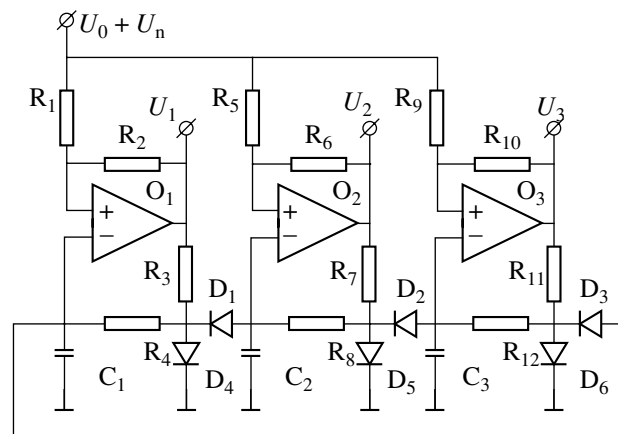

Fig. 1. A schematic diagram of a chain of biased multivibrators comprising integrated circuits O_1–O_3 (K140UD7), diodes D_1–D_6 (D223A), capacitors C_1–C_3 (0.033 μF), and resistors R_1, R_5, R_9 (16 kΩ), R_2, R_6, R_{10} (75 kΩ), R_3, R_7, R_{11} (1.1 kΩ), and R_4, R_8, R_{12} (30 kΩ). U_0 is the bias voltage necessary to drive the multivibrators into a noise-excited regime; U_1–U_3 are the output voltages.
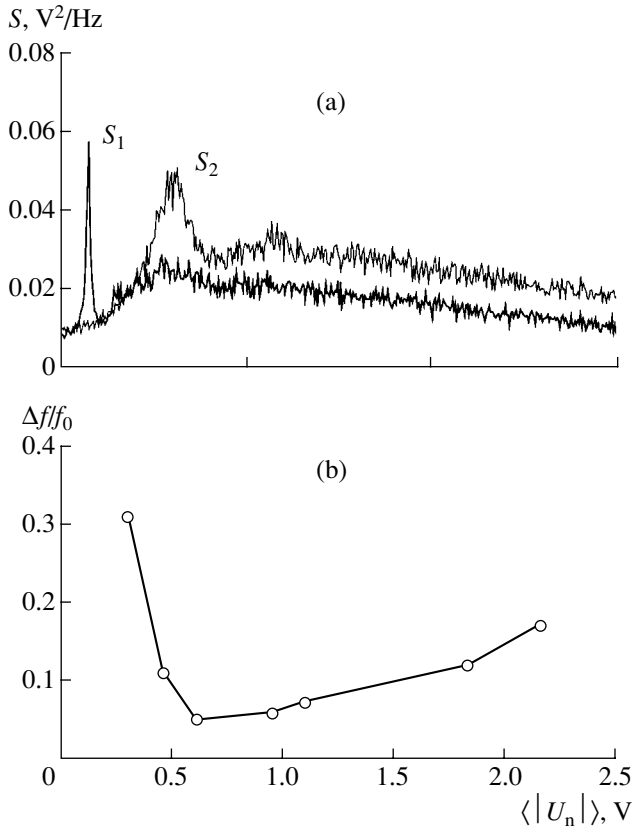
Fig. 2. Output characteristics of biased multivibrators: (a) power density spectra of (S_1) a coupled multivibrator and (S_2) the same autonomous device $(U_0 = 0.21$ V, $\langle U_n \rangle = 0.3$ V); (b) relative width $\Delta f/f_0$ of the spectral band versus effective average noise voltage $\langle U_n \rangle$ $(U_0 = 0.21$ V, U_n is a Gaussian noise with an effective bandwidth of 50 kHz).

The τ_a value of a biased multivibrator is determined by the excitation threshold Δ_U and the noise intensity G; for small G values, this dependence is described by an Arrhenius relationship $\langle \tau_a \rangle \sim \exp(\Delta_U/G)$, where the angle brackets indicate averaging. The time of stay in the excited state τ_b (i.e., the multivibrator pulse duration) weakly depends on the noise level G; for small G values, τ_b can be considered as determined only by the capacitor recharge time proportional to RC. For an autonomous biased multivibrator, the oscillation period T is given by the sum of τ_a and τ_b. As long as the noise intensity is small, the relative uncertainty of the T value is

$$R_0 = \sqrt{\langle T^2 \rangle - \langle T \rangle^2}/\langle T \rangle = \sqrt{\langle \tau_a^2 \rangle - \langle \tau_a \rangle^2}/(\langle \tau_a \rangle + \tau_b),$$

where τ_b is assumed to be constant.

For multivibrator entering into a closed chain, the oscillation period increases to include the relaxation time τ_c. Similar to the τ_b value, the relaxation time (related to a capacitor recharge) is almost strictly determined for small G values. Thus, the mean relative uncertainty of the oscillation period T_c is

$$R_1 = \sqrt{\langle T_c^2 \rangle - \langle T_c \rangle^2}/\langle T_c \rangle$$

$$= \sqrt{\langle \tau_a^2 \rangle - \langle \tau_a \rangle^2}/(\langle \tau_a \rangle + \tau_b + \tau_c),$$

which is smaller for a multivibrator in a chain than for the same multivibrator not coupled to the adjacent elements.

This conclusion is confirmed by the experimental data presented in Fig. 2a. As can be seen from the output power spectra, the width of the main spectral band is smaller for a multivibrator coupled to the analogous devices than for the same device alone. Figure 2b shows a plot of the relative width f/f_0 of the spectral band versus effective average noise voltage $\langle U_n \rangle$. It is seen that the curve is nonmonotonic: there is an optimum value of the effective noise intensity at which the band width is minimum, that is, when the oscillations are most coherent.

This phenomenon can be explained as follows. As long as the noise intensity is small, an increase in G leads to a decrease in the stochastic period component (τ_a) in the total oscillation period. As a result, the coherence of oscillations in the system grows. However, at very large G values, the coherence drops because of the increasing stochastic character of the components τ_b and τ_c that can no longer be considered as strictly determined. It should be noted that all multivibrators in the experiment were identical and excited from a common noise generator.

REFERENCES

1. A. S. Pikovsky and J. Kurths, Phys. Rev. Lett. **78**, 775 (1997).
2. B. Lindner and L. Schimansky-Geier, Phys. Rev. E **61**, 6103 (2000).
3. B. Lindner and L. Schimansky-Geier, Phys. Rev. E **60**, 7270 (1999).
4. D. E. Postnov, S. K. Han, T. G. Yim, and O. V. Sosnovtseva, Phys. Rev. E **59**, R3791 (1999).
5. S. K. Han, T. G. Yim, D. E. Postnov, and O. V. Sosnovtseva, Phys. Rev. Lett. **83**, 1771 (1999).
6. A. Neiman, L. Schimansky-Geier, A. Cornell-Bell, and F. Moss, Phys. Rev. Lett. **83**, 4896 (1999).
7. H. Hempel, L. Schimansky-Geier, and J. Garcia-Ojalvo, Phys. Rev. Lett. **82**, 3713 (1999).
8. N. T. Petrovich and A. V. Kozyrev, *Generation and Conversion of Electrical Pulses* (Sov. Radio, Moscow, 1954).
9. B. I. Goroshkov, *Radioelectronic Devices: Handbook* (Radio i Svyaz', Moscow, 1984).
10. M. R. Rosenzweig, A. L. Leiman, and S. M. Breedlove, *Biological Psychology* (Sinauer Associates, Sunderland, 1996).

Translated by P. Pozdeev

The Formation of Periodic Layered Structures of Components in Heterogeneous Materials under the Action of High-Power Laser Beams

V. S. Golubev and F. Kh. Mirzoev*

Institute for Problems of Laser and Information Technologies, Russian Academy of Sciences, Shatura, Russia
* e-mail: mirzo@lazer.nictl.msk.su

Abstract—A hydrodynamic model is developed to describe the formation of periodic layered structures in heterogeneous condensed systems composed of immiscible components under the action of high-power laser beams in the regime of channeled penetration. The model takes into account the motion of particles of the immiscible components in vortex flows formed in the melt under the action of centrifugal forces. The conditions favoring the development of a periodic concentration variations are established, and the corresponding spatial scale is determined. © 2001 MAIK "Nauka/Interperiodica".

Under certain conditions, the action of a high-power laser radiation on heterogeneous materials (in particular, composites) leads to the separation of components already in the liquid phase (melt), this state being fixed in the form of structures featuring periodic concentration variations upon the melt crystallization after termination of the laser action [1]. Representing a kind of structural defect, this separation may significantly affect various physical properties of the laser-treated heterogeneous material.

During the solidification of the melt appearing in a target material as a result of deep penetration of a high-power laser beam forming an immobile vapor–gas channel (e.g., during a laser spot welding), the melt volume features intensive vortex flows. The liquid flow velocities in these vortices may reach up to $(0.5–10) \times 10^2$ cm/s [2–5].

There are several factors that may account for the development of flows in the melt, the main of which are as follows:

(i) A capillary collapse of the vapor–gas channel walls [4] leading to their "corrugation" accompanied by the formation of a periodic structure of the field of nonstationary flows in the melt volume (a characteristic time of this process is $\sim 10^{-4}–10^{-3}$ s; the corresponding spatial scale of the capillary collapse is on the order of a vapor–gas channel radius $r_0 \sim (2–3) \times 10^{-2}$ cm);

(ii) Capillary–evaporation and thermocapillary instabilities of the vapor–gas channel walls [4, 6, 7] resulting, in particular, in a screwlike shape of the channel surface; interaction of the axial vapor flow (ejected from the channel) with the melt surface may give rise to a three-dimensional flow in the melt volume with a nonzero azimuthal velocity component [8].

If microparticles (or microscopic droplets) of an insoluble impurity with dimensions on the order of $10^{-3}–10^{-2}$ cm are present in the material, periodic impurity layers may also be fixed in the solidifying melt formed around the mobile vapor–gas channel. This can take place as a result of the centrifugal "recession" of heavy impurities toward the periphery of vortices in the melt or "gathering" of light impurities toward the vortex centers.

The purposes of this study were (i) to elucidate a mechanism of the liquid phase separation in heterogeneous materials based on immiscible components under the action of deeply penetrating high-power laser beams, (ii) to determine conditions favoring the periodic layer structure formation, and (iii) to estimate the spatial scale of these phenomena.

Let us consider a medium containing immiscible components A and B, representing a matrix (e.g., of the light component A) with dispersed microparticles (e.g., of the heavier component B), exposed to a high-power laser beam. The microparticles may possess the shape of microscopic droplets formed as a result of the cluster formation in the melt, followed by the diffusion coalescence of these clusters, so that the dimensions of such microparticles may range from 10^{-4} to 10^{-2} cm [1]. An example is offered by Pb microparticles in a Fe matrix [1]. Alternatively, the microparticles may represent solid species of the same dimensions composed of a more refractory material than the matrix (e.g., W in Fe).

If a melt containing the microparticles of an insoluble impurity features vortex motions, the microparticles will be entrained (accelerated), first along the current lines (by the kinetic head of the flow of the main component A) and then toward the periphery of the vortex

(by the centrifugal force). A stationary radial (relative to the vortex center) motion of the microparticles relative to the matrix A must be established within a sufficiently short time $t \approx \tau_s = r_p^2 \rho_p / 9\nu\rho_L$ (ρ_L and ρ_p are the densities of liquid A and particles B, respectively; r_p is the microparticle size; and ν is the kinematic viscosity of liquid A). The velocity of this motion is determined by a balance between the centrifugal force and a viscous hydrodynamic drag of the medium $v_p^{(cm)} \approx (\rho_p - \rho_L) r_p^2 v_m^2 / 9\rho_L \nu r_w$, where v_m is the azimuthal velocity of vortex motion in liquid A, r_w is the characteristic vortex size, and v_p is the radial component of a microparticle.

The maximum size of entrained particles is determined by a relationship between the dynamic pressure of the matrix A moving relative to the droplet and the Laplace pressure determined by the surface tension of the impurity droplet occurring in the matrix. Since we believe that microparticles of the component B are not disintegrated under the action of the kinetic head $\pi r_p^2 (\rho_L v_m^2 / 2)$ while moving relative to the liquid component A, the particle size corresponds to the Weber number $We = \rho_L v_m^2 r_p / \sigma < We_{cr} \cong 10$ [9], where σ is the microparticle surface tension. This implies that the microparticle size cannot exceed $r_p = r_{p(cr)} \cong \sigma We_{cr} / \rho_L v_m^2 \cong 2 \times 10^{-1}$ cm (for $\sigma \cong 4 \times 10^2$ dyn/cm (Pb), $\rho_L = 8$ g/cm^3 (Fe), $\rho_p = 11$ g/cm^3 (Pb), $\nu = 3 \times 10^{-3}$ cm^2/s, and $v_m = 50$ cm/s).

In the regions of contact between two adjacent vortices, the concentration of microparticles must increase, which would result (after solidification of the melt) in the appearance of layers enriched with the impurity component B.

If the density of the impurity B microparticles is smaller than that of the liquid component A (i.e., $\rho_p < \rho_L$), the lighter microparticles will float toward the vortex center (in contrast to the heavier particles with $\rho_p > \rho_L$, which would "sink" toward the vortex periphery).

The vortex motions in the melt are characteristic of the capillary corrugation collapse in the channel (see the figure). For this collapse, the corrugation wavelength is $\Lambda = 2\pi/k_m$, where $k_m \cong (r_0 \sqrt{3})^{-1}$ is the maximum wavenumber of the perturbation. The time of the collapse development (i.e., the time during which the corrugation amplitude increases to reach $\sim r_0$) is $\tau_c \cong (r_0 \sqrt{3})^{3/2} (\rho_L / \sigma_L)^{1/2}$ [4], where σ_L is the surface tension of the major melt component. The velocity of the melt flowing toward the corrugation vertices in the course of
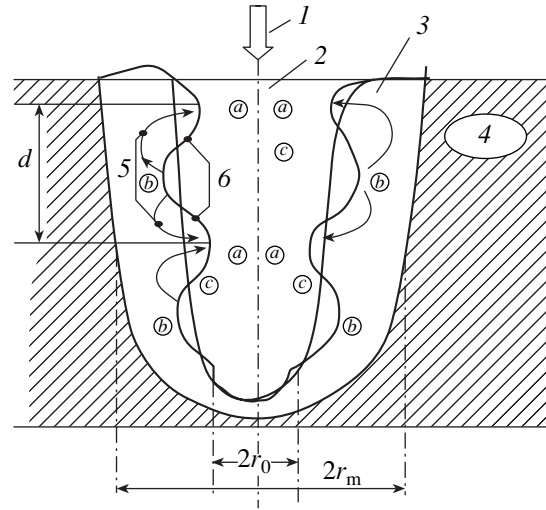
A schematic diagram illustrating the geometry of a vapor–gas channel formed by a high-power laser pulse: (*1*) laser beam; (*2*) vapor–gas channel; (*3*) melt; (*4*) solid phase; (*5*) melt flows; (*6*) corrugation.

collapse (as illustrated in the figure, this motion exhibits a vortex character) can be estimated as

$$v_m \cong r_0/\tau_c \approx 0.5 \left(\frac{\sigma_L}{\rho_L r_0} \right)^{1/2}. \qquad (1)$$

For $\sigma_L = 1.6 \times 10^3$ dyn/cm and $r_0 = 2 \times 10^{-2}$ cm, we obtain $v_m \sim 50$ cm/s.

The time of melt solidification is

$$\tau_f \cong \left(\frac{\bar{T} - T_m}{T_m} \right) \frac{r_m^2}{\chi}, \qquad (2)$$

where $\bar{T}$ is the average temperature of the melt prior to the onset of cooling (laser beam switch off) and r_m is the average radius of the melted zone. According to [10], the latter value can be estimated as $r_m \cong r_0(h/r_0)^{1 - T_m/T_b}$, where T_b and T_m are the boiling and melting points of the major melt component and h is the vapor–gas channel depth. For an Fe target ($T_m \cong 1.8 \times 10^3$ K, $T_b \cong 3 \times 10^3$ K) with $h \cong 0.5$ cm, this yields $r_m \cong 4r_0 \cong 0.8 \times 10^{-1}$ cm.

The melt temperature varies in the radial direction across the vapor–gas channel as

$$T(r) = T_b \frac{\ln(h/r)}{\ln(h/r_0)}. \qquad (3)$$

Averaging over a cylindrical layer gives for the initial melt temperature

$$\bar{T} \cong T_b \left[1 - \frac{\ln(r_m/r_0) - 1/2}{\ln(h/r_0)} \right] \cong 0.7 T_b. \qquad (4)$$

Thus, the melt solidification time can be expressed as

$$\tau_f \cong \frac{8}{3}\frac{r_0^2}{\chi}. \qquad (5)$$

The condition for a periodic layer structure formation in the solidified insoluble impurity can be expressed as

$$v_p\tau_f \geq r \cong r_0, \qquad (6)$$

where r is the radius of a vortex flow in the melt in the course of the capillary corrugation collapse. Substituting formulas (1) and (5) into (6), we reduce this condition to

$$(\rho_p/\rho_L - 1)(\sigma/\rho_L r_0)(r_p^2/\nu\chi) \geq 14.$$

For the parameters $\chi = 10^{-1}$ cm^2/s and $\nu \cong 10^{-3}$ cm^2/s, this implies that the particle size must exceed $r_\rho = 7 \times 10^{-4}$ cm.

Therefore, for solidification of an "immobile" cylindrical melted layer in a collapsing corrugated vapor–gas channel, we may expect that periodic insoluble impurity layers would form along the channel. These layers have the form of curved disks perpendicular to the channel axis. If the impurity is heavy, the periodic layers will be localized at the corrugation antinodes (zones a and b in the figure); for a light impurity, the layers tend to localize at the corrugation nodes (zones c). The spatial scale of the resulting periodic structure coincides with the corrugation period: $d = \Lambda$.

Thus, we formulated and analyzed a qualitative model describing the formation of layered component structures in a solidified melt zone formed in a heterogeneous target under the action of a high-power laser pulse producing a deep fusion of the material. The model explains the layer structure formation by the phenomenon of centrifugal "recession" or "gathering" of impurity microparticles (heavier or lighter than compared to the main component, respectively) with dimensions $\sim 10^{-4}$–10^{-3} cm. The centrifugal effects are manifested in the vortex flows with velocities $\sim(0.5$–$1) \times$ 10^2 cm/s generated in the melt due to hydrodynamic instabilities of a certain nature. In the case of an immobile cylindrically symmetric melted layer surrounding the laser-induced vapor–gas channel, the vortex flows appear as a result of the capillary corrugation collapse in the vapor–gas channel. After the laser pulse switch off, the melt solidifies and the structure of periodic layers is formed along the channel. These layers have the form of curved disks perpendicular to the channel axis. The spatial scale of the resulting periodic structure is $d = 2 \times 10^{-1}$ cm, in agreement with the experimental data reported in [1].

REFERENCES

1. I. N. Shiganov, Vestn. Mosk. Gos. Tekh. Univ., No. 3, 125 (1998); Proc. SPIE **3688**, 211 (1999).

2. A. Mastsunawa, N. Seto, J. Kim, *et al.*, Proc. SPIE **3888**, 34 (2000).

3. V. S. Golubev, Proc. SPIE **3888**, 244 (2000).

4. V. S. Golubev, Preprint No. 83, IPLIT RAN (1999).

5. G. Caillibotte, D. Kechemair, and L. Sabatier, Proc. SPIE **1502**, 50 (1991).

6. F. Kh. Mirzoev, V. S. Panchenko, and L. A. Shelepin, Usp. Fiz. Nauk **166** (1), 3 (1996) [Phys. Usp. **39**, 1 (1996)].

7. F. Kh. Mirsoev and L. A. Shelepin, J. Russ. Laser Res. **19** (6), 528 (1998).

8. S. V. Kayukov, A. A. Gusev, E. G. Zaĭchikov, *et al.*, Izv. Akad. Nauk, Ser. Fiz. **61** (7), 25 (1997).

9. V. M. Voloshchuk and Yu. S. Sedunov, *Coagulation Processes in Disperse Systems* (Moscow, 1975).

10. A. A. Vedenev and G. G. Gladush, *Physical Processes during Laser Material Processing* (Énergoatomizdat, Moscow, 1985).

Translated by P. Pozdeev

A Global Finite-Dimensional Attractor and Coherent Vortex Structures in One Particular Problem of Magnetohydrodynamics

N. B. Volkov

Institute of Electrophysics, Ural Division, Russian Academy of Sciences, Yekaterinburg, Russia

e-mail: nbv@ami.uran.ru; nbv@iep.uran.ru

Abstract—The exact solution of a stationary problem of magnetohydrodynamics is obtained for an incompressible cylindrical conductor possessing constant electric conductivity and shear viscosity. It is shown that a global finite-dimensional attractor in this problem represents a stable focus and has a dimensionality of two. The coherent spatial structures appear as two periodic systems of interacting hydrodynamic and current vortices. © 2001 MAIK "Nauka/Interperiodica".

The determination and investigation of the stationary solutions of infinite-dimensional nonlinear dynamic (e.g., hydrodynamic and magnetohydrodynamic) systems, including proof that such solutions represent global finite-dimensional attractors, is a task of considerable theoretical and practical significance [1–4]. Previously [5], we used an approximate substitution in combination with the Galerkin method [6] to obtain a nonstationary three-mode model. It was shown (numerically and analytically) that this model, employed as a nonlinear element connected parallel to a load resistor in an electric circuit with a dc source, possesses a stationary state. This state corresponds to a global finite- dimensional attractor (with a dimensionality of three) of the initial infinite-dimensional nonlinear dynamic system.

The purpose of this study was to determine an exact substitution that would allow us prove that the obtained stationary solution is a global finite-dimensional attractor for a system of magnetohydrodynamic (MHD) equations (representing an infinite-dimensional dynamic system). In addition, we studied the coherent spatial (hydrodynamic and current) structures formed in this system.

A stationary solution to the MHD problem will be obtained in the case of a cylindrical liquid metal conductor with a radius of r_0 and a length of $l \gg r_0$ possessing a constant density ρ, electric conductivity σ, and shear viscosity η. The stationary MHD equations for this system are as follows:

$$\nabla \cdot \mathbf{v} = 0; \tag{1}$$

$$-\nabla\left(\frac{P}{\rho} + \frac{v^2}{2}\right) + \mathbf{v} \times (\nabla \times \mathbf{v}) \tag{2}$$
$$+ \frac{1}{4\pi\rho}((\nabla \times \mathbf{B}) \times \mathbf{B}) + \nu\Delta\mathbf{v} = 0;$$

$$\nabla \times (\mathbf{v} \times \mathbf{B}) + \nu_m\Delta\mathbf{B} = 0; \tag{3}$$

$$\nabla \cdot \mathbf{B} = 0. \tag{4}$$

Here, $\mathbf{v}$ is the velocity, $\mathbf{B}$ is the magnetic induction, P is the pressure, $\nu = \eta/\rho$ is the kinematic viscosity, $\nu_m = c^2(4\pi\sigma)^{-1}$ is the magnetic viscosity, and c is the speed of light. Equation (1) shows that $\mathbf{v} = \nabla \times \mathbf{A}$, where $\mathbf{A}$ is the vector potential satisfying the Coulomb calibration condition $\nabla \cdot \mathbf{A} = 0$.

Assuming (with an allowance for the problem symmetry) that $\mathbf{A} = \{0, A(r, z), 0\}$, $\mathbf{B} = \{0, B(r, z), 0\}$, and

$$B(r, z) = B_1(r) + h(r, z) = B_0\frac{i}{I_0}\frac{r}{r_0} + h(r, z),$$
$$B_0 = \frac{2I_0}{cr_0}, \tag{5}$$

we can transform Eqs. (1)–(4) to

$$\frac{\partial\{\hat{D}A, A\}_s}{\partial\{r, z\}} - 2\frac{\hat{D}A}{r}\frac{\partial A}{\partial z} + \mathscr{R}\frac{\nu_m\nu}{B_0 r_0^3}\frac{i}{I_0}\frac{\partial h}{\partial z} + \nu\hat{D}^2A = 0, \tag{6}$$

$$\frac{\partial\{h, A\}_s}{\partial\{r, z\}} - 2\frac{h}{r}\frac{\partial A}{\partial z} + \nu_m\hat{D}h = 0. \tag{7}$$

In these expressions,

$$\hat{D} = \Delta - \frac{1}{r^2} = \frac{\partial}{\partial r}\left(\frac{\partial r}{r\partial r}\right) + \frac{\partial^2}{\partial z^2},$$

$$\frac{\partial\{a, b\}_s}{\partial\{r, z\}} = \frac{\partial ra}{r\partial r}\frac{\partial b}{\partial z} - \frac{\partial a}{\partial z}\frac{\partial rb}{r\partial r}$$

is the Poisson bracket, i is the electric current in the conductor, I_0 is a characteristic value of the current, and $\mathfrak{R} = B_0^2 r_0^2 (2\pi\rho\nu_m\nu)^{-1}$ is the Rayleigh magnetic number [5, 7].

The boundary conditions for Eqs. (6) and (7) are as follows:

$$A(0, z) = \hat{D}A(0, z) = A(r_0, z) = \hat{D}A(r_0, z) = 0,$$

$$A\left(r, -\frac{l}{2}\right) = \hat{D}A\left(r, -\frac{l}{2}\right) = A\left(r, \frac{l}{2}\right) = \hat{D}A\left(r, \frac{l}{2}\right) = 0, \quad (8)$$

$$h(0, z) = h(r_0, z) = 0, \quad h\left(r, -\frac{l}{2}\right) = h\left(r, \frac{l}{2}\right). \quad (9)$$

To close the system of equations (6)–(7), we must select a method for determining the electric current i. Let us assume that the liquid metal conductor is connected parallel to a load resistor R_L at a constant voltage of e (the initial resistance of the conductor $R_{p0} = l(\pi r_0^2 \sigma)^{-1}$ obeys the condition $R_L \gg R_{p0}$). In this case,

$$e = \frac{c}{4\pi\sigma}\int_{-\frac{1}{2}}^{\frac{1}{2}}\left(\frac{\partial rB}{r\partial r}\right)_{r = r_0} dz$$

$$= \frac{cB_0 l}{2\pi\sigma r_0}\left(\frac{i}{I_0} + \frac{1}{2l}\int_{-\frac{1}{2}}^{\frac{1}{2}}\left(\frac{\partial rh}{r\partial r}\right)_{r = r_0} dz\right).$$

Determining the characteristic current I_0 from the condition $e = R_{p0}I_0$, we obtain

$$\frac{i}{I_0} = 1 - \frac{1}{2lB_0}\int_{-\frac{1}{2}}^{\frac{1}{2}}\left(\frac{\partial rh}{r\partial r}\right)_{r = r_0} dz. \quad (10)$$

Taking this relationship into account, Eq. (6) can be written as

$$\frac{\partial\{\hat{D}A, A\}_s}{\partial\{r, z\}} - 2\frac{\hat{D}A}{r}\frac{\partial A}{\partial z} + \mathfrak{R}\frac{\nu_m\nu}{B_0 r_0^3}$$

$$\times\left(1 - \frac{1}{2lB_0}\int_{-\frac{1}{2}}^{\frac{1}{2}}\left(\frac{\partial rh}{r\partial r}\right)_{r = r_0} dz\right)\frac{\partial h}{\partial z} + \nu\hat{D}^2 A = 0. \quad (11)$$

With an allowance for the problem symmetry, we may use the following substitution for $A(r, z)$ satisfying the

boundary conditions (8):

$$A(r, z) = X\nu_m\frac{g_1^2 + (kr_0)^2}{kr_0}J_1\left(g_1\frac{r}{r_0}\right)\sin(kz), \quad (12)$$

where $J_1(x)$ is the Bessel function, $g_1 = 3.83171$ is the first zero of $J_1(x)$, k is the wavenumber, and X is the amplitude.

A substitution for the magnetic induction $h(r, z)$ will be found in the form

$$h(r, z) = B_0\left(Yf_1\left(\frac{r}{r_0}\right)\cos kz + f_2\left(\frac{r}{r_0}\right)\right), \quad (13)$$

where the unknown functions $f_1(x)$ and $f_2(x)$ satisfy the following boundary conditions:

$$f_1(0) = f_1(1) = 0, \quad f_2(0) = f_2(1) = 0. \quad (14)$$

Substituting expressions (12) and (13) into Eq. (11), multiplying the resulting equation by $\sin(kz)$, and integrating with respect to z from $-l/2$ to $l/2$, we obtain

$$-\frac{\mathfrak{R}(kr_0)^2}{(g_1^2 + (kr_0)^2)^3}\left(1 - \frac{1}{2}\left(\frac{\bar{r}df_2(\bar{r})}{\bar{r}d\bar{r}}\right)_{\bar{r} = 1}\right)Yf_1(\bar{r})$$

$$+ XJ_1(g_1\bar{r}) = 0, \quad (15)$$

where $\bar{r} = rr_0^{-1}$. Equation (15) is identically valid at all points on the conductor radius provided that $f_1(\bar{r}) = J_1(g_1\bar{r})$. Also identically valid are the following boundary conditions for $f_1(\bar{r})$: $f_1(0) = f_1(1) = 0$. As a result, Eq. (15) acquires the form

$$\left\{-p(k)\left(1 - \frac{1}{2}\left(\frac{d\bar{r}f_2(\bar{r})}{\bar{r}d\bar{r}}\right)_{\bar{r} = 1}\right)Y + X\right\}J_1(g_1\bar{r}) = 0, \quad (16)$$

where $p(k) = \mathfrak{R}\mathfrak{R}_c(k)^{-1}$ is the control parameter,

$$\mathfrak{R}_c(k) = \frac{(g_1^2 + (kr_0)^2)^3}{(kr_0)^2}$$

is the Rayleigh critical number reaching a minimum at $k_0 r_0 = g_1/\sqrt{2}$ (for the wavenumber $k_0 = 2\pi/k_0 = 2\sqrt{2}\pi r_0/g_1 = 2.32r_0$ [5, 8]), where $\mathfrak{R}_c(k_0 r_0) = 27 g_1^4/4$ (hereinafter we assume that $k = k_0$). Relationship (16) gives a condition for the derivative of the function $f_2(\bar{r}) \equiv f(\bar{r})$ at $\bar{r} = 1$:

$$\left(\frac{d\bar{r}f(\bar{r})}{\bar{r}d\bar{r}}\right)_{\bar{r} = 1} = 2\left(1 - \frac{X}{p_0 Y}\right), \quad (17)$$

where $p_0 = p(k_0)$.

For the following, it is convenient to write expressions (12) and (13) in the following form (for $k_0 = g_1(\sqrt{2}\,r_0)^{-1}$):

$$A(r, z) = \sqrt{2}\,g_1\nu_m X J_1\left(g_1\frac{r}{r_0}\right)\sin\left(\frac{g_1 z}{\sqrt{2}\,r_0}\right), \qquad (18)$$

$$h(r, z) = B_0\left(YJ_1\left(g_1\frac{r}{r_0}\right)\cos\left(\frac{g_1 z}{\sqrt{2}\,r_0}\right) + f\left(\frac{r}{r_0}\right)\right). \qquad (19)$$

Substituting these formulas into Eq. (7), we arrive at

$$\left(-\frac{d}{d\bar{r}}\left(\frac{d\bar{r}f(\bar{r})}{\bar{r}\,d\bar{r}}J_1(g_1\bar{r})\right)\right.$$

$$+ XYg_1^3 J_1(g_1\bar{r})\left(J_0(g_1\bar{r}) - 2\frac{J_1(g_1\bar{r})}{g_1\bar{r}}\cos^2\left(\frac{g_1 z}{\sqrt{2}\,r_0}\right)\right)\right)(20)$$

$$+ g_1^2 J_1(\bar{r})\left(-\frac{3}{2}Y + XJ_1(g_1\bar{r}) - 2X\frac{f(\bar{r})}{\bar{r}}\right)\cos^2\left(\frac{g_1 z}{\sqrt{2}\,r_0}\right) = 0.$$

Integrating this equation with respect to z, we obtain

$$\frac{d}{d\bar{r}}\left(\frac{d\bar{r}f(\bar{r})}{\bar{r}\,d\bar{r}} + \frac{1}{2}XYg_1^2 J_1^2(g_1\bar{r})\right) = 0,$$

from which it follows that

$$\frac{d\bar{r}f(\bar{r})}{\bar{r}\,d\bar{r}} + \frac{1}{2}XYg_1^2 J_1^2(g_1\bar{r}) = C. \qquad (21)$$

Here, the constant C can be determined by comparing (21) at $\bar{r} = 1$ to condition (17):

$$C = 2\left(1 - \frac{X}{p_0 Y}\right). \qquad (22)$$

Integrating Eq. (21) and taking into account formula (22), we obtain

$$f(\bar{r}) = \left(1 - \frac{X}{p_0 Y} - \frac{1}{2}g_1^2 XY(J_0^2(g_1\bar{r}) + J_1^2(g_1\bar{r}))\right)\bar{r} \qquad (23)$$

$$+ g_1 XYJ_0(g_1\bar{r})J_1(g_1\bar{r}).$$

Using the boundary condition for $f(\bar{r})$ at $\bar{r} = 1$ (see (14)), we obtain the first equation for the amplitudes X and Y:

$$1 - \frac{X}{p_0 Y} - \frac{1}{2}g_1^2 XYJ_0^2(g_1) = 0. \qquad (24)$$

Multiplying Eq. (20) by $\cos(g_1 z/(\sqrt{2}\,r_0))$ and integrating with respect to z, we obtain

$$\left(-\frac{3}{4}Y + \frac{1}{2}X\frac{d\bar{r}f(\bar{r})}{\bar{r}\,d\bar{r}} - X\frac{f(\bar{r})}{\bar{r}}\right)J_1(g_1\bar{r}) = 0,$$

from which is follows that

$$-\frac{3}{4}Y + \frac{1}{2}X\frac{d\bar{r}f(\bar{r})}{\bar{r}\,d\bar{r}} - X\frac{f(\bar{r})}{\bar{r}} = 0. \qquad (25)$$

Integrating this equation, we arrive at the relationship

$$\left(-\frac{3}{2} + X^2 J_0^2(g_1)\right)Y = 0.$$

For the nontrivial solutions of interest, this relationship yields an expression for the amplitude X:

$$X_{1,2} = \pm\sqrt{\frac{3}{2}}\frac{1}{J_0(g_1)}. \qquad (26)$$

Solving Eq. (24), we obtain the expressions for Y:

$$Y_{1,2} = \frac{1}{g_1^2 XJ_0^2(g_1)}\left(1 \pm \sqrt{1 - \frac{2g_1^2 X^2 J_0^2(g_1)}{p_0}}\right). \qquad (27)$$

In the general case, each of the two X values corresponds to two Y values. For $1 \le p_0 < 3g_1^2$, the amplitude Y is complex. In this interval of the control parameter p_0, the system is characterized by establishing of a current vortex structure. In the region of $p_0 \ge 3g_1^2$ ($\bar{p} = p_0(3g_1^2)^{-1} \ge 1$), the following amplitudes Y have a physical sense:

$$Y_{1,2} = \pm\sqrt{\frac{2}{3}}\frac{1}{g_1^2 J_0(g_1)}\left(1 + \sqrt{1 - \frac{1}{\bar{p}}}\right). \qquad (28)$$

An analysis of this expression shows that the amplitude Y sufficiently rapidly falls within the region of an asymptotically weak dependence on the control parameter. This is related to a sharp drop in the electric current—

$\bar{i} = i\Gamma_0^{-1} = 1 - 0.54(1 - \sqrt{1 - \bar{p}^{-1}})$—in the regions of small but finite values of the critical parameter $\varepsilon = \bar{p} - 1$.

Thus, we have obtained an exact stationary solution to the system of Eqs. (1)–(4) with an infinite-dimensional phase space (below $\bar{z} = zr_0^{-1}$):

$$A(\bar{r}, \bar{z}) = \sqrt{2}\,g_1\nu_m XJ_1(g_1\bar{r})\sin\left(\frac{g_1\bar{z}}{\sqrt{2}}\right); \qquad (29)$$

$$B(\bar{r}, \bar{z}) = B_0\left(\left(1 - \frac{g_1^2 XYJ_0^2(g_1)}{2}\right)\bar{r} + YJ_1(g_1\bar{r})\cos\left(\frac{g_1\bar{z}}{\sqrt{2}}\right)\right.$$

$$(30)$$

$$\left. + \frac{g_1^2 XY}{2}(J_0^2(g_1) - J_0^2(g_1\bar{r}) - J_1^2(g_1\bar{r}))\bar{r} + g_1 XYJ_0(g_1\bar{r})J_1(g_1\bar{r})\right).$$

The phase space of the solution (29), (30) has a dimensionality of two. An analysis of the stability of this solution, based on the investigation of a system of two ordinary linear differential equations for the perturbation amplitudes X and Y showed that the stationary solu-
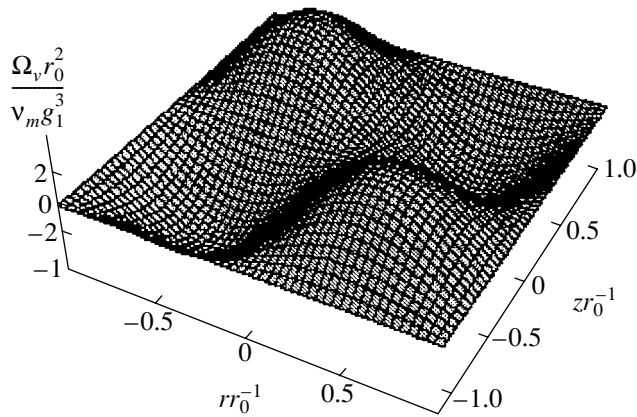
Fig. 1. The spatial structure of hydrodynamic vortices in a unit cell of the vortex lattice in the region $-\sqrt{2}\,\pi g_1^{-1} = -1.16 \le zr_0^{-1} \le \sqrt{2}\,\pi g_1^{-1} = 1.16$.
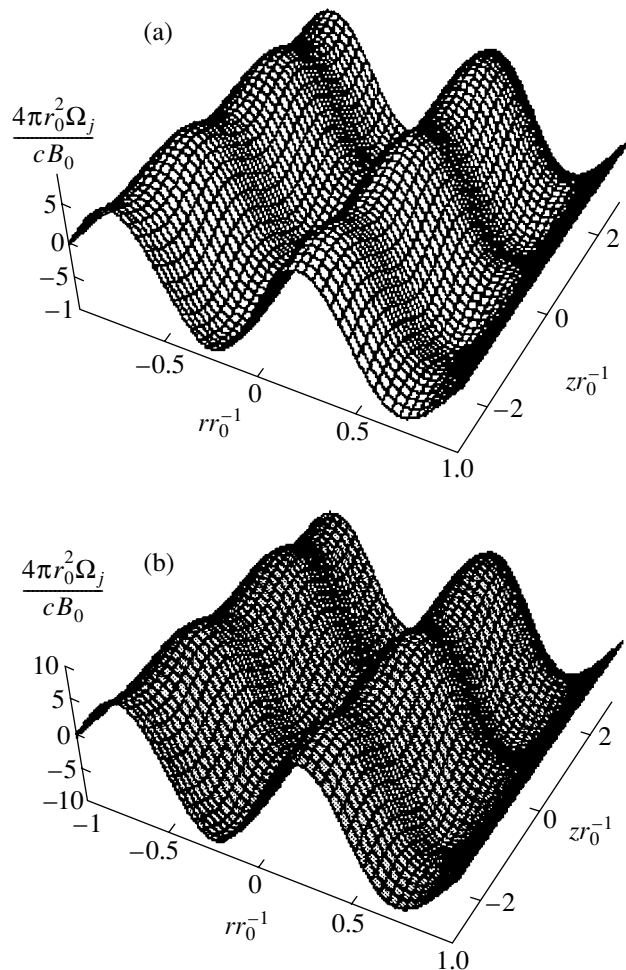

(a)

(b)

Fig. 2. The spatial structure of current vortices in a unit cell of the vortex lattice in the region $-5\pi(\sqrt{2}\,g_1)^{-1} = -3.48 \le zr_0^{-1} \le 5\pi(\sqrt{2}\,g_1)^{-1} = 3.48$ for two values of the control parameter: $\bar{p} = 1$ (a) and 1.05 (b).

tion (29)–(30) corresponds to a global finite-dimensional attractor representing a stable focus.

Using the stationary solution (29)–(30), we may also study the coherent spatial hydrodynamic and current structures. Since we are considering an incompressible conducting liquid, the hydrodynamic spatial structure represents a periodic vortex structure. This hydrodynamic vortex structure is determined by the relationship

$$\Omega_v(\bar{r}, \bar{z}) = -\hat{D}A(\bar{r}, \bar{z})$$
$$= -2\sqrt{3}\,\frac{\nu_m g_1^3}{r_0^2 J_0(g_1)} J_1(g_1 \bar{r}) \sin\!\left(\frac{g_1 \bar{z}}{\sqrt{2}}\right). \tag{31}$$

Figure 1 shows a distribution of the relative vorticity $\bar{\Omega}_v = \Omega_v r_0^2 (\nu_m g_1^3)^{-1}$ in a unit cell of the vortex lattice $(-\sqrt{2}\,\pi g_1^{-1} = -1.16 \le \bar{z} \le \sqrt{2}\,\pi g_1^{-1} = 1.16)$ containing two ring vortices of opposite signs.

The system of hydrodynamic vortices interacts with another vortex structure representing a current vortex lattice with the same period as that of the hydrodynamic vortex. The vorticity vector of the current density is determined by the expression $\Omega_j = c(4\pi)^{-1}\nabla \times \nabla \times \mathbf{B}$. For a given symmetry of the problem, this vector possesses a single azimuthal component:

$$\Omega_j(\bar{r}, \bar{z}) = \frac{cB_0}{4\pi r_0^2 J_0(g_1)}\left(1 + \sqrt{1 - \frac{1}{p}}\right)$$
$$\times \left(-\sqrt{\frac{3}{2}} J_1(g_1 \bar{r}) \cos\!\left(\frac{g_1 \bar{z}}{\sqrt{2}}\right)\right. \tag{32}$$
$$\left. + 2\frac{g_1 J_1(g_1 \bar{r})}{J_0(g_1)}\left(J_0(g_1 \bar{r}) - \frac{J_1(g_1 \bar{r})}{g_1 \bar{r}}\right)\right).$$

Figure 2 show a distribution of the relative vorticity $\Omega_j = 4\pi r_0^2 (cB_0)^{-1}$ of the electric current density vector in the region $-5\pi(\sqrt{2}\,g_1)^{-1} = -3.48 \le \bar{z} \le 5\pi(\sqrt{2}\,g_1)^{-1} = 3.48$ for two values of the control parameter: $\bar{p} = 1$ (Fig. 2a) and 1.05 (Fig. 2b). The further increase in $\bar{p}$ does not change the structure of current vortices because the amplitude $Y(\bar{p})$ rapidly attains the asymptotics.

Thus, we have determined and investigated an exact stationary solution to a system of MHD equations for an incompressible conducting liquid possessing constant electric conductivity and shear viscosity. It is shown that this solution, the phase space of which has a dimensionality of two, corresponds to a global finite-dimensional attractor representing a stable focus. The coherent spatial structures represent two periodic sys-

tems of interacting hydrodynamic and current vortices with the same unit cell size of $\lambda = 2.32r_0$.

REFERENCES

1. R. Temam, *Infinite-Dimensional Dynamical Systems in Mechanics and Physics* (Springer-Verlag, New York, 1988).

2. A. V. Babin and M. I. Vishik, Usp. Mat. Nauk **38** (4), 133 (1983).

3. A. V. Babin and M. I. Vishik, J. Math. Pures Appl. **62** (4), 441 (1983).

4. I. D. Chueshov, Usp. Mat. Nauk **48** (3), 135 (1993).

5. A. M. Iskoldsky, N. B. Volkov, and O. V. Zubareva, Physica D (Amsterdam) **91**, 182 (1996).

6. C. A. J. Fletcher, *Computational Galerkin Methods* (Springer-Verlag, New York, 1984; Mir, Moscow, 1988).

7. N. B. Volkov and A. M. Iskol'dskii, Pis'ma Zh. Éksp. Teor. Fiz. **51**, 560 (1990) [JETP Lett. **51**, 634 (1990)].

8. N. B. Volkov and N. M. Zubarev, Zh. Éksp. Teor. Fiz. **107**, 1868 (1995) [JETP **80**, 1037 (1995)].

Translated by P. Pozdeev

The Structure of Fullerene C_{60} Films Modified by Helium Glow Discharge Plasma

A. V. Vasin[a]*, L. A. Matveeva[a], V. A. Yukhimchuk[a], and E. M. Shpilevskii[b]

[a] *Institute of Semiconductor Physics, National Academy of Sciences of Ukraine, Kiev, Ukraine*
[b] *Belarussian State University, Minsk, Belarus*
** e-mail: vasin@isp.kiev.ua*
Received May 16, 2001

Abstract—The structure of fullerene C_{60} films modified by helium dc glow discharge plasma was studied using Raman scattering spectroscopy. The vibrational spectra of the C_{60} films exhibit certain features depending on the plasma treatment duration. The helium ion bombardment leads to the degradation of the fullerene structure and the formation of an amorphous carbon phase. The coefficient of carbon sputtering by helium was estimated. © 2001 MAIK "Nauka/Interperiodica".

An important direction of research in the physics of fullerenes is related to the modification of fullerene materials by various external factors, including electromagnetic radiation in the visible and UV range [1–3], high pressures [4–6], plasma treatment [7], and electron irradiation [8]. This is explained by interest in the possibility of forming covalent bonds between fullerene molecules. It is suggested that a material with a structure comprising covalently bonded fullerene units must combine the mechanical properties inherent in individual fullerene molecules (extremely high strength of the intramolecular bonds) and fullerites (low friction coefficient). In this context, our purpose was to study the effect of plasma treatment on the structure of fullerene films.

The experiments were performed with approximately 100-nm-thick fullerene films obtained by sublimation of a C_{60} powder from a tantalum effusion cell and deposition onto unheated silicon substrates. The substrates with fullerene films were mounted on a cathode in a plasma treatment setup. The samples were treated in a dc glow discharge plasma at a working gas (helium) pressure of 10 Pa. The discharge voltage was 460 V; the corresponding discharge current density was 150 $\mu A/cm^2$; the plasma treatment duration was varied from 1 to 30 min.

The Raman scattering spectra were measured at room temperature with the aid of a DFS-24 double-beam monochromator. The spectra were excited by an Ar^+ laser operating at a wavelength of 488 nm. In order to avoid excess heating of the fullerene films during the optical measurements, the laser radiation was focused by a cylindrical lens. The probing radiation power did not exceed 100 mW. The Raman spectra were recorded with the aid of a cooled photoelectron multiplier operating in the photon count mode.

A typical Raman spectrum of the initial (untreated) fullerene C_{60} film is represented by curve *1* in the figure. As is seen, the initial spectrum displays three lines peaked at 1426, 1470, and 1578 cm^{-1}, which can be interpreted as the "intramolecular" modes with the symmetry H_g, A_g, and H_g, respectively [9, 10]. Note a significant asymmetry of the line at 1470 cm^{-1}. The low-frequency shoulder in this line is due to the super-
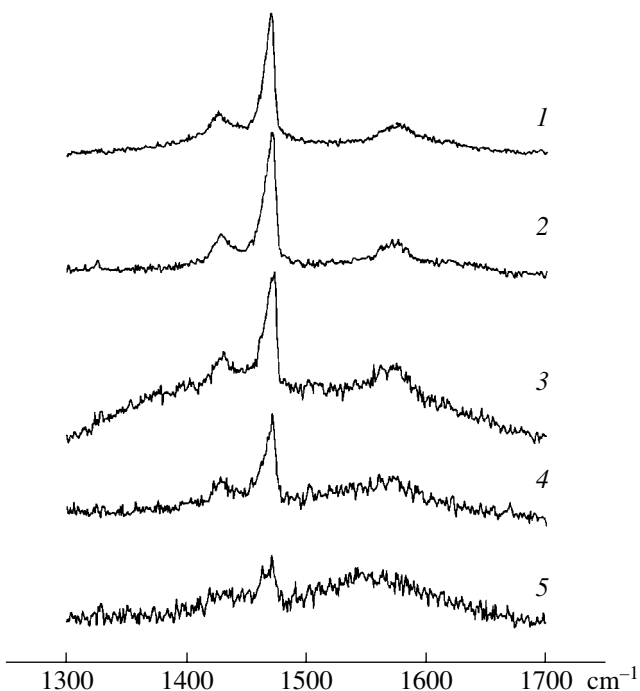
Raman scattering spectra of fullerene C_{60} films (*1*) before and (*2–5*) after treatment in a helium dc glow discharge plasma for various times (min): (*2*) 1; (*3*) 10; (*4*) 16; (*5*) 24.

position of close-lying weaker lines occurring in the region of 1455–1460 cm^{-1}. Unfortunately, there is no commonly accepted opinion about the nature of components of this Raman line. Some researchers assign the line at 1459 cm^{-1} to a polymerized fullerene fraction [1–3], although the physical nature of these vibrations is not clear, since the "intermolecular" vibrational modes must fall into a low-frequency region (about 200 cm^{-1}). However, one may suggest that a decrease in the symmetry of some molecules involved in the intermolecular bond formation may give rise to additional lines in the Raman spectra. According to an alternative assignment, the low-frequency shoulder of the line at 1470 cm^{-1} reflects a contribution to the Raman spectrum from the photoexcited C$_{60}$ molecules [11]. The excited triplet state is antibonding, which must lead to a decrease in the frequency of vibrations corresponding to the fundamental A_g mode.

The plasma treatment of fullerene films for 1 min virtually did not effect the positions and shapes of lines in the Raman spectrum (see curve *2* in the figure). After a 10-min treatment, a broad background band appears in the spectrum in the region from 1300 to 1700 cm^{-1} (curve *3*). Previously [4, 5], a similar broad structureless band was observed in the Raman spectra of superhard carbon samples obtained by treating a C$_{60}$ powder at high pressures and temperatures and in the spectra of graphite irradiated with nitrogen or argon ions to high doses [12] or treated at a hydrostatic pressure above 45 GPa [13]. Besides, a similar band was observed in the Raman spectra of amorphous carbon films deposited onto a substrate under the conditions of intensive bombardment with nitrogen ions [14]. Thus, we may conclude that the broad band at 1300–1700 cm^{-1} appearing after a 10-min plasma treatment is characteristic of a strongly disordered carbon structure. The appearance of this phase in our samples probably reflects the initial stage of fullerene degradation and the formation of an isotropic amorphous carbon structure. An analysis of the shape of the peak at 1470 cm^{-1} showed that the asymmetry of this Raman line did not significantly change after the plasma treatment.

As the plasma treatment duration is increased, the broad background band disappears but a weak band centered at 1560 cm^{-1} appears instead in the high-frequency region (curves *4* and *5*). The halfwidth and position of the new band (~1560 cm^{-1}) are close to the so-called graphitic band (*G*-band) observed for amorphous carbon films. This band is a manifestation of vibrations of the E_{2g} symmetry in graphitelike clusters [15]. Based on these data, we may conclude that the plasma-treated films contain two phases: fullerene and amorphous carbon. Since the ion energies are insufficient to penetrate deep into the film (calculations by the TRIM-2000 program give the average range of singly-charged helium ions in the target under the conditions studied not to exceed 10 nm), we may suggest that decomposition of

the fullerene molecules takes place in a subsurface region of the film featuring the development and decay of the atomic collision cascades.

After a 30-min exposure to the plasma, no Raman scattering signal was detected from the samples. This is explained by the fact that the film was completely removed from substrate as a result of the ion sputtering. A decrease in the film thickness during the plasma treatment was confirmed by a change in the interference color observed after every treatment stage. We have estimated the sputtering coefficient for the fullerene films bombarded by helium ions in the dc glow discharge at a discharge voltage of 460 V. Determined with neglect of the material porosity (the model of close-packed spheres), the sputtering coefficient amounted to about 0.012 mol/ion or 0.72 atom/ion. This estimate markedly exceeds the value (0.15 atom/ion) determined for fullerenes bombarded by neutral argon ions at an energy of 400–500 eV [16]. The ion sputtering is probably accompanied by the sublimation of fullerenes as a result of heating of the substrate holder electrode.

When treated under the conditions studied, the fullerene films are not only subject to the ion bombardment but exposed to the UV radiation of the gas discharge as well. In order to determine which of these factors is responsible for the degradation of fullerenes, we studied the Raman spectra of C$_{60}$ films exposed to the UV radiation from a quartz–mercury lamp of the SVD-120A type with the most intense line corresponding to a wavelength of 365 nm. To increase the intensity of irradiation, the UV radiation was focused on a sample with the aid of a quartz lens. It was found that a 6-h exposure under these conditions did not significantly affect the Raman spectra of C$_{60}$ films. This result gives us ground to assert that the decomposition of fullerene C$_{60}$ molecules during the plasma treatment is mostly related to the ion bombardment.

Thus, we have established that bombardment of a fullerene film with helium ions at an energy of about 400 eV leads, besides the usual sputtering of the film, to the decomposition of C$_{60}$ molecules. This results in the formation of a disordered amorphous carbon structure with a graphitelike short-range order.

REFERENCES

1. Y. Wang, J. M. Holden, Z. H. Dong, *et al.*, Chem. Phys. Lett. **211** (4–5), 341 (1993).

2. P. Zhon, Z. H. Dong, A. M. Rao, *et al.*, Chem. Phys. Lett. **211** (4–5), 337 (1993).

3. A. Ito, T. Morikawa, and T. Takahashi, Chem. Phys. Lett. **211** (4–5), 333 (1993).

4. M. E. Kozlov, M. Hirabayashi, K. Mozaki, *et al.*, Appl. Phys. Lett. **66** (10), 1199 (1995).

5. V. V. Brazhkin, A. G. Lyapin, Yu. V. Antonov, *et al.*, Pis'ma Zh. Éksp. Teor. Fiz. **62** (4), 328 (1995) [JETP Lett. **62**, 350 (1995)].

6. V. V. Brazhkin and A. G. Lyapin, Usp. Fiz. Nauk **166** (8), 893 (1996) [Phys. Usp. **39**, 837 (1996)].

7. N. Takahashi, H. Dock, N. Matsuzava, *et al.*, J. Appl. Phys. **74** (9), 5790 (1993).

8. Y. B. Zhao, D. M. Poirier, and R. J. Pechman, Appl. Phys. Lett. **64** (5), 577 (1994).

9. P. H. M. van Loosdrecht, P. J. M. Van Bentum, M. A. Verheijen, *et al.*, Chem. Phys. Lett. **198** (6), 587 (1992).

10. R. Lin and M. V. Klein, Phys. Rev. B **45** (19), 11437 (1992).

11. P. H. M. van Loosdrecht, P. J. M. Van Bentum, and G. Meijer, Chem. Phys. Lett. **205** (2,3), 191 (1993).

12. H. Watanabe, K. Takahashi, and M. Iwaki, Nucl. Instrum. Methods Phys. Res. B **80/81**, 1489 (1993).

13. A. F. Goncharov, Zh. Éksp. Teor. Fiz. **98** (5), 1824 (1990) [Sov. Phys. JETP **71**, 1025 (1990)].

14. A. V. Vasin, R. Yu. Holiney, L. A. Matveeva, *et al.*, in *Proceedings of the 4th International Symposium on Diamond Films and Related Materials, Kharkov, 1999*, p. 167.

15. Hisao-chu Tsai and D. B. Bogy, J. Vac. Sci. Technol. A **5** (6), 3287 (1987).

16. I. P. Soshnikov, A. V. Lunev, M. É. Gavevskiǐ, *et al.*, Zh. Tekh. Fiz. **70** (6), 98 (2000) [Tech. Phys. **45**, 766 (2000)].

Translated by P. Pozdeev

Remote Laser Probing of Hydrocarbons in the Atmosphere

V. E. Privalov and V. G. Shemanin

Baltic State Technical University, St. Petersburg, Russia
Received May 18, 2001

Abstract—A lidar equation for the Raman backscattering of light from molecules of some hydrocarbons was numerically solved. The optimum value of the copper vapor laser wavelength for the probing of hydrocarbons at a distance from 40 m to 4 km was determined. © *2001 MAIK "Nauka/Interperiodica".*

The laser probing of hydrocarbon molecules in the gas phase is of interest for the atmospheric pollution monitoring, technological gas control, and investigations in the optics of atmosphere [1]. Our previous investigations [2–4] aimed at the assessment of the potential of a Raman lidar for the pulsed laser probing of hydrogen and iodine molecules in the atmosphere. The results showed that the Raman lidar offers a promising means for the remote measurement of the concentrations of molecules in gas mixtures.

The purpose of this study was to numerically solve the lidar equation for the vibrational spectrum of the Raman backscattering from ethane, ethylene, and ethyl mercaptan under diurnal sounding conditions. Based on this modeling, we selected an optimum laser radiation wavelength ensuring a maximum power of the Raman scattering signal at the lidar detector. By comparing the results of calculation of the Raman scattering power measured by the lidar to the solar background radiation power, we estimated the minimum concentrations of hydrocarbon molecules detectable under the diurnal sounding conditions.

We have considered a lidar variant using the copper vapor laser operating at a wavelength of 578.2, 510.6, 298.1, and 255.3 nm and a sum wavelength of 271.2 nm at a peak power of up to 100 kW [5]. The hydrocarbons probed were selected taking into account both their structure (all molecules contain two carbon atoms) and maximum permissible concentrations (MPCs) for the atmospheric pollution monitoring [6]: ethane, 50 mg/m^3 (1.0×10^{15} cm^{-3}); ethylene, 3.0 mg/m^3 (6.5×10^{13} cm^{-3}); ethyl mercaptan, 1.5×10^{-3} mg/m^3 (3.5×10^{15} cm^{-3}).

The frequencies of intrinsic CH stretching vibrations of the molecules studied, taken from published data for C_2H_6 [7], C_2H_4 [1], and C_2H_4SH [8], are presented in the table. For ethyl mercaptan, we selected the CH stretching vibrations of CH_3 groups (2917 cm^{-1}) and SH stretching vibrations (2751 cm^{-1}), the latter characterized by an intensity five times smaller than the former [8]. Using these frequencies, we calculated the wavelengths λ_R of the Raman scattering bands of the

molecules studied for the selected laser wavelengths λ_0 (see table).

The differential cross sections ($d\sigma/d\Omega$) of the vibrational Raman backscattering for the selected laser wavelengths were determined (as descried in [3]) using the values experimentally measured for the wavelength $\lambda_0 = 337.1$ nm of a nitrogen laser [1] (see table). The cross section for ethane was estimated using the data for methane and butane [1], while the cross section of ethyl mercaptan was estimated using the Raman scattering intensities reported in [8], with an allowance for the data in [1].

The lidar equation for the Raman backscattering was taken in the form derived previously [2], with the values of parameters employed in [2, 3]. The numerical calculations of the Raman scattering power were performed for the same concentration of hydrocarbon molecules 10^{19} cm^{-3} and various sounding distances $R = 0.1, 0.5, 1.0, 2.0, 3.0, 4.0, 5.0,$ and 6.0 km. Similarly to what was done in [3], we determined the background
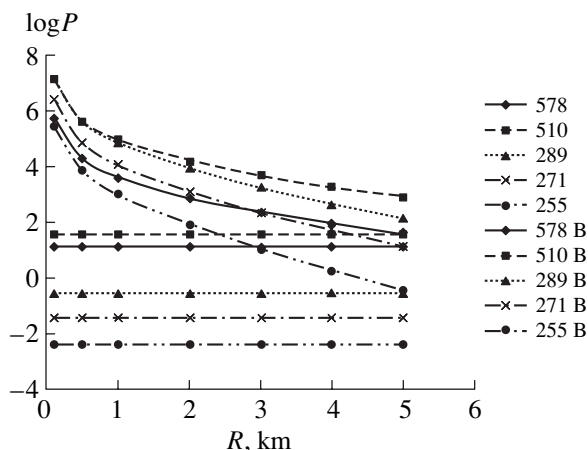

Fig. 1. Plots of the detected signal power logarithm versus probing distance for ethylene molecules at a concentration of 10^{19} cm^{-3} for the Raman backscattering at various wavelengths of the copper vapor laser. The horizontal lines show P_b, the minimum power levels detectable by a laser lidar under the experimental conditions studied.

Copper vapor laser radiation wavelengths (λ_0), intrinsic frequencies of the CH and SH stretching vibrations (ν), raman scattering wavelengths (R), and differential cross sections of the hydrocarbon molecules studied, and the relative spectral sensitivity of the electron multiplier photocathodes $\xi(\lambda)$, attenuation coefficients (k, k_0), and the spectral intensity of solar radiation S_b for various probing laser wavelengths

Ethane (C$_2$H$_6$)			$\nu = 3070$ cm^{-1}				
λ_0, nm	λ_R, nm	$(d\sigma/d\Omega) \times 10^{30}$, cm^2/str	k, km^{-1}	$\xi_p(\lambda)$	S_b, 10^6, W/(m^2 str nm)	k_0, km^{-1}	
578.2	697.3	5.4	0.15	0.16	5.2	0.16	
510.6	601.3	8.9	0.16	0.53	15.3	0.17	
289.1	316.1	86.8	0.38	0.35	7.23	0.53	
271.2	294.8	112.1	0.53	0.29	0.05	0.70	
255.3	276.1	142.7	0.58	0.15	0.03	1.91	
337.1	374.3	47.0					

Ethylene (C$_2$H$_4$)			$\nu = 3020$ cm^{-1}			
λ_0, nm	λ_R, nm	$(d\sigma/d\Omega) \times 10^{30}$, cm^2/str	k, km^{-1}	$\xi_p(\lambda)$	S_b, 10^6, W/(m^2 str nm)
578.2	694.0	9.4	0.15	0.18	5.56
510.6	598.8	15.5	0.16	0.53	15.48
289.1	315.4	151.0	0.39	0.35	7.17
271.2	294.2	195.0	0.54	0.29	0.05
255.3	275.6	248.4	0.59	0.15	0.03
337.1	373.3	81.8			

Ethyl mercaptan (C$_2$H$_4$SH)			ν CH $= 2931$ cm^{-1}			
λ_0, nm	λ_R, nm	$(d\sigma/d\Omega) \times 10^{30}$, cm^2/str	k, km^{-1}	$\xi_p(\lambda)$	S_b, 10^6, W/(m^2 str nm)
578.2	694.2	10.8	0.15	0.18	5.56
510.6	599.0	17.7	0.16	0.53	15.46
289.1	315.5	172.6	0.39	0.35	7.18
271.2	294.3	222.9	0.54	0.29	0.05
255.3	275.6	283.9	0.59	0.15	0.03
337.1	373.4	93.5			

Ethyl mercaptan (C$_2$H$_4$SH)			ν SH $= 2570$ cm^{-1}			
λ_0, nm	λ_R, nm	$(d\sigma/d\Omega) \times 10^{30}$, cm^2/str	k, km^{-1}	$\xi_p(\lambda)$	S_b, 10^6, W/(m^2 str nm)
578.2	694.0	14.3	0.15	0.18	5.56
510.6	598.8	23.5	0.16	0.53	15.48
289.1	315.4	229.0	0.39	0.35	7.17
271.2	294.2	295.7	0.54	0.29	0.05
255.3	275.6	376.5	0.59	0.15	0.03
337.1	373.3	124.0			

power at the detector $P_b(\lambda, R)$ and the minimum detected power P_m for the spectral intensity of solar radiation $S_b(\lambda)$ at various wavelength in the Raman scattering spectra of the molecules studied (see table).

Figure 1 presents the results of calculations for C$_2$H$_4$ molecules. For the comparison, the figure also gives the levels of the minimum detectable power P_b calculated for each lidar wavelength under the particular experi-
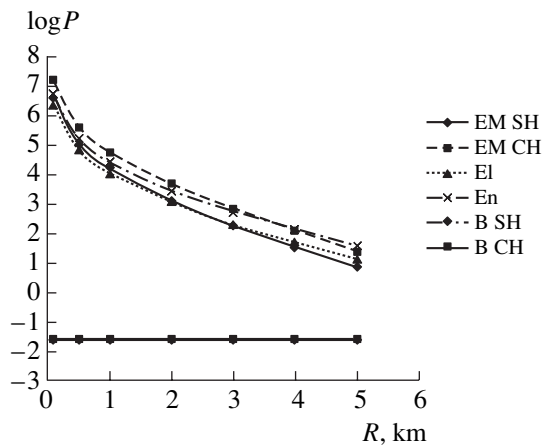
Fig. 2. Plots of the detected Raman backscattering power logarithm versus probing distance for ethyl mercaptan (EM), ethylene (El) and ethane (En) molecules at a concentration of 10^{19} cm^{-3} probed at a wavelength of 255 nm. The horizontal line shows P_b, the minimum power level detectable by a laser lidar operating at the given wavelength under the experimental conditions studied.

higher for the CH bands of ethyl mercaptan and ethane than for the same band of ethylene). Using the data on MPCs, we may estimate the maximum distances at which the molecules studied can be detected by a laser lidar at a concentration on the MPC level. The best results are expected for ethane and ethylene probed at 289 and 271 nm (4 and 1.5 km, respectively), while ethyl mercaptan probed at 271 nm can be detected at distance of 40 m using the CH band and only at 30 m using the SH band.

Thus, the optimum performance in the lidar system studied is provided by a copper vapor laser operating at a wavelength of 271.2 nm, which ensures the detection of all three hydrocarbons at a concentration on the MPC level.

mental conditions [4]. The Raman backscattering power exceeds the background level for a hydrocarbon concentration of 10^{19} cm^{-3} in the entire range of sounding distances only for a wavelength of 255 nm.

Figure 2 shows the results of calculations for all molecules at a concentration of 10^{19} cm^{-3} probed at a laser wavelength of 255 nm in the same sounding range. An analysis of these data indicates that a maximum Raman backscattering power for all distances is obtained at a probing wavelength of 255 nm for the CH Raman band of ethyl mercaptan. A somewhat smaller detected power is obtained for the SH band of ethyl mercaptan and the CH band of ethane, and a still lower value is observed for ethylene. For all molecules, the detected power exceeds the background level (which is

REFERENCES

1. R. M. Measures, *Laser Remote Sensing: Fundamentals and Applications* (Wiley, New York, 1984; Mir, Moscow, 1987).
2. V. E. Privalov and V. G. Shemanin, Opt. Spektrosk. **82** (4), 700 (1997) [Opt. Spectrosc. **82**, 650 (1997)].
3. V. E. Privalov and V. G. Shemanin, Proc. SPIE **3345**, 6 (1998).
4. V. E. Privalov and V. G. Shemanin, Opt. Atmos. Okeana **11** (2–3), 237 (1998).
5. S. A. Vitsinskiĭ, V. D. Divin, A. V. Keller, *et al.*, Opt. Zh. **63** (5), 83 (1996) [J. Opt. Technol. **63**, 401 (1996)].
6. *List and Codes of Substances Polluting Atmospheric Air* (Nauchn. Issled. Inst. Okhrany Atmosfernogo Vozdukha, St. Petersburg, 1992).
7. W. F. Murphy, W. Holzer, and H. J. Bernstein, Appl. Spectrosc. **23** (3), 211 (1969).
8. L. M. Sverdlov, M. A. Kovner, and E. P. Krainov, *Vibrational Spectra of Polyatomic Molecules* (Nauka, Moscow, 1970; Wiley, New York, 1974).

Translated by P. Pozdeev

Effect of the Metal–Semiconductor Phase Transition on the Capacitance of an Aluminum–Dielectric–Vanadium Dioxide Heterostructure

A. A. Bugaev, S. E. Nikitin, and E. I. Terukov*

Ioffe Physicotechnical Institute, Russian Academy of Sciences, St. Petersburg, 194021 Russia
* e-mail: eug.terukov@pop.ioffe.rssi.ru
Received June 9, 2001

Abstract—The temperature dependence of the electric capacitance of an aluminum–dielectric–vanadium dioxide heterostructure was studied. The capacitance exhibits a jumplike change in the region of the metal–semiconductor phase transition temperature. A qualitative model is suggested that relates a change in the capacitance to a jump in the conductivity of vanadium caused by the phase transition. © *2001 MAIK "Nauka/Interperiodica"*.

Despite a large number of investigations devoted to both theoretical [1–5] and applied [5] aspects of the metal–semiconductor phase transition in vanadium dioxide (VO_2), the prospects of practical implementation of this phenomenon still attract the attention of researchers. The main interest in the applied research was related to a significant ($\Delta n \sim 1$, $\hbar\omega = 1.17$ eV) reversible variation of the complex permittivity of vanadium dioxide in a broad interval of the optical spectrum, which led to the development of a reversible holographic medium [6, 7] and a passive optical gate for pulsed lasers [8, 9]. A much smaller number of investigations were related to the jump in the electric conductivity, which may reach (for the VO_2 film structures) up to 10^3–10^4 in the order of magnitude.

The purpose of this study was to develop a new capacitive element for optoelectronics, the capacitance of which would change in response to the thermal or optical action upon vanadium dioxide. The basic idea is to use a VO_2 film as the active plate of a capacitor, the conductivity of which changes depending on the temperature. This possibility opens up prospects for creating adjustable electronic circuits of a new type.

The samples were prepared on insulating substrates representing standard 15-μm-thick mica plates (dielectric permittivity 5–6) with an area of 4 cm². Using the method of thermal deposition in vacuum, one side of the mica plate was coated with a ~2000-Å-thick layer of aluminum and the other, with a ~1000-Å-thick layer of metallic vanadium. Then, the vanadium layer was oxidized in air at 420°C, which resulted in the formation of an oxide film with the composition close to VO_2 [7].

The experimental procedure consisted in measuring the standard temperature dependence of the VO_2 film conductivity. Simultaneously, we measured the temperature dependence of the electric capacitance of the Al–

mica–VO_2 structure. The measurements were performed at a frequency of 1 MHz using an indium electrode with an area of 0.06 cm² pressed against the center of the VO_2 film.
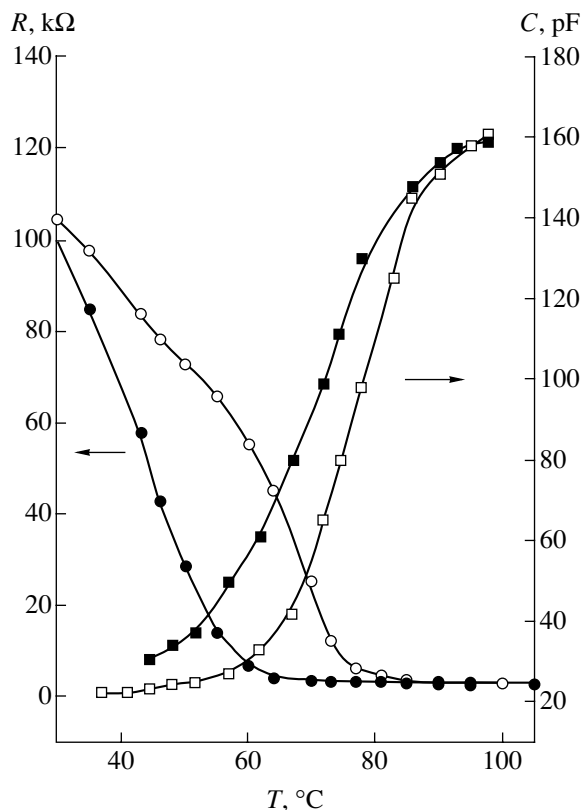
Temperature variation of the VO_2 film resistance (circles) and the Al–mica–VO_2 structure capacitance (squares). Open and filled symbols correspond to heating and cooling of the sample, respectively.

The results of the electrical measurements are presented in the figure. As can be seen from these experimental data, the cyclic (heating–cooling) temperature variation is accompanied both by the well-known pattern of changes (hysteresis loop) in the resistance of VO_2 [5] and by an analogous behavior of the electric capacitance. While the VO_2 film resistance changes by a factor of 20–30, the capacitance of the heterostructure studied varies only 6–7 times. Note that the control experiments with an analogous structure in which the VO_2 film was replaced by aluminum (i.e., with an Al–mica–Al capacitor) showed no significant change in the sample capacitance measured in the same temperature interval. Thus, we may ascertain that it is a change in the resistivity of VO_2 that accounts for the observed variation in capacitance of the Al–mica–VO_2 structure.

In order to explain the phenomenon of capacitance variation, we must take into account that the resistivity of VO_2 in both semiconductor ($\rho_s \approx$ 2–5 Ω cm) and metallic ($\rho_m \approx 10^{-3}$ Ω cm) states is significantly greater than the resistivity of typical "classical" metals. For this reason, the VO_2 film is both a capacitor plate and a resistor. Therefore, the sample circuit can be represented as an RC circuit with distributed parameters. The circuit comprises a small initial capacitance C_0 (Al–mica–In electrode) connected to the distributed RC chain (Al–mica–VO_2 film). The harmonic electromagnetic oscillations in this system are described by the equations of telegraphy for a line with losses [10].

The sample is conveniently represented as a thin disk with the indium electrode placed at the center of the VO_2 plate. For this two-dimensional distributed chain with radial symmetry, solving the equations of telegraphy reduces to the one-dimensional case. Dependence of the voltage between capacitor plates U on the distance r from the central electrode is described by an exponent

$$U = U_0 \exp - [\gamma r], \qquad (1)$$

where U_0 is the voltage on the central electrode and γ is the damping constant. In the case studied, the sample inductance and the insulator loss currents can be taken equal to zero. Under these assumptions, the damping constant γ can be expressed as

$$\gamma = (Ri\omega C)^{1/2}, \qquad (2)$$

where R and C are the chain resistance and capacitance in the region from 0 to r, respectively, and ω is the frequency of electromagnetic oscillations.

As can be seen from relationships (1) and (2), a significant resistance R (VO_2 in the semiconducting state) makes γ large and the electric field localized in the central region near the capacitor axis. In this case, only a small part of the VO_2 film in the vicinity of the central electrode is effective. For small R (VO_2 in the metallic state), γ sharply decreases and the region occupied by the electric field grows. This is equivalent to an increase in the effective area of the VO_2 plate.

Thus, a jumplike change in the conductivity of VO_2 related to the metal–semiconductor phase transition leads to a sharp variation of the electric field distribution in the sample structure, which is equivalent to a change in the effective capacitor plate area. In concluding, it should be noted that the conductivity of VO_2 may vary under the action of short laser pulses [5]. This effect allows the structure studied to be considered as a prototype of new light-controlled elements for optoelectronic circuits.

REFERENCES

1. N. F. Mott, *Metal–Insulator Transitions* (Taylor & Francis, London, 1974; Nauka, Moscow, 1979).

2. J. M. Honig and L. L. van Zandt, Annu. Rev. Mater. Sci. **5**, 225 (1975).

3. D. Adler and H. Brooks, Phys. Rev. **155** (3), 826 (1967).

4. D. Paquet and P. Leroux-Hugon, Phys. Rev. B **22** (11), 5284 (1980).

5. A. A. Bugaev, B. P. Zakharchenya, and F. A. Chudnovski, *Metal–Semiconductor Phase Transition and Its Application* (Nauka, Leningrad, 1979).

6. A. A. Bugaev, B. P. Zakharchenya, E. I. Terukov, and F. A. Chudnovski, in *Spatial Light Modulators*, Ed. by S. B. Gurevich (Nauka, Leningrad, 1977).

7. A. A. Bugaev, B. P. Zakharchenya, and F. A. Chudnovski, Kvantovaya Élektron. (Moscow) **6** (7), 1459 (1979).

8. A. A. Bugaev, B. P. Zakharchenya, and F. A. Chudnovski, Pis'ma Zh. Éksp. Teor. Fiz. **33** (12), 643 (1981) [JETP Lett. **33**, 629 (1981)].

9. A. A. Bugayev, F. A. Chudnovski, and B. P. Zakharchenya, in *Semiconductor Physics*, Ed. by V. M. Tuchkevich (Consultants Bureau, New York, 1986), pp. 265–293.

10. E. I. Manaev, *Principles of Radioelectronics* (Sov. Radio, Moscow, 1976).

Translated by P. Pozdeev

The Resonance IR Absorption in a "Metal–Thin Dielectric Layer–Diaphragm with Aperture" System

D. A. Usanov and S. S. Gorbatov

Saratov State University, Saratov, Russia

* e-mail: usanovda@info.sgu.ru

Received June 14, 2001

Abstract—It is established that a "metal–thin dielectric layer–diaphragm with aperture" system exhibits a resonance absorption in the IR spectral range. The effect is related to the interaction of the near field of the incident radiation, distorted by the aperture, with the reflecting metal surface. This phenomenon can be used to create adjustable IR filters. © *2001 MAIK "Nauka/Interperiodica".*

Previously [1], we described resonances in an iris–short system in a waveguide, spaced by a distance smaller than the wavelength of a radiation propagating in the waveguide by two orders of magnitude. The resonances were explained by the fact that high-order modes excited at the aperture obeyed the resonance condition for such distances from the short. Thus, the resonance were related to an interaction of the short (reflector) with the near field characterizing a distortion of the wave front incident on the iris aperture. Obviously, the effect of such interaction may be significant for a sufficiently small distance between the short and the iris with aperture, which was experimentally confirmed in the microwave range [1].

It was of interest to check for the possibility of analogous resonances being manifested at other frequencies, in particular, in the IR range. Below, we report on the results of such investigation. The experiments were performed with a system comprising two layers of an aluminum foil with a thickness of ≈0.5 μm, one of which had a rectangular slitlike aperture with dimensions 1×5000 μm. The metal films were separated by a dielectric layer representing the natural oxide films on the foil surfaces facing one another, with a total thickness of ~200 Å [2]. In the shortwave IR region, this spacing corresponds to ≈1/100 of the radiation wavelength.

The measurements of absorption of the IR radiation incident onto this structure were performed with the aid of an IKS-22 spectrophotometer. As can be seen from the results of these measurements presented in the figure, the resonance features actually take place in the wavelength range from 2 to 15 μm. The maximum

absorption was observed for the radiation with a wavelength of about 8 μm (curve *1*); additional absorption peaks were located at 4.5 and 12 μm.

A specific feature of the resonances described previously [1] was a shortwave shift in the characteristic frequencies with increasing distance between aperture and short in the waveguide. In order to confirm the hypothesis of analogy between the observed IR absorption resonances (see figure) and the phenomenon reported in [1], we repeated the measurements with the aluminum foils preliminarily oxidized for 2 min in water vapor so as to increase the dielectric (oxide) layer thickness. As expected, we observed a shift of the absorption
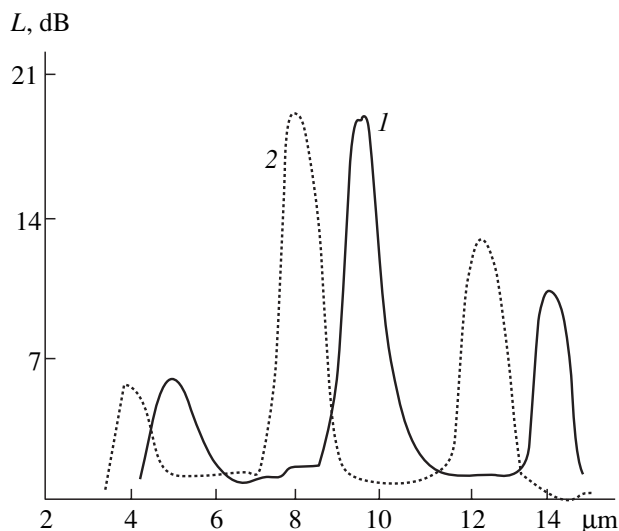

Figure.

curve by a approximately 2 μm toward shorter wavelengths (curve *2*).

Thus, we have established that a "metal–thin dielectric layer–diaphragm with aperture" system with specially selected aperture dimensions and the dielectric layer thickness may exhibits a resonance absorption in the IR spectral range. The effect is related to the interaction of the near field of the incident radiation, distorted by the aperture, with the reflecting metal surface. This phenomenon can be used, for example, to create adjustable IR filters.

REFERENCES

1. D. A. Usanov, S. S. Gorbatov, S. B. Wenig, and V. E. Orlov, Pis'ma Zh. Tekh. Fiz. **26** (18), 47 (2000) [Tech. Phys. Lett. **26**, 827 (2000)].

2. G. I. Bogda and M. M. Nekrasov, *Two-Dimensional Electronics and Semiconductor Integrated Circuits* (Vishcha Shkola, Kiev, 1979).

Translated by P. Pozdeev

Acoustic Energy Dissipation during Phase Separation in Oversaturated Solid Solutions

V. A. Plotnikov

Altai State University, Barnaul, Russia
e-mail: plotnikov@phys.dcn-asu.ru
Received June 4, 2001

Abstract—The phase separation in oversaturated solid solutions Al–4.0 at.% Cu and Al–6.5 at.% Zn is accompanied by an acoustic emission (AE). The AE signals were detected in the stage of formation of the concentration inhomogeneities (Guinier–Preston zones) in the former alloy and in the early phase separation stage in the latter. There are two possible mechanisms of the AE in the course of the phase separation: (i) dynamic energy relaxation related to spontaneous motions of the interphase boundary or (ii) plastic relaxation of the elastic energy related to the nucleation of misfit dislocations at the sites of coherency breakage. © *2001 MAIK "Nauka/Interperiodica".*

Introduction. As is known, an alloy possessing an excess (for a given temperature) concentration of one of the components occurs in the nonequilibrium state with an excess free energy and exhibits a tendency to separation of such an oversaturated solid solution. A driving force of this process is the decrease in the Gibbs free energy of the system [1]. The model of nucleation during the phase separation is based on the assumption that the new and initial phases are separated by a phase boundary (interface) leading to a local increase in the free energy, while the appearance of some volume of the new phase results in the overall decrease in the free energy due to the transition to a more stable state.

The phase decomposition is accompanied by the experimentally detected acoustic emission (AE), which is evidence that a part of the free energy is dissipated in this way. The purpose of this study was to elucidate mechanisms of the acoustic energy dissipation.

Sample preparation. The AE accompanying the phase separation of solid solutions was studied in alloys of the two systems: Al–Cu (with 4.0 at. % Cu) and Al–Zn (with 6.5 at. % Zn). The sample alloys were prepared by melting chemically pure components in a pure helium atmosphere in an electric-arc furnace.

This selection of alloys for the investigation was related to the fact that the Al–4.0 at. % Cu alloy exhibits the formation of disk-shaped concentration inhomogeneities (Guinier–Preston zones) in the early stage of phase separation, while the Al–6.5 at. % Zn alloy in the same stage shows spherical precipitates. Besides, the phase separation of solid solutions is known to proceed differently in the two systems—by nucleation and growth in the Al–4.0 at. % Cu alloy and by spinodal decay in the Al–6.5 at. % Zn alloy [1].

Oversaturation in the sold solutions was achieved by quenching the alloys from the temperatures corre-sponding homogeneous states of the solid solution. The Al–4.0 at. % Cu alloy was kept for 1 h at 570°C and quenched in water; the Al–6.5 at. % Zn alloy was also quenched in water but then stored in liquid nitrogen because of a high instability of the oversaturated slid solution.

AE measurements. The phase decomposition in the oversaturated solid solutions was studied in the course of continuous heating of the samples at a constant rate (about 1 K/s). Simultaneously, the AE was measured by a standard method described in [2].

Figure 1 gives fragments of the AE curves, representing variation of the signal intensity (count rate) dN/dt during the process, and shows the temperature variation with time. As can be seen, the AE from heated samples of the Al–4.0 at. % Cu alloy is manifested in the temperature interval from 30 to 250°C with a maximum at 150°C, while the same process in the Al–6.5 at. % Zn alloy is observed in the temperature interval from –50 to 100°C with a maximum at 70°C.

Analysis of results. The AE activation energy was determined by assuming that the phase decomposition of solid solutions can be described as the first-order reaction, with the reaction rate proportional to the AE intensity dN/dt. Thus, by comparing the AE intensity in Fig. 1 to the process temperature, we can determine the reaction rate constant k from the Arrhenius relationship $k = k_0\exp(-Q/KT)$, where Q is the activation energy, K is the Boltzmann constant, and T is the absolute temperature [2].

The results of analysis are presented in Fig. 2 and in the table. As can be seen in Fig. 2, the experimental points well fit to the straight line in the coordinates of $\ln[dN_i/dt/(N - N_i)]$ versus $10^3/T$. Here, N is the total count and N_i is the count by the time instant t_i. The table gives the AE activation energy and the correlation coef-
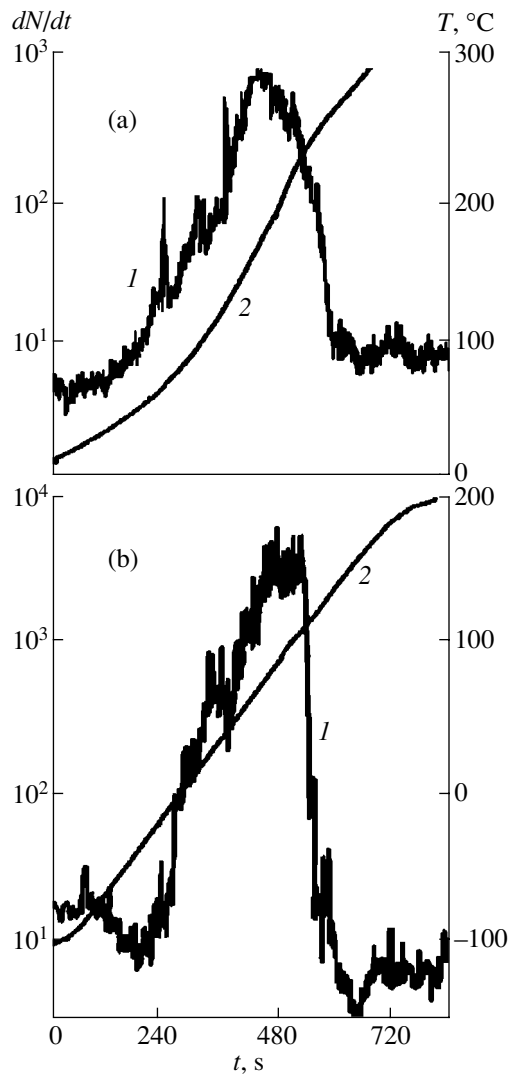
Fig. 1. The character of the acoustic emission manifestation during the phase separation of oversaturated solid solutions (a) Al–4.0 at. % Cu and (b) Al–6.5 at. % Zn in the course of annealing: (*1*) AE intensity (count rate) kinetics; (*2*) time variation of the sample temperature.

Fig. 2. Determination of the effective activation energy of the AE process accompanying the annealing of oversaturated samples of (a) Al–4.0 at. % Cu and (b) Al–6.5 at. % Zn alloys. Sold lines *1* show the linear approximation.

ficient. The correlation coefficient is close to unity and the activation energies are close to the analogous published data [3].

Discussion. The values of the activation energy indicate that the AE production is related to a process controlled by the diffusion of the corresponding alloy components in the initial aging stage. The acoustic effect accompanying the phase separation is evidence of a specific cooperative process involved in the formation of inhomogeneous zones. Such a cooperative process in the early aging stage can be spontaneous formation of the Guinier–Preston zones, followed by the spontaneous growth of these zones. The acoustic energy dissipation in this variant of the phase separation development is due to the dynamic energy relaxation related to spontaneous motions of the interphase boundary [4].
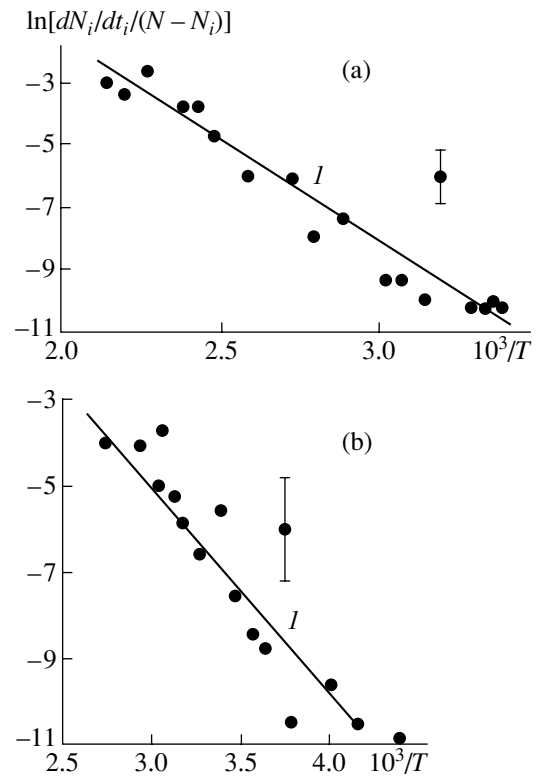
The nucleus–matrix interface is characterized by the atomic matching, which can be coherent, semicoherent, or completely incoherent. The shape of inhomogeneities (precipitates) can be needlelike, platelike, or spherical. It is important to note that the edges of needlelike and platelike precipitates are completely incoherent, in which case a mismatch between the crystal structures of precipitates and the matrix gives rise to the deformation energy. Relaxation of the elastic energy of deformation leads either to the formation of misfit dislocations or to the motion of dislocations and point defects. The latter case refers to the high-temperature precipitation processes, while the former process

Activation energies the AE accompanying the phase separation in oversaturated solid solutions Al–4.0 at. % Cu and Al–6.5 at. % Zn

Alloy	Temperature interval, °C	Activation energy, kJ/ mol	Correlation coefficient
Al–4.0 at. % Cu	30–150–250	54.9 ± 6.5	0.975
Al–6.5 at. % Zn	(–50)–70–100	44.0 ± 8.4	0.936

Note: The second value in the temperature interval indicates the position of maximum of the AE intensity.

takes place at low temperatures. The plastic deformation (plastic relaxation of the elastic energy) was experimentally observed in the stage of zone formation [1].

Conclusion. The analysis of the experimental results suggests that the acoustic energy dissipation during the phase separation in the oversaturated solid solutions studied may proceed by two mechanisms: (i) dynamic energy relaxation related to spontaneous motions of the interphase boundary or (ii) plastic relaxation of the elastic energy related to the generation of misfit dislocations as a result of coherency breakage at the interphase boundary.

REFERENCES

1. *Physical Metallurgy*, Ed. by R.W. Cahn and P. Haasen (North-Holland, Amsterdam, 1983; Metallurgiya, Moscow, 1987), Vol. 2.

2. V. A. Plotnikov, *The Nature of Acoustic Emission during Annealing of Metallic Materials* (Ed. of J. Izv. Vyssh. Uchebn. Zaved., Fiz., Tomsk, 1992); Available from VINITI, No. 686-B92.

3. Yu. I. Paskal' and K. V. Savitskiĭ, Izv. Vyssh. Uchebn. Zaved., Fiz., No. 1, 170 (1965).

4. V. A. Plotnikov, Pis'ma Zh. Tekh. Fiz. **25** (13), 15 (1999) [Tech. Phys. Lett. **25**, 512 (1999)].

Translated by P. Pozdeev

Calculation of the Temperature Gradient in the Melt Zone during the Electric-Transport Liquid Phase Epitaxy of Silicon Carbide Based Solid Solutions

B. A. Bilalov, G. K. Safaraliev, É. I. Idayatov, and G. D. Kardashova

Dagestan State University, Makhachkala, Dagestan, Russia
e-mail: dgu@dgu.ru; dgu@datacom.ru

Received April 2, 2001

Abstract—The temperature distribution in a growth cell and the temperature gradient in the melt zone during the electric-field liquid phase epitaxy of silicon carbide based solid solutions (ytterbium–gallium, ytterbium–aluminum) were calculated with an allowance for the growth cell geometry. The analysis was based on a solution of the stationary thermal conductivity equations in all five regions of the standard growth cell. The solution was obtained taking into account the following factors: (i) Joule's heating; (ii) Peltier's heating (cooling) at the electrode–source (substrate)–melt zone interfaces; (iii) contact heat liberated at the electrode–source (substrate) interface; (iv) dissolution heat; and (v) crystallization heat. Expressions for the temperature gradient ∇T in the melt zone as a function of the current density and the dimensions of regions in the growth cell are obtained. © 2001 MAIK "Nauka/Interperiodica".

The maximum time for attaining a stationary temperature distribution in the standard growth cell described in [1] can be determined from the relationship $\tau_T = l^2/(\pi^2 a)$ and is typically about 0.25 s. Here, l is the cell length; $a = \chi/(\rho c) \sim 10^{-5}$ m²/s is the thermal diffusivity coefficient; $\chi \sim 20$ W/(m K) is the thermal conductivity coefficient; $\rho \sim 5 \times 10^3$ kg/m³ is the density; and $c \sim 400$ J/(kg K) is the specific heat.

On the scale of a typical epitaxial layer growth time (30–60 min), the stationary temperature distribution in the growth cell can be considered as established instantaneously. Therefore, the temperature distribution in the growth cell can be determined by solving the stationary thermal conductivity equation in all five regions of the cell:

$$\chi_i \frac{d^2 T_i}{dz^2} + \rho_i j^2 = 0, \quad i = 1, 2, 3, 4, 5, \tag{1}$$

where χ_i, ρ_i, and T_i are the thermal conductivity coefficient, resistivity, and temperature of the ith region, respectively, and j is the electric current density in the growth cell.

We have solved the system (1) for the following boundary conditions:

$$T_1 = T_{ext}, z = -(d_1 + d_{e1}); \; T_1 = T_2, z = -d_l;$$

$$T_2 = T_3, z = 0; \; T_3 = T_4, z = d_m;$$

$$T_4 = T_5, z = d_m + d_s; \; T_5 = T_{ext}, z = d_m + d_s + d_{e5};$$

$$-\chi_1 \frac{dT_1}{dz} - \chi_2 \frac{dT_2}{dz} = \Pi_{21} j + R_{k1} s j^2 \quad \text{at} \quad z = -d_1,$$

$$\chi_2 \frac{dT_2}{dz} - \chi_3 \frac{dT_3}{dz} = \Pi_{32} j + Q_c \quad \text{at} \quad z = 0,$$

$$\chi_3 \frac{dT_3}{dz} - \chi_4 \frac{dT_4}{dz} = \Pi_{43} j - Q_m \quad \text{at} \quad z = d_m, \tag{2}$$

$$\chi_4 \frac{dT_4}{dz} - \chi_5 \frac{dT_5}{dz} = \Pi_{54} j + R_{k5} s j^2 \quad \text{at} \quad z = d_m + d_s.$$

Here, T_{ext} is the external (ambient) temperature; s is the electrode–source (substrate) contact area; Q_c and Q_m are the crystallization and dissolution (melting) heats, respectively; R_{k1} and R_{k5} are the contact resistances of the interfaces between regions 1–2 and 4–5; d_{e1}, d_{e5}, d_l, d_m, and d_s are the thicknesses of electrodes, substrate, melt, and source, respectively; and $\Pi_{ik} = \Pi_k - \Pi_i$ are the Peltier coefficients (positive, when Peltier's heat is liberated for the current passing through the interface from kth to ith region). It should be emphasized that the boundary conditions (2) refer to a standard growth cell with the normal to the interfaces parallel to the Z axis.

The resulting temperature distribution in the ith region of the growth cell can be presented in the following form:

$$T_i(z) = -\frac{1}{2}\frac{\rho_i}{\chi_i} j^2 z^2 + a_i z + b_i, \tag{3}$$

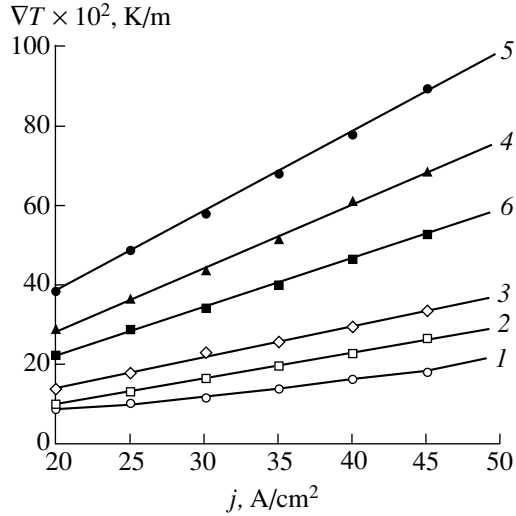where a_i and b_i are the integration constants. We obtained explicit expressions for a_i and b_i in all five

$\nabla T \times 10^2$, K/m

Fig. 1. Plots of temperature gradient ∇T versus current density j (curve numbers correspond to cell numbers in the table).
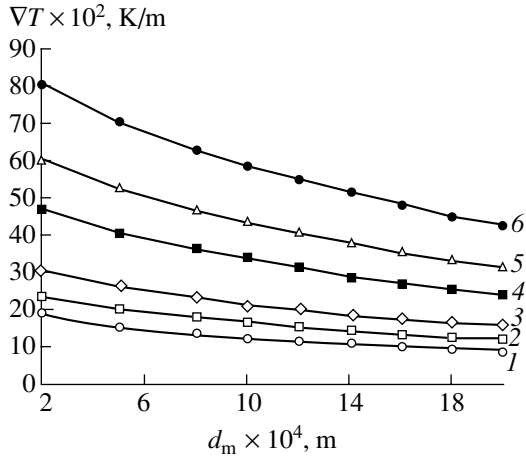
$\nabla T \times 10^2$, K/m

Fig. 2. Plots of temperature gradient versus melt zone thickness.

regions of the cell. The expressions are rather cumbersome and we present here only the formulas for a_3 and b_3:

$$a_3 = \frac{1}{\chi_3}\left\{\left(-\frac{d_{e1}}{\chi_1}(\Pi_{21} + \Pi_{32}) - \frac{d_1}{\chi_2}\Pi_{32} + \frac{d_s}{\chi_4}\Pi_{43}\right.\right.$$

$$+ \frac{d_{e5}}{\chi_5}(\Pi_{43} + \Pi_{54})\right)j - \left(\frac{d_{e1}}{\chi_1} + \frac{d_1}{\chi_2}\right)Q_c - \left(\frac{d_s}{\chi_4} + \frac{d_{e5}}{\chi_5}\right)Q_m$$

$$- \left(\frac{d_{e1}}{\chi_1}R_{k1} - \frac{d_{e5}}{\chi_5}R_{k5}\right)sj^2 - \left(\frac{1}{2}\frac{\rho_1}{\chi_1}d_{e1}^2 + \frac{1}{2}\frac{\rho_2}{\chi_2}d_1^2\right.$$

$$+ \frac{\rho_2}{\chi_1}d_{e1}d_1 - \frac{1}{2}\frac{\rho_3}{\chi_3}d_m^2 - \frac{\rho_3}{\chi_4}d_m d_s - \frac{\rho_3}{\chi_5}d_s d_{e5} \tag{4}$$

$$- \frac{1}{2}\frac{\rho_4}{\chi_4}d_s^2 - \frac{\rho_4}{\chi_5}d_s d_{e5} - \frac{1}{2}\frac{\rho_5}{\chi_5}d_{e5}^2\right)j^2\right\}$$

$$\times \left[\frac{d_{e1}}{\chi_1} + \frac{d_1}{\chi_2} + \frac{d_m}{\chi_3} + \frac{d_s}{\chi_4} + \frac{d_{e5}}{\chi_5}\right]^{-1};$$

$$b_3 = T_{ext} + a_3\left(\frac{\chi_3}{\chi_1}d_{e1} + \frac{\chi_3}{\chi_2}d_1\right)$$

$$+ \left[\frac{d_{e1}}{\chi_1}(\Pi_{21} + \Pi_{32}) + \frac{d_1}{\chi_2}\Pi_{32}\right] \tag{5}$$

$$+ \left(\frac{d_{e1}}{\chi_1} + \frac{d_1}{\chi_2}\right)Q_c + \frac{d_{e1}}{\chi_1}R_{k1}sj^2$$

$$+ \left(\frac{1}{2}\frac{\rho_1}{\chi_1}d_{e1}^2 + \frac{1}{2}\frac{\rho_2}{\chi_2}d_1^2 + \frac{\rho_2}{\chi_1}d_{e1}d_1\right)j^2.$$

Variation of the temperature T_3 and the temperature gradient ∇T_3 in the melt zone of the growth cell are given by the formulas

$$T_3(z) = -\frac{1}{2}\frac{\rho_3}{\chi_3}j^2 z^2 + a_3 z + b_3,$$

$$\nabla T_3(z) = -\frac{\rho_3}{\chi_3}j^2 z + a_3. \tag{6}$$

In order to elucidate the influence of various factors on the temperature distribution and gradient ∇T in the cell, we performed a comparative analysis of the contributions of various factors to expressions (6) based on formulas (4) and (5). The analysis showed that both Joule's and the Peltier effect, as well as the contact heat, may significantly influence the temperature and its gradient in the system studied. The contributions of Q_c and Q_m are lower by at least two orders of magnitude. Indeed, the former three factors may lead to $\nabla T_3 \approx (1-10) \times 10^2$ K/m, whereas an allowance for the Q_c and Q_m only gives $\nabla T_3 \approx 1$ K/m. However, the contributions due to the former three factors also significantly vary depending on the relative dimensions, the corresponding Peltier coefficients, and resistivities of the growth cell regions [2]. For example, the contact heat effect is significant when $R_{k1}\frac{d_{e1}}{\chi_1} \neq R_{k5}\frac{d_{e5}}{\chi_5}$, while Joule's heat contributes considerably provided that $\chi_2 \neq \chi_4$, $\rho_1 \neq \rho_5$, $\rho_2 \neq \rho_4$, and $\chi_1 \neq \chi_5$.

We have numerically calculated the values of temperature at the crystallization front T_k and the melting front T_m, and the temperature gradient in the melt zone for various relative dimensions of the growth cell regions and different conductivity types of the substrate and source (see table). The electrode thicknesses d_{e1} and d_{e5} varied from 1×10^{-3} to 8×10^{-4} m; the substrate thickness d_1, from 1×10^{-4} to 4×10^{-4} m; the melt thick-

ness d_m, from 1×10^{-3} to 5×10^{-4} m; and the source thickness d_s, from 1×10^{-4} to 4×10^{-4} m. The electric current density j varied within $(10–40) \times 10^4$ A/m^2. The other parameters used in the calculation were as follows: $T_{ext} = 1273$ K; $\chi_1 = \chi_5 = 33.43$ W/(m K), $\chi_2 = \chi_4 = 21.3$ W/(m K), $\chi_3 = 65.02$ W/(m K); $Q_c = Q_m = 0$; $\rho_1 = \rho_5 = 1.72 \times 10^{-6}$ Ω m, $\rho_2 = \rho_4 = 8 \times 10^{-5}$ Ω m, $\rho_3 = 4.74 \times 10^{-7}$ Ω m; $R_{k1} = R_{k5} = 0.01$ Ω.

The temperature gradient ∇T and the temperature difference $\Delta T = T_m - T_k$ depend significantly on the Peltier coefficient $\Pi = (\Pi_{43} + \Pi_{54}) - (\Pi_{21} + \Pi_{32})$. The maximum ∇T value obtained in the calculation was 10100 K/m (for $j = 50 \times 10^4$ A/m^2 and $\Pi = 3.2$ V). The corresponding temperature difference was 8.4 K. In agreement with the above considerations, the main contribution is due to the terms involving the Peltier coefficients (in all cases, the ∇T_3 value increases in proportion to the current density), while Joule's heat increases ∇T_3 rather insignificantly (Fig. 1). The drop of ∇T_3 with the melt zone thickness is mostly explained by the fact that an increase in the temperature difference $\Delta T = T_m - T_k$ (due to the growth in T_m and drop in T_k) is much smaller than the increase in d_m. Note that the dependence of ∇T_3 on d_m is nonlinear (Fig. 2).

We have also studied the dependence of ∇T on the substrate, source, and electrode thicknesses. As the substrate thickness grows, ∇T may either increase or decrease. This behavior is related to a decrease (increase) in the temperature at the crystallization front

The growth cell parameters (the Peltier coefficients and the substrate and source conductivity types) used in the calculation

Cell no.	Conductivity type	Π_{21}, V	Π_{32}, V	Π_{43}, V	Π_{54}, V
1	n–n	0.6	−0.7	0.7	−0.6
2	n–p	0.6	−0.7	1.2	−1.0
3	p–p	1	−1.2	1.2	−1.0
4	n–n	−0.6	−0.7	0.7	0.6
5	p–p	−0.4	−1.2	1.2	0.4
6	n–n	−0.4	−0.5	0.6	0.5

with increasing distance to the 1–2 region interface at which Peltier's heat is liberated (absorbed). By the same token, ∇T decreases (increases) when Peltier's heat is liberated (absorbed) at the 4–5 region interface. Similar considerations explain the dependence of ∇T on d_{e1} and d_{e5} values.

REFERENCES

1. V. N. Demin, Ya. M. Buzhdan, and F. A. Kuznetsov, in *Electric Transport and Its Applications* (Novosibirsk, 1982), pp. 75–79.

2. G. K. Safaraliev, B. A. Bilalov, and A. Z. Éfendiev, Zh. Tekh. Fiz. **54** (10), 2016 (1984) [Sov. Phys. Tech. Phys. **29**, 1181 (1984)].

Translated by P. Pozdeev

The Acoustic Emission
from a Nonlinearly Oscillating Charged Drop

A. I. Grigor'ev, S. O. Shiryaeva, A. R. Gaibov, and D. F. Belonozhko

Yaroslavl State University, Yaroslavl, Russia
e-mail: grig@uniyar.ac.ru
Received May 31, 2001

Abstract—A charged drop oscillating in a compressible medium is capable of emitting acoustic waves. According to calculations in the constant drop volume approximation linear in the oscillation amplitude, the most intense acoustic emission corresponds to the dominant mode. An acoustic dipole emission related to the excitation of a translational mode is only revealed by calculations in the second order of smallness with respect to the oscillation amplitude, in the case when two adjacent modes are present in the spectrum of initial deformations. © 2001 MAIK "Nauka/Interperiodica".

1. Investigations of the interaction of acoustic waves with liquid-drop systems frequently ignore the internal degrees of freedom related to the capillary oscillations of the drops. However, it is well known that the frequencies of such capillary oscillations of the drops with dimensions characteristic of some natural systems (fog, cloud, rain) fall within the frequency range of sound waves and longwave ultrasonic waves (see, e.g., [1–4] and references therein). The presence of an electric charge on the drops, deviation of the drop shape from spherical, motion of the drops relative to the medium, and an allowance for the drop viscosity lead to a shift of the spectrum of capillary oscillations toward lower frequencies [4–6], that is, to the region of acoustic waves detected by human ear.

2. In this context, we will consider the problem of an acoustic emission from an oscillating ideal incompressible electrically conducting liquid drop with the radius R, the density ρ_1, the surface tension γ, and the charge Q. The external medium is assumed to be ideally compressible and characterized by the sound velocity V, the permittivity ε, and the density ρ_2. The system will be described in a spherical coordinate system with the origin at the drop center. The wave motions in the drop and the medium are assumed to possess a potential character and are described by the velocity field potentials $\psi_1(\mathbf{r}, t)$ and $\psi_2(\mathbf{r}, t)$, respectively.

Since the initial perturbation of the drop surface is axisymmetric and small, we assume the drop shape to also be axisymmetric in both initial and all subsequent time instants. An equation describing the drop surface in the dimensionless polar coordinates such that $R = \rho = \sigma = 1$ with the origin at the drop center is

$$r(\theta, t) = 1 + \xi(\theta, t), \quad |\xi| \ll 1.$$

A system of equations describing evolution of the drop surface includes the Laplace equation for the velocity field potential $\psi_1(\mathbf{r}, t)$, the wave equation for the velocity field potential $\psi_2(\mathbf{r}, t)$, and the Laplace equation for the electrostatic potential $\Phi(\mathbf{r}, t)$:

$$\Delta\psi_1(\mathbf{r}, t) = 0; \quad \frac{1}{V^2}\frac{\partial^2\psi_2}{\partial t^2} - \Delta\psi_2 = 0;$$

$$\Delta\Phi(\mathbf{r}, t) = 0$$

and the boundary conditions

$$r \longrightarrow 0: \psi_1(\mathbf{r}, t) \longrightarrow 0;$$

$$r \longrightarrow \infty: \psi_2(\mathbf{r}, t) \longrightarrow 0; \quad \Phi(\mathbf{r}, t) \longrightarrow 0;$$

$$\frac{\partial\psi_2}{\partial r} + ik\psi_2 = o\left(\frac{1}{r}\right); \quad k = \omega/V;$$

$$r = 1 + \xi(\theta, t): \frac{\partial\xi}{\partial t} = \frac{\partial\psi}{\partial r} - \frac{1}{r^2}\frac{\partial\xi}{\partial\theta}\frac{\partial\psi}{\partial\theta};$$

$$\Delta p - \frac{\partial\psi}{\partial t} - \frac{1}{2}(\nabla\psi)^2 + \frac{1}{8\pi}(\nabla\Phi)^2 = \mathrm{div}\,\mathbf{n};$$

$$\Phi(r, t) = \Phi_s(t).$$

To close the above system, we use the conditions of conservation of the total charge Q and the drop volume $v = 4\pi/3$, as well as the condition of immobility of the center of mass:

$$-\frac{1}{4\pi}\oint_S (\mathbf{n} \cdot \nabla\Phi)ds = Q,$$

$$S = [r = 1 + \xi(\theta, t), 0 \leq \theta \leq \pi, 0 \leq \phi \leq 2\pi];$$

$$\int_v r^2(dr)\sin\theta\, d\theta\, d\phi = \frac{4}{3}\pi,$$

$$v = [0 \leq r \leq 1 + \xi(\theta, t), 0 \leq \theta \leq \pi, 0 \leq \phi \leq 2\pi];$$

$$\int_v \mathbf{e}_r \cdot r^3 dr \sin\theta \, d\theta \, d\phi = 0,$$

$$v = [0 \le r \le 1 + \xi(\theta, t), \, 0 \le \theta \le \pi, \, 0 \le \phi \le 2\pi].$$

The initial conditions are set so as to specify a virtual deformation of the equilibrium spherical drop, with the zero initial velocities of all points of the drop surface:

$$t = 0: \xi_0 P_0(\mu) + \xi_1 P_1(\mu) + \varepsilon \sum_{i \in \Xi} h_i P_i(\mu);$$

$$\frac{\partial \xi(\theta)}{\partial t} = 0; \tag{1}$$

$$\sum_{j \in \Xi} \alpha_j = 1; \quad \mu = \cos\theta.$$

In the above relationships, Ξ is the set of numbers of the initially excited modes; Δp is the constant pressure jump between inside and outside of the drop in the equilibrium state; $\mathbf{n}$ is the unit vector of normal to the drop surface; $\mathbf{e}_r$ is the radial unit vector of the spherical coordinate system; $\Phi_s(t)$ is the potential (constant over the drop surface); ε is the amplitude of the initial perturbation of the drop surface; $P_j(\mu)$ is the Legendre polynomial of the jth order; and ξ_0 and ξ_1 are constants determined from the conditions of the constant drop volume and the center-of-mass immobility at the initial time instant. To within the terms of the second order of smallness in ε, the latter quantities are given by the formulas

$$\xi_0 \approx -\varepsilon^2 \sum_{j \in \Xi} \frac{h_j}{(2j+1)} + O(\varepsilon^3);$$

$$\xi_1 \approx -\varepsilon^2 \sum_{j \in \Xi} \frac{9jh_{j-1}h_j}{(2j-1)(2j+1)} + O(\varepsilon^3).$$

3. Solution of the above problem by standard methods in the approximation corresponding to first order of smallness with respect to the amplitude of capillary oscillations leads to the following dimensional dispersion equation:

$$\omega_j^2 = (j-1)\frac{\sigma}{R^3}[W - (j+2)]$$

$$\times \left[\frac{(\rho_2/\rho_1)h_j^{(2)}(k_j R)}{k_j R h_{j-1}^{(2)}(k_j R) - (j+1)h_j^{(2)}(k_j R)} - \frac{1}{j} \right]^{-1};$$

$$W \equiv \frac{Q^2}{4\pi\varepsilon\sigma R^3},$$

where $h_j^{(2)}$ is the spherical Hankel function of the second kind ($j \ge 2$) and k is the wavenumber.

The roots of this equation can readily be found by numerical integration. The first two roots correspond to capillary oscillations decaying as a result of the energy losses for the acoustic wave emission. Upon determining the potential $\psi_2(\mathbf{r}, t)$ of the velocity field in the medium outside the drop, one may simply calculate the acoustic emission intensity (note that the center of mass of the oscillating drop is immobile). In the infinite set of sound radiators represented by the drop, the main contribution is related to the quadrupole emission of the dominant mode ($j = 2$).

Consider a raindrop with $R = 250$ μm oscillating upon excitation of the dominant intrinsic mode ($j = 2$) with an amplitude of $C_2 = 0.1R$ (according to [7, 8], the oscillation amplitude of raindrops can be quite large, up to $C_2 \approx R$). For $\sigma = 73$ dyn/cm, $\rho_1 = 1$ g/cm^3, $\omega_2 \approx 5.3 \times 10^3$ s^{-1}, $k_2 \approx 0.16$ cm^{-1}, $k_2 R \approx 4 \times 10^{-3}$, $\rho_2 = 1.3 \times 10^{-3}$ g/cm^3, $V = 3.3 \times 10^4$ cm/s, and $W = 1$, the total intensity of the acoustic emission from the drop at the dominant oscillation mode is readily calculated using the formula [9]

$$I = \rho_2 V \oint \overline{v^2} ds$$

$$\approx \frac{4\pi\rho_z V C_2^2 R^2 \omega^2}{\left| k_2 R h_1^{(2)}(k_2 R) - 3h_2^{(2)}(k_2 R) \right|^2} \approx 7.6 \times 10^{-16} \text{ erg/s.}$$

Assuming in this model consideration that a cubic kilometer of the rainy space accommodates 3×10^{14} raindrops with $R = 250$ μm (one drop per ≈ 3 cm^3), we readily obtain an estimate of the total acoustic emission intensity at the dominant oscillation mode of the raindrops contained in a space volume of 1 km^3: 0.23 erg/s at a frequency of $\omega_2 \approx 5.3 \times 10^3$ s^{-1}. This yields a sound level of ≈ 17 dB at the boundary of the emitting volume, which corresponds to a loud human whisper.

4. A solution to the problem formulated in Section 2 in the approximation corresponding to second order of smallness with respect to the amplitude of capillary oscillations can be obtained by the standard methods of the perturbation theory [10] (see, e.g., [11, 12]). This solution shows that the condition of immobility of the center of mass of the oscillating drop leads to excitation of the translational mode ($n = 1$), provided that two adjacent modes are present in the initial excitation spectrum.

An expression for the time variation of the translational mode amplitude for an oscillating drop in which the jth and $(j + 1)$th modes were initially excited is as follows (see also the figure):

$$M_1^{(2)}(t)$$

$$= -\varepsilon^2 R \frac{9j\alpha_{j-1}\alpha_j}{(2j-1)(2j+1)} \cos(\omega_j t) \cos(\omega_{j-1} t). \tag{2}$$

$M_1^{(2)}$

(a)

(b)
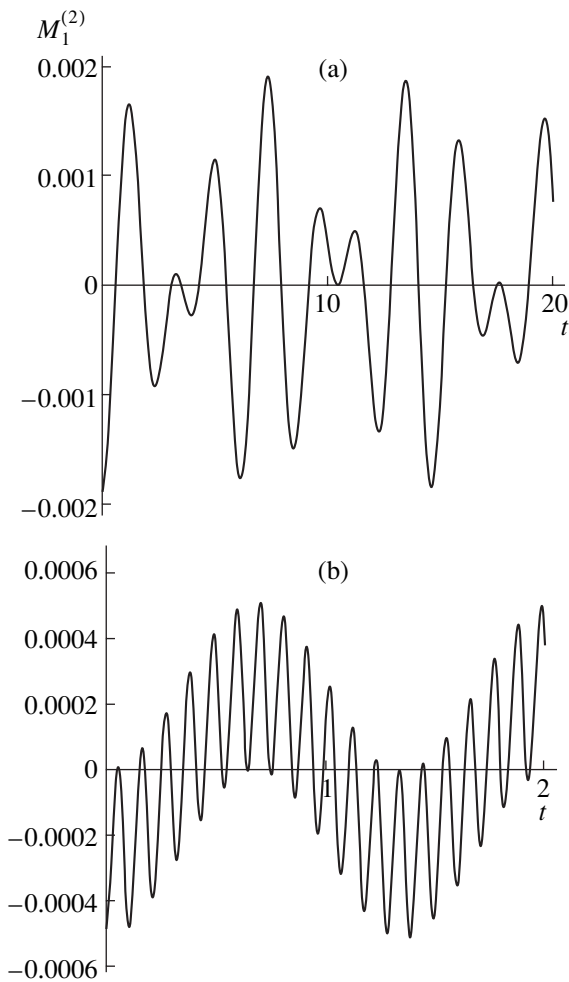
Plots of the dimensionless amplitude $M_1^{(2)}$ versus dimensionless time t for the translational mode ($n = 1$) of an oscillating drop. The initial deformation of the equilibrium spherical drop shape is set in the form of (a) $\varepsilon[P_2(\mu) + P_3(\mu)]/2$ and (b) $\varepsilon[P_{10}(\mu) + P_{11}(\mu)]/2$.

For a drop with the translational mode frequency ω_j and the radius comparable to $(\nu/\omega_j)^{1/2}$ (and such that $R(\omega_j/2\nu)^{1/2} \ll 1$), an expression for the intensity of the dipole acoustic emission in a compressible medium with a kinematic viscosity ν is as follows [9]:

$$I_d = \frac{3\pi\rho_2\nu^2 R^2\omega_j^2 U^2}{2V^3}, \qquad (3)$$

where U is the velocity amplitude for the points on the drop surface. Using relationship (2), we may readily

determine the U value. Substituting this quantity into formula (3) for the same values of parameters as above and assuming additionally that $j = 2$, $\varepsilon = 0.1$, $\nu = 0.15$ cm^2/s, and $\alpha_2 = \alpha_3 = 0.5$, we obtain an estimate of the acoustic dipole emission intensity related to the translational mode excitation: $I_d \approx 1.1 \times 10^{-14}$ erg/s. The integral emission from a 1-km^3 cloud would correspond to a sound level of ≈ 28 dB, which corresponds to a human speaking quietly.

5. Thus, we may conclude that the intensity of the acoustic dipole emission related to the translational mode excitation ($n = 1$) in an oscillating charged drop (manifested as a nonlinear effect in the second order of smallness with respect to the amplitude of capillary oscillations) is of the same order of magnitude as the intensity of the quadrupole emission related to the dominant mode excitation ($n = 2$) in the same drop in the approximation linear with respect to the oscillation amplitude.

REFERENCES

1. Won-Kyu Rhim, Sang Kun Chung, M. T. Hyson, *et al.*, IEEE Trans. Ind. Appl. **1A-23** (6), 975 (1987).
2. V. Sh. Shagapov, Izv. Akad. Nauk SSSR, Fiz. Atmos. Okeana **24** (5), 506 (1988).
3. E. H. Trinh, R. G. Holt, and D. B. Thiessen, Phys. Fluids **8** (1), 43 (1996).
4. A. I. Grigor'ev and S. O. Shiryaeva, Izv. Akad. Nauk, Mekh. Zhidk. Gaza, No. 3, 3 (1994).
5. S. O. Shiryaeva, Zh. Tekh. Fiz. **69** (8), 28 (1999) [Tech. Phys. **44**, 894 (1999)].
6. A. I. Grigor'ev, V. A. Koromyslov, and S. O. Shiryaeva, Zh. Tekh. Fiz. **70** (7), 26 (2000) [Tech. Phys. **45**, 840 (2000)].
7. V. V. Sterlyadkin, Izv. Akad. Nauk SSSR, Fiz. Atmos. Okeana **24** (6), 613 (1988).
8. K. V. Beard and Ali Tokay, Geophys. Res. Lett. **18** (12), 2257 (1991).
9. L. D. Landau and E. M. Lifshitz, *Mechanics of Continuous Media* (Gostekhteorizdat, Moscow, 1953).
10. A.-H. Nayfeh, *Perturbation Methods* (Wiley, New York, 1973; Mir, Moscow, 1976).
11. D. F. Belonozhko and A. I. Grigor'ev, Zh. Tekh. Fiz. **70** (8), 45 (2000) [Tech. Phys. **45**, 1001 (2000)].
12. S. O. Shiryaeva, Zh. Tekh. Fiz. **71** (2), 27 (2001) [Tech. Phys. **46**, 158 (2001)].

Translated by P. Pozdeev

Deformation-Induced Acoustic Emission from Porous Iron

V. V. Polyakov*, A. V. Egorov, and I. N. Svistun

Altai State University, Barnaul, Russia
* e-mail: polyakov@phys.dcn-asu.ru
Received June 18, 2001

Abstract—We studied the acoustic emission (AE) from mechanically loaded iron samples with a porosity of up to 30%. Dependence of the AE signal intensity (count rate) on the mechanical stress level was established for the samples possessing various structures. The curve of an informative AE parameter exhibits a non-monotonic variation with increasing porosity, showing an anomaly in the vicinity of the percolation threshold. © 2001 MAIK "Nauka/Interperiodica".

The use of structurally inhomogeneous materials in a mechanically loaded state requires thorough investigation of the plastic deformation and fracture of such materials under the working conditions. The presence of regions possessing sharply different properties and interfaces between these regions leads to certain features in the deformation behavior not encountered in homogeneous solids [1, 2]. A promising method for the study of deformation processes is offered by the acoustic emission (AE) [3, 4]. The purpose of this investigation was to establish the laws of AE from mechanically loaded iron-based porous materials.

The influence of a porous structure on the AE of inhomogeneous solids was studied using the samples prepared from iron-based metal powder of the PZhRV-2 grade. The sample structure was modified by changing the material porosity P from 5 to 30% in the course of pressing and sintering in vacuum (1450 K, 2.5 h). Variation of the sample porosity in this range ensured the obtaining of different topological patterns of the material structure, including the cases of isolated and "infinite" pore clusters as well as the percolation transition [5]. The structure of the initial powder and sintered metal samples was studied by optical metallography techniques using a Neophot-32 microscope. The AE from samples in the course of plastic deformation and fracture was measured with the aid of an automated setup [6] allowing the samples to be tested by tension at a fixed loading rate. An informative AE characteristic was represented by the count rate $\dot{N}$ of the AE oscillations.

The optimum testing regime was selected in a series of preliminary experiments performed at various loading rates. The experimental data were represented by the plots of $\dot{N}$ versus elastic stress σ. Figure 1 shows typical results obtained for three values of the stress variation rate $\dot{\sigma}$ = 0.9, 2.4, and 6.5 MPa/s, which demonstrate a significant influence of the loading regime on the acoustic emission from samples. At $\dot{\sigma}$ = 0.9 MPa/s, the AE curve reveals individual features of the material structure, which are manifested by chaotic peaks superimposed on the general $\dot{N}$ versus σ curve. An increase
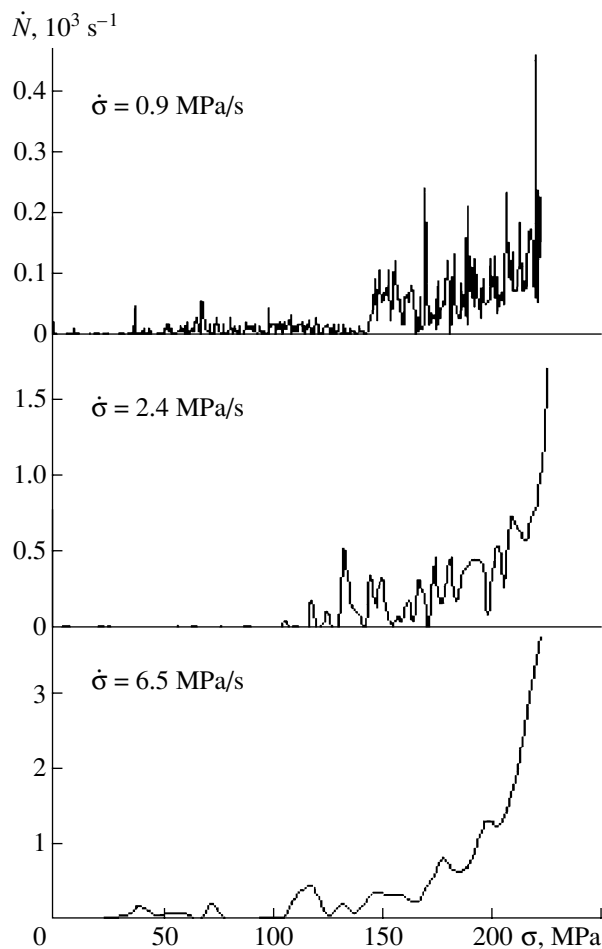

Fig. 1. The plots of AE signal count rate versus stress for iron samples with a porosity of 10% loaded at various rates.
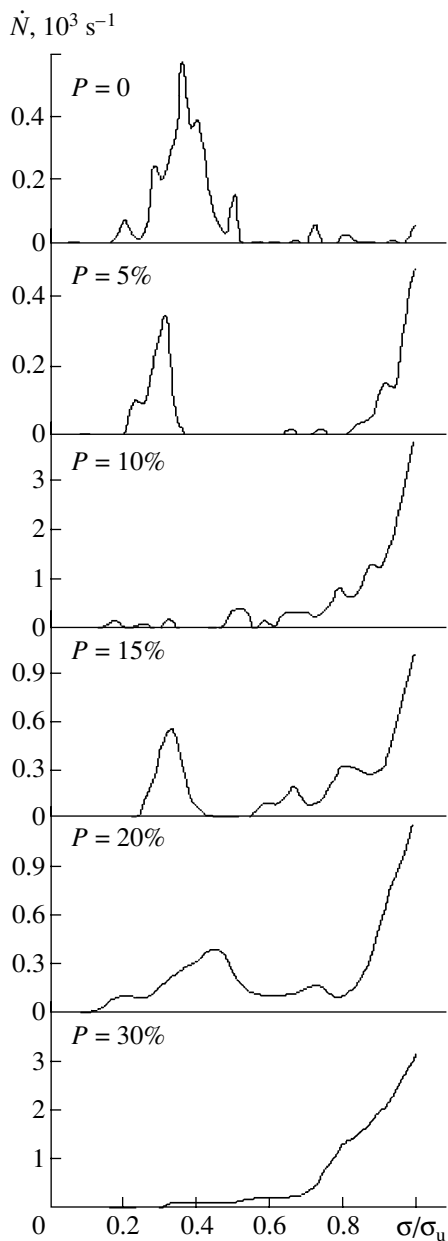
$\dot{N}$, 10^3 s^{-1}

Fig. 2. The plots of AE signal count rate versus stress for iron samples with various porosities (loaded at $\dot{\sigma}$ = 6.5 MPa/s).

in the $\dot{\sigma}$ value to 2.4 MPa/s reduced the random fluctuations in the signal count rate. The measurements at $\dot{\sigma}$ = 6.5 MPa/s provided stable results averaged over a large number of events. The latter value was selected for testing porous samples.

Figure 2 shows the results of measuring the AE signal count rate $\dot{N}$ during the deformation of iron-based samples with various porosities P. The $\dot{N}$ values are plotted versus σ/σ_u, where σ_u is the experimental ultimate tensile strength varying with the sample porosity:

σ_u = 350 MPa ($P = 0$), 260 MPa ($P = 5\%$), 240 MPa ($P = 10\%$), 170 MPa ($P = 15\%$), 110 MPa ($P = 20\%$), and 90 MPa ($P = 30\%$). The experimental results reflect a significant effect of the porous structure on the acoustic emission. For the compact metal sample ($P = 0$), the $\dot{N}$ versus σ curve is nonmonotonic, with a clearly pronounced maximum in the region of stresses corresponding to the yield point. Such curves are typical of the compact plastic metals [3, 4].

An increase in the material porosity to $P = 5\%$ led to a decrease in the $\dot{N}$ peak observed in the region of small stresses due to the plastic deformation of compact regions. In addition, the AE signal count rate exhibited a sharp increase immediately before fracture. For $P = 10\%$, the peak completely disappeared and the $\dot{N}$ value monotonically increased with σ. This behavior of the AE signal in the course of deformation is characteristic of the brittle fracture of a material featuring intensive cracking [4]. The passage to the brittle fracture is related to the fact that isolated pores act as effective local stress concentrators, whereby the fracture proceeds by the cracks propagating from one to another pore [1, 7].

As the sample porosity increased further ($P = 15\%$), the $\dot{N}$ versus σ curve became nonmonotonic again, acquiring a shape qualitatively similar to that observed for $P = 5\%$. However, the metallographic analysis showed that the mechanism of deformation is different from that operative in the case of low porosity. The formation and development of the open pores at $P \sim 10\%$ results in the early formation of microcracks at an insignificant plastic deformation of grains. Thus, the first peak can be interpreted as reflecting the formation of a network of microscopic cracks. These cracks are retarded at the boundaries of the porous space, which hinders the main crack development.

Figure 2 illustrates the gradual transition to a monotonic dependence of the AE signal count rate on the stress level when the porosity increases to $P = 20\%$. This can be explained by that a high porosity results in a significant "geometric" loss of strength caused by the presence of large number of voids. Finally, at $P = 30\%$, the main crack is developed virtually without any plastic deformation of the metal grains.

The results of our investigation elucidated the features of acoustic emission from loaded porous metals and revealed the influence of a porous structure on the mechanism of plastic deformation and fracture of such materials.

REFERENCES

1. V. V. Polyakov, G. V. Syrov, and A. V. Fadeev, in *Proceedings of the 4th European Conference on Advanced Materials and Processes, EUROMAT-95, Venice, Italy, 1995*, Vol. 4, p. 521.

2. V. E. Panin, V. V. Polyakov, G. V. Syrov, *et al.*, Izv. Vyssh. Uchebn. Zaved., Fiz., No. 1, 101 (1996).

3. V. A. Greshnikov and Yu. B. Drobot, *Acoustic Emission* (Izd. Standartov, Moscow, 1976).

4. A. S. Tripalin and S. I. Buĭlo, *Acoustic Emission. Physical and Mechanical Aspects* (Rost. Univ., Rostov-on-Don, 1986).

5. B. I. Shklovskiĭ and A. L. Éfros, Usp. Fiz. Nauk **117** (3), 401 (1975) [Sov. Phys. Usp. **18**, 845 (1975)].

6. V. V. Polyakov, V. V. Egorov, I. N. Svistun, *et al.*, Vestn. PGTU, No. 4, 133 (1999).

7. B. L. Baskin, R. K. Ivashchenko, A. M. Leksovskiĭ, *et al.*, in *Technological and Structural Plasticity of Powder Materials: Collection of Scientific Works* (IPM Akad. Nauk USSR, Kiev, 1988), pp. 93–97.

Translated by P. Pozdeev

Whispering Gallery Modes Induced in a Partly Shielded Hemispherical Dielectric Resonator

A. E. Kogut*, V. V. Kutuzov, V. A. Solodovnik, and S. N. Kharkovsky

Usikov Institute of Radiophysics and Electronics, National Academy of Sciences of Ukraine, Kharkov, Ukraine
* e-mail: kogut@ire.kharkov.ua
Received June 20, 2001

Abstract—Whispering gallery modes induced in a partly shielded hemispherical dielectric resonator by lumped radiation sources were experimentally studied for the symmetric and asymmetric arrangement of the hemisphere relative to the cylindrical metal shield. The oscillation mode characteristics are presented for the shielded hemispherical resonator and an analogous open dielectric resonator. The proposed resonator is a promising device for the creation of highly stable solid-state millimetric wave oscillators. © *2001 MAIK "Nauka/Interperiodica".*

Open dielectric resonators featuring whispering gallery (WG) oscillation modes possess unique properties in the millimetric wave range, including high intrinsic Q and relatively rare spectrum of induced oscillations [1]. These features make such resonators advantageous for the oscillator systems of active instruments and devices operating in the millimetric wave range [2].

However, devices based on the open dielectric resonators possess certain disadvantages as well, the open character being among these drawbacks. This feature leads to uncontrolled electromagnetic coupling to other elements of the system. Previously [3], we demonstrated that shielding of the open dielectric sphere by a metal cylinder with open ends allows the oscillating electromagnetic field to be localized inside the resonance system. For a certain relationship between dimensions of the sphere and cylinder, this resonance system allows excitation of the WG modes with the Q values exceeding (due to the field localization near the spherical surface of the dielectric) those attained with an analogous open dielectric resonator. In order to use such high-Q WG modes in practice (e.g., as the working modes of millimetric wave oscillators), it is necessary to study stability of the characteristics of these systems with respect to inhomogeneities and disorders in the resonator structure. For example, an asymmetry in spacing between the hemisphere and shield appearing during the fabrication and use of the shielded resonator system is equivalent to a diode introducing an inhomogeneity in the resonator field.

Our purpose was to study the WG modes in a partly shielded hemispherical dielectric resonator (SHDR) excited by an open waveguide end or a diode module via a coupling slot in the flat mirror. The analysis was performed for the cases of symmetric and asymmetric arrangement of the hemisphere relative to the shielding cylinder.

The system comprised a flat metal mirror 1 bearing a dielectric (teflon) hemisphere 2 with a diameter of 39 mm and a cylindrical (semicircle base with a radius of 42 mm) metal shield 3 with open ends (see the inset in Fig. 1). The flat mirror contains an excitation element 4 in the form of a coupling slot representing an open end of a rectangular waveguide (narrowing along the wide wall) or the output diaphragm of a 7.2×1 mm diode module. The system design includes, in addition to the Gunn diode proper, the necessary mount, adjustment, and power supply elements. The experimental prototype setup allowed the mutual arrangement of the symmetry planes of the dielectric hemisphere and the shielding meal cylinder to be gradually varied so as to
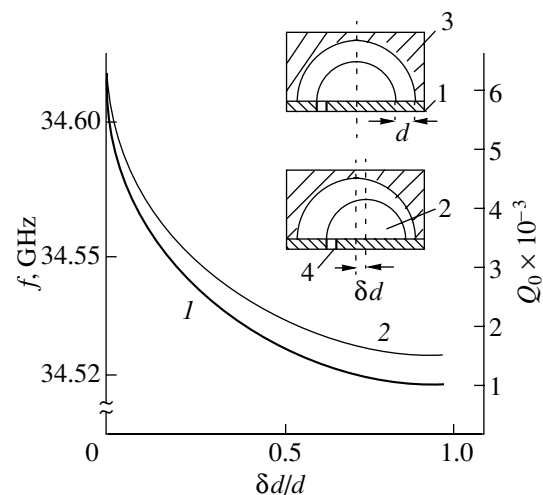

Fig. 1. Plots of the (*1*) intrinsic Q_0 and (*2*) resonance frequency f versus relative air gap asymmetry $\delta d/d$ for the WG modes of TM oscillations in the SHDR. The inset shows a schematic diagram of the SHDR studied (see the text for explanations).

make the air gap between resonator and shield asymmetric.

Figure 1 shows plots of the intrinsic SHDR quality factor Q_0 (curve *1*) and the resonance frequency f (curve *2*) versus relative displacement $\delta d/d$ of the dielectric hemisphere and the shield. The data refer to the excitation of WG modes of the TM oscillations at a frequency close to 34.55 GHz with a single field variation along the radial and azimuthal coordinate. The error of determination of the Q_0 values did not exceed 20%.

As can be seen from the data presented in Fig. 1, the maximum intrinsic Q_0 is attained for the WG modes excited in the SHDR with a symmetrically arranged dielectric hemisphere and metal cylinder. In this case, the quality factor ($Q_0 \approx 6 \times 10^3$) exceeds both the intrinsic quality factor for oscillations in the open hemispherical dielectric resonator (at a frequency close to that in Fig. 1, this amounts to 4.2×10^3) and the quality factor related to the energy losses in the dielectric. For the same SHDR with an asymmetric air gap, the Q_0 value decreases to become approximately equal to the value for the open hemispherical dielectric resonator already for $\delta d/d \approx 0.2$. As the resonance system asymmetry increases, the Q_0 of the SHDR drops further to become as low as 10^3 for $\delta d/d \approx 1$.

These results are explained by the influence of the metal shield on the WG modes excited in the dielectric resonator. Violation of the SHDR symmetry by changing the shield position relative to the dielectric hemisphere allows the resonance frequency of the WG modes to be reduced to within approximately 100 MHz (Fig. 1).

Figure 2 shows plots of the output power P and the oscillation frequency change δf versus the Gunn diode supply voltage U for SHDR with the symmetric and asymmetric arrangement of the dielectric resonator and metal shield. Curves *1* illustrate the behavior of a partly shielded resonator with the symmetric air gap and curves *2* refer to the case of an asymmetric resonance system with $\delta d/d \approx 0.7$. For comparison, curves *3* show the results of investigation of the oscillation characteristics of an analogous Gunn diode with the open dielectric resonator. The data were obtained by measurements performed near the SHDR resonance frequency of $f \approx$ 38.6 GHz. The output diaphragm arrangement of the diode module corresponded to a maximum oscillating field intensity in both shielded and open resonator.

As can be seen from Fig. 2, the SHDR with the symmetric air gap is characterized by a maximum output power and a minimum slope of the electronic frequency tuning $\delta f(U)$. These results agree with the Q_0 data and
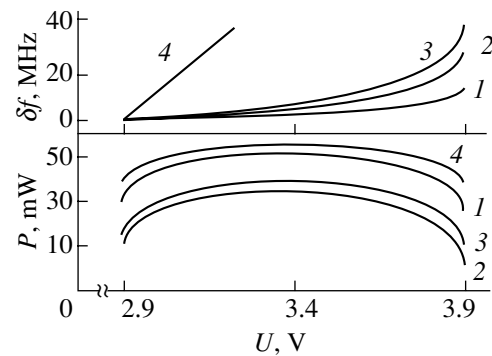

Fig. 2. Plots of the output signal power P and the frequency change versus power supply voltage U for the Gunn diodes (see the text for explanations).

can be explained by lower energy losses in the resonance system with the symmetric air gap as compared to the case of an open dielectric resonator or the same SHDR with asymmetric arrangement of the dielectric hemisphere and metal cylinder.

It should be noted that a displacement of the shield relative to the dielectric hemisphere did not lead to the frequency trapping in the neighboring oscillation bands. The working frequency gradually decreased with increasing the asymmetry, similarly to the case of measurement of the electrodynamic characteristics.

Thus, the results of our investigation demonstrated the possibility of exciting high-Q WG modes in a symmetric SHDR. The WG modes do not disappear when an asymmetry appears in the mutual arrangement of the dielectric resonator element and the metal shield; the WG frequency gradually decreases with increasing asymmetry. For the WG modes excited in the resonator described above, the output signal frequency and power stability level exceeded that achieved with an analogous open dielectric resonator.

REFERENCES

1. M. E. Il'chenko, V. F. Vzyatyshev, L. G. Gassanov, *et al.*, *Dielectric Resonators*, Ed. by M. E. Il'chenko (Radio i Svyaz', Moscow, 1989).

2. B. A. Kotserzhinskiĭ, E. A. Machusskiĭ, N. A. Pershin, and V. P. Taranenko, Izv. Vyssh. Uchebn. Zaved., Radioélektron. **30** (10), 13 (1987).

3. S. N. Kharkovsky, Yu. F. Filippov, Z. E. Eremenko, *et al.*, Pis'ma Zh. Tekh. Fiz. **25** (14), 20 (1999) [Tech. Phys. Lett. **25**, 558 (1999)].

Translated by P. Pozdeev

Optical Wavelet Processor for a Complex Signal Treatment

V. Yu. Petrunkin, E. T. Aksyonov, and G. A. Starikov

St. Petersburg State Technical University, St. Petersburg, Russia
Received June 21, 2001

Abstract—The expediency of creating optical wavelet processors capable of treating complex (in particular, noiselike) signals is justified. The results of treating phase-modulated signals with the aid of an optical wavelet processors are presented, which confirm the possibility of a real-time registration of the signal inhomogeneity. © 2001 MAIK "Nauka/Interperiodica".

The optical data processing systems are characterized by high operation rates determined, in fact, by dimensions of the input and output apertures and by the longitudinal system size. At present, the most promising data processing systems combine a fast optical processor, performing preliminary data treatment according to a preset algorithm, and an electronic digital processor accomplishing the following treatment stages. The possibilities of such hybrid systems can be increased, in particular, by developing and implementing new algorithms of the preliminary data treatment performed by the optical processor.

A promising direction of such development is related to using the optical processor for calculating a wavelet transform of a studied signal, with the formation of the corresponding time–frequency distribution. The wavelet transform provides for an effective analysis of nonstationary signals by facilitating separation and localization of the details and features of signals and images and determination of the characteristic scales of such details. In the analysis of wideband and nonstationary signals, the wavelet transform allows the features and inhomogeneities of such signals to be localized with high precision.

The wavelet transform consists in expanding a signal in a basis set formed from a localized function $\psi(t)$ by changing the scale with transfer [1]:

$$\psi_{\alpha, \beta}(t) = |\alpha|^{-1/2} \psi[(t - \beta)/\alpha]. \tag{1}$$

The integral wavelet transform of a function $f(t)$ is written in the following form:

$$[W_\psi f](\alpha, \beta) = |\alpha|^{-1/2} \int_{-\infty}^{+\infty} f(t) \psi^*[(t - \beta)/\alpha] dt$$

$$= \int_{-\infty}^{+\infty} f(t) \psi^*_{\alpha, \beta}(t) dt, \tag{2}$$

where the asterisk denotes complex conjugate. There is a considerable freedom in selecting a function generat-

ing the basis set of a wavelet transform (base wavelet). This is an important advantage, since a wavelet can be selected so as to facilitate the problem solution.

There are many functions employed for the base wavelet construction. One of these is the Morlet wavelet representing the product of a harmonic function by the Gauss function

$$\psi(t) = \exp(-t^2/2) \exp(i\omega_0 t),$$
$$\Psi(\omega) = \exp[-(\omega - \omega_0)^2/2]. \tag{3}$$

Here, $\psi(t)$ and $\Psi(\omega)$ are the Morlet wavelet and its Fourier image, respectively; i is the imaginary unity; and ω_0 is the frequency determining the number of oscillations of the harmonic function. The wavelet transform can be considered as a correlation or a convolution of the studied function (signal) with a set of analyzing wavelets (1). In optical systems, the wavelet transforms are calculated using various optical correlator schemes [2].

Modern communication and remote sensing systems widely employ complex, in particular, noiselike signals. The class of noiselike signals includes phase-modulated signals in which the carrier frequency phase is modulated according to a pseudorandom binary sequence. One of the tasks encountered in the analysis of such signals consists in creating a device capable of separating the phase jumps in the signal studied in the real time.

Our study is aimed at determining possibilities of the wavelet transform processing, establishing the promising fields of application of the optical wavelet processors, and formulating the concept of construction of such processors. We conducted experiments for assessing the possibility of separating the phase jump in phase-modulated signals with the aid of a wavelet transform.

The experiments were performed using a multichannel optical correlator with a spatial integration facility (Fig. 1a). In this setup, the light beam from a He–Ne laser ($\lambda = 0.6328$ μm) passing trough a beam expander is incident onto a mask situated in the entrance plane *3*
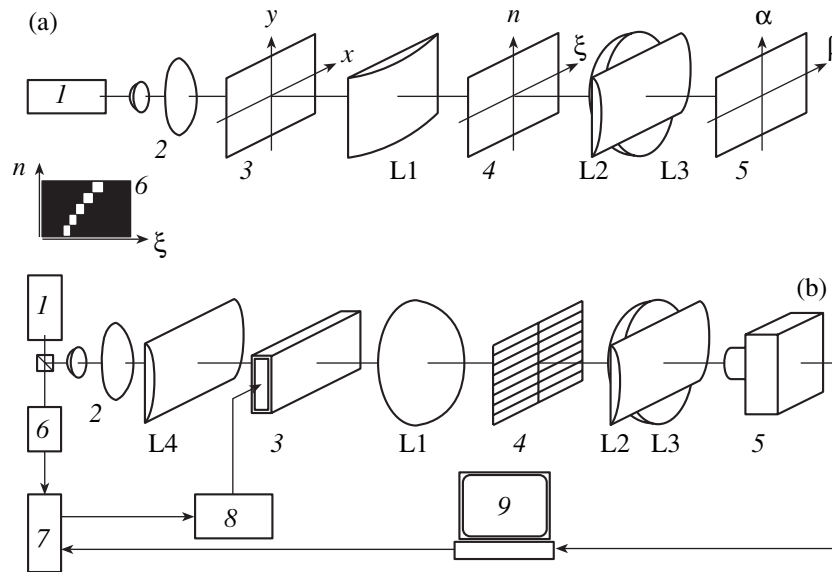
Fig. 1. Schematic diagrams of the optical wavelet processors used (a) in a model experiment and (b) for a real-time signal treatment. System (a): (*1*) He–Ne laser; (*2*) beam-forming unit; (*3*) entrance plane; (L1) cylindrical lens; (*4*) wavelet filter plane (ξ, spatial frequency; n, wavelet number); (L2, L3) lens system performing Fourier transform in the horizontal direction and imaging in the vertical direction; (*5*) exit plane; (*6*) mask fragment. System (b): (*1*) pulsed laser; (*2*) beam-forming unit; (L4) focusing lens; (*3*) acoustooptical modulator; (L1) spherical lens; (*4*) wavelet filter; (L2, L3) lens system performing Fourier transform in the horizontal direction and imaging in the vertical direction; (*5*) CCD-array TV-camera; (*6*) photodetector; (*7*) lock-in device; (*8*) signal source; (*9*) computer.

containing a model of the studied signal. In our experiments, the signal model was an amplitude mask with a periodic bar lattice. The lattice period was $100\,\mu m$, with a half-period phase jump in the middle. A cylindrical lens L1 provided the Fourier transform in the horizontal coordinate; mask *4* contained written Fourier images of the base wavelet, representing the Morlet wavelet [3]. The mask was manufactured with the required (Gaussian) transmission function approximated by a rectangular function [3]. A fragment of the mask is shown in the bottom left corner of Fig 1a (for clarity, only five frequency channels are depicted). A system of lenses L2 and L3 provided the Fourier transform in the horizontal direction and imaging in the vertical direction. The light field intensity distribution was registered at the system exit plane *5* with the aid of a CCD-array (TV-camera). The output signal from the camera was displayed on a monitor and fed to a computer for storage and processing.

The experimental procedure consisted in recording the light field intensity distribution in the exit plane of the optical system depending on the phase jump position in the input signal (in the entrance aperture). We have also studied the intensity distribution depending on the lattice period; a change in the spatial frequency was achieved by rotating the mask (modeling the input signal) about the vertical axis. The experimental results are presented in Fig. 2, which shows dependence of the intensity distribution on the phase jump position in the aperture (Fig. 2a) and on the spatial frequency of the input signal (Fig. 2b).

The most interesting task was the real-time signal processing. For the real-time operation, the experimental setup was modified as follows (Fig. 1b). The data input was provided by a lead molybdate based acoustooptical modulator. Past the beam expander, the light beam was focused on the acoustooptical modulator with a cylindrical lens L4; cylindrical lens L1 was replaced by a spherical one to compensate for the beam divergence in the vertical plane caused by lens L4. In addition, since the real-time wavelet transform recording requires fast-response detector system [3], the system was equipped with a pulsed laser ($\lambda = 0.531\,\mu m$) and computer-controlled lock-in device ensuring synchronization of the laser and signal source. The lock-in device introduced a preset delay between the signal front and the laser pulse, which allowed the results to be registered using the same camera with a CCD-array. The signal represented a sequence of two radio pulses with a carrier frequency of 38.5 MHz, a duration of $3.3\,\mu s$, and a phase difference of π.

The real-time experimental procedure consisted in recording the light field intensity distribution in the exit plane of the optical system depending on the time delay between the signal front and the laser pulse front. In addition, we studied the output signal in the case of simultaneous action of a pulsed phase-modulated signal and a continuous harmonic signal. The results are presented in Figs. 2c and 2d in the form of time–frequency distributions of the phase-modulated signal detected without interference and with a harmonic
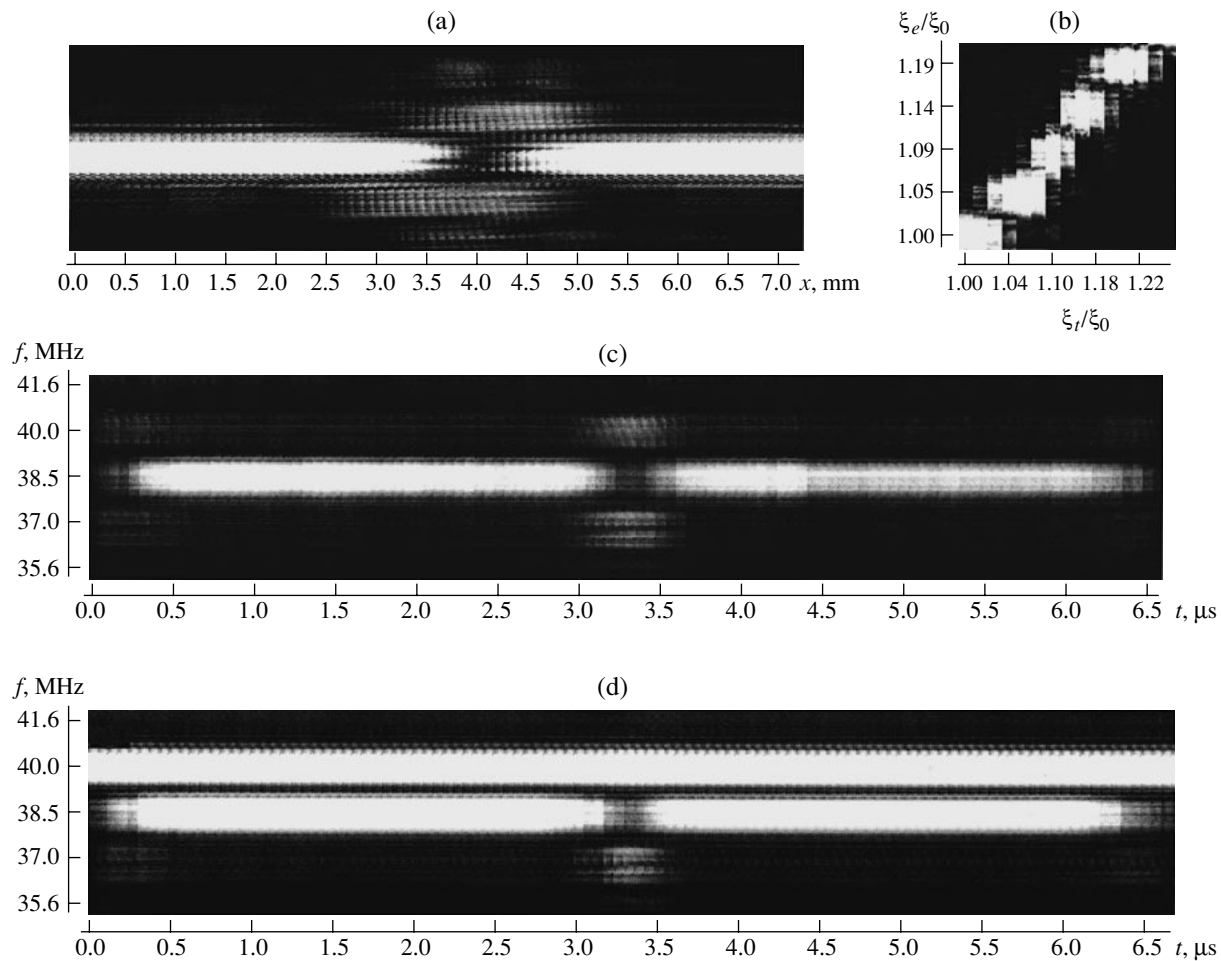
(a)

(b)

ξ_e/ξ_0

(c)

f, MHz

(d)

f, MHz

Fig. 2. Output signals of the wavelet processor in (a, b) a model experiment and (c, d) a real-time signal treatment: (a) horizontal axis indicates the phase jump coordinate *x*; (b) "experimental" spatial frequency ξ_e corresponding to the channel number versus "theoretical" spatial frequency ξ_t corresponding to the mask rotation angle (both normalized to the spatial frequency ξ_0 of the mask); (c, d) horizontal axis indicates the delay time *t* measured from signal front, vertical axis shows the central wavelet frequency *f* in the corresponding channel.

interference, respectively. As can be seen from Fig. 2d, the phase jump can be registered even in the presence of an intense harmonic interference signal with a close frequency.

Thus, we have studied the possibility of using an optical wavelet processor for analysis of the structure of noiselike signals. For the first time, a real-time optical wavelet processor was implemented using a pulsed laser synchronized with the studied signal. Based on the results of these experiments, we conclude that optical wavelet processors are promising systems for the real-time treatment of complex signals. The possibili-

ties of the wavelet processor can be markedly increased using a variety of the base wavelets.

REFERENCES

1. N. M. Astaf'eva, Usp. Fiz. Nauk **166** (11), 1145 (1996) [Phys. Usp. **39**, 1085 (1996)].

2. C. DeCusatis, J. Koay, D. M. Litynsky, and P. Das, Proc. SPIE **2643**, 17 (1995).

3. Yulong Sheng, Danny Roberge, and Harold H. Szu, Opt. Eng. **31** (9), 1840 (1992).

Translated by P. Pozdeev

The Birth, Annihilation, and Evolution of Nonparaxial Optical Vortices: 2. Topological Dipole

A. V. Volyar*, T. A. Fadeeva, and S. N. Lapaeva

Tauric National University, Simferopol, Crimea, Ukraine
* *e-mail: volyar@ccssu.crimea.ua*
Received April 23, 2001

Abstract—The events of the birth and annihilation of optical vortices in topologically neutral nonparaxial combined mode beams (topological dipoles) were studied. It is shown that there exists an extended domain of parameters of the elementary beams, for which the optical vortices of the dipole annihilate near the focal plane, thus restoring a wave field free of the wavefront dislocations. © 2001 MAIK "Nauka/Interperiodica".

The eigenmodes of an optical fiber represent the wavefields carrying optical vortices [1]. Even when a mode beam exciting the optical fiber is neutral (i.e., such that the sum of topological charges of the field is zero), very small perturbations of the fiber lead to the conversion of the principal mode energy into fields containing optical vortices in the bound state. The light emitted from a multimode fiber also carries a large number of bound vortices. As a result, the radiation exhibits a sharply irregular intensity distribution, which is called the speckle structure [2].

The vortex composition of the light beam emitted from a fiber significantly varies with distance from the exit edge. This is most clearly pronounced in a wave field radiated from a multimode fiber, observed near the focal plane of an output microobjective. Under certain conditions, the optical vortices disappear near the focal plane to appear again in the far radiation zone. The effect of the sudden disappearance and appearance of the phase singularities (dislocation reactions) of the initially smooth light field is characteristic of the nonparaxial laser beams observed near the focal caustic [3]. These dislocation reactions are manifested by the birth and annihilation of the anomalous Airy rings.

The purpose of this study was to describe the birth and annihilation of optical vortices in topologically neutral nonparaxial combined mode beam carrying two purely screw dislocations with topological charges of equal magnitude but opposite sign. Such singular states are termed the topological dipoles [4].

An analysis of the behavior of a nonparaxial topological dipole proceeds from the known shape of the wavefunction of the high-order mode beams satisfying the Helmholtz wave equation. In the first part of this study we showed that the wavefunction of a mode beam (reduced in the limiting case to the Laguerre–Gauss paraxial beams) can be composed of several elementary Legendre–Bessel beams. However, in the paraxial asymptotics ($kz_0 \gg 1$), this Ψ-function will match the

wavefunction of the corresponding paraxial beam either near the focal plane ($kz \ll 1$) or far from this plane ($kz \gg kz_0$) rather than on the whole optical axis.

Let us construct a new wavefunction of the combined mode nonparaxial beam:

$$\Psi^{(D)} = A\Psi^{(LB)}_{02} + B\Psi^{(ED)}_{11} + C\Psi^{(0)}_0, \tag{1}$$

where

$$\Psi^{(LB)}_{02} = \left(1 - \frac{2}{3}kz_0\right)j_0(kR) - \frac{1}{3}kz_0\left(2 - 3\frac{r^2}{R^2}\right)j_2(kR)$$

is the combined Legendre–Bessel beam matched near the focal plane ($kz \ll 1$) with the Laguerre–Gauss beam $\tilde{\Psi}^{(LG)}_{01}$; $\Psi^{(ED)}_{11} = \frac{r}{R}\cos\varphi\, j_1(kR)$ is the Legendre–Bessel beam with $m = l = 1$ matched on the whole optical axis with the paraxial beam $\tilde{\Psi}^{(ED)}_{10}$; $\Psi^{(0)}_0 = j_0(kR)$ is the principal Legendre–Bessel beam with $m = l = 0$ matched on the whole optical axis with the fundamental Gauss beam $\tilde{\Psi}^{(0)}_0$; $j_m(kR)$ are the mth order spherical Bessel functions of the first kind; and $R = \sqrt{r^2 + (z + iz_0)^2}$ is the complex radius of the beam.

In terms of expression (1), it is rather difficult to provide for a rigorous analysis of the vortex trajectories. For this reason, the distributions of intensity, amplitude, and phase of the wave will be constructed using the exact form of Eq. (1), while the vortex trajectories in the form of parametric curves will be determined using approximate Bessel functions $j_m(kR) \approx (i)^m j_0(kR)$ with $R \approx z + iz_0 + \frac{r^2}{2(z + iz_0)}$ and $r^2 = x^2 + y^2$ [5]. This approximation is valid with a high accuracy even for
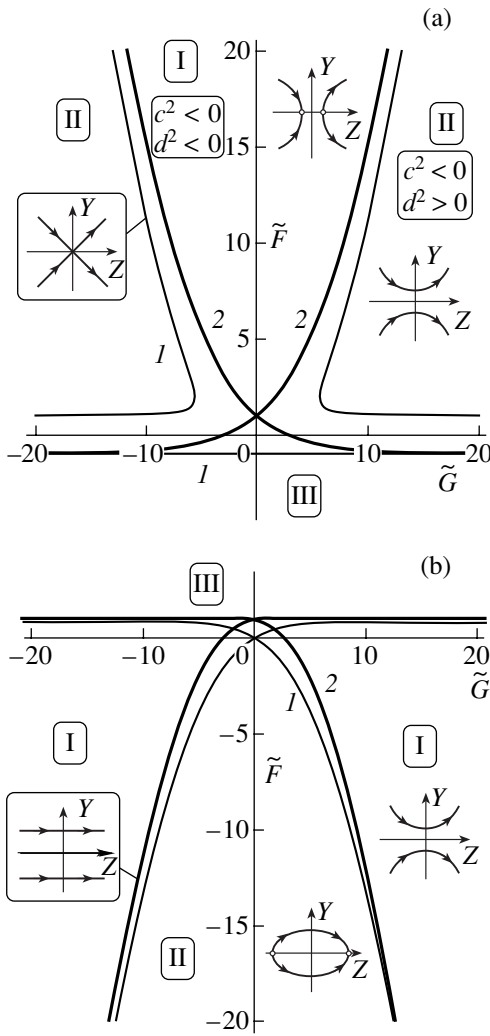
Fig. 1. Parametric curves of a (*1*) paraxial and (*2*) nonparaxial topological dipole for (a) real and (b) imaginary coefficient *B*.

relatively small values of $kz_0 \geq 10$ and $\frac{r}{z_0} < 1$. The most frequently encountered situations can be divided into two types, whereby the coefficient *B* in Eq. (1) is real or imaginary. Let us consider these cases separately in more detail.

1. The case of real *B*. Equating to zero the real and imaginary parts of Eq. (1) and subtracting the second equation from the first one, we obtain

$$(X - G)^2 + Y^2 + FZ^2 = 3F + G^2,$$
$$4F(1 + Z^2) + DX[2(1 + Z^2) + \mathcal{R}^2] = 0,$$

(2)

where

$$\mathcal{R}^2 = X^2 + Y^2, \quad F = \frac{A - C}{A(1 + kz_0) - C},$$

$$G = -\frac{B}{A(1 + kz_0) - C},$$

$$X = \frac{x}{z_0}, \quad Y = \frac{y}{z_0}, \quad Z = \frac{z}{z_0}.$$

In the paraxial approximation ($kz_0 \gg 1$) for $\tilde{Z} = 0$, we obtain

$$\tilde{X} = aX, \quad \tilde{Y} = aY, \quad \tilde{Z} = Z, \quad F \approx \frac{1}{a^2}\frac{1 - \tilde{F}}{2},$$

$$G \approx \frac{1}{a}\frac{\tilde{G}}{2}, \quad \tilde{F} = \frac{C}{A}, \quad \tilde{G} = \frac{B}{aA}, \quad a = \sqrt{\frac{kz_0}{2}}.$$

(3)

The paraxial Gauss beams are strictly determined only near the optical axis (i.e., for $r \ll z_0$). In this case, we may ignore the term $\mathcal{R}^2 \ll 1$ in the square brackets of Eq. (2). In addition, we can take into account that the wavefunctions of the paraxial and nonparaxial dipoles are equivalent only near the focal plane. Equation (1) describes a second-order surface, while the surface given by Eq. (2) significantly differs from a plane (especially in the vicinity of the origin). Nevertheless, for large values of the Rayleigh length ($kz_0 \gg 1$) or far from the focal plane ($kz \gg 1$), expression (2) is approximated by an equation of the plane $2F + DX = 0$. Near the origin, this surface exhibits a dome-shaped convexity in the positive (for $G < 0$) or negative (for $G > 0$) direction of the *z* axis. It is this convexity that determines the main distinctions in behavior of the paraxial and nonparaxial dipoles.

In order to analyze the behavior of the wave system on the parametric plane ($\tilde{F}$, $\tilde{G}$), we will use a paraxial transition to $kz_0 \gg 1$. With an allowance for approximation (3), exact expressions (2) acquire the following form:

$$\tilde{X}^2 + \tilde{Y}^2 + \frac{1 - \tilde{F}}{2}\tilde{Z}^2 = \frac{1 - \tilde{F}}{2}, \quad \tilde{G}\tilde{X} + 2(1 - \tilde{F}) = 0. \quad (4)$$

The topological dipole evolution is most conveniently described on the parametric plane ($\tilde{F}$, $\tilde{G}$). Here, the vortex trajectory in the parametric form can be written as

$$\tilde{Y}^2 - \frac{\tilde{Z}^2}{c^2} = d^2, \quad c^2 = \frac{2}{1 - \tilde{F}},$$

$$d^2 = \frac{1}{2}\left((1 - \tilde{F}) - 8\frac{(\tilde{F} - 1)^2}{\tilde{G}^2}\right).$$

(5)

The characteristic curves on the parametric plane are $d^2(\tilde{F}, \tilde{G}) = 0$ and $\tilde{F} = 1$. In Fig. 1a, curve *2* corresponds to the domain of variation of the dipole parameters corresponding to Eqs. (4). By the same token, curves *1* refer to the paraxial case not considered here. Obviously, the parametric curves show a discrepancy
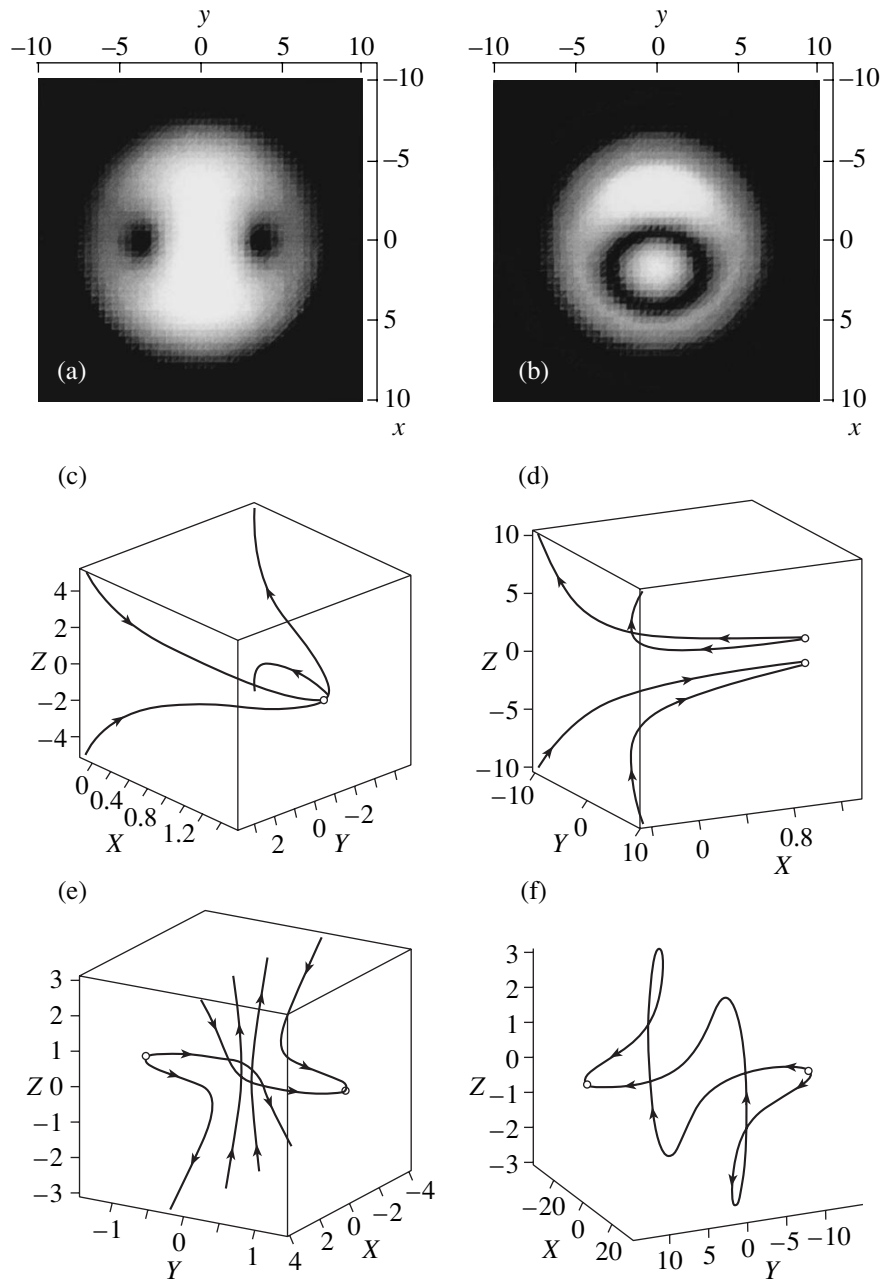
Fig. 2. (a, b) Light intensity distribution in a nonparaxial topological dipole and (c–f) optical vortex trajectories in a paraxial topological dipole with the parameters (c) $\tilde{F} = 5$, $\tilde{G} = 10$ and (d) $\tilde{F} = 510$, $\tilde{G} = 2$ for real B and (e) $\tilde{F} = 0.1$, $\tilde{G} = 15$ and (f) $\tilde{F} = 0.1$, $\tilde{G} = 18$ for imaginary B.

only for small values of the parameters $|\tilde{F}|, |\tilde{G}| \propto 1$; as the absolute values of the parameters increase, the results asymptotically coincide. Figure 2 shows a characteristic intensity distribution in the nonparaxial beam carrying a topological dipole in the case of a real quantity B. The vortex trajectories for various values of the parameters $\tilde{F}$ and $\tilde{G}$ were obtained by numerical computer analysis of the exact expressions for the corresponding surfaces.

2. The case of imaginary B. Repeating the general steps of the above analysis, we obtain analogous equations for the nonparaxial trajectories in this case:

$$\mathcal{R}^2 + 3FZ^2 + 2GXZ = F,$$
$$4FZ(1 + Z^2) + GX[2(1 + Z^2) - \mathcal{R}^2] = 0. \tag{6}$$

The parametric curve *2* in Fig. 1b agrees rather well with the analogous curve *1* representing events in

accordance with the parabolic wave equation. Although the curves for paraxial beams exhibit a good coincidence, there are significant discrepancies in the course of events in the nonparaxial beam.

Indeed, almost the whole parametric plane features a coincidence of the paraxial and nonparaxial behavior of the topological dipole with an imaginary coefficient B (Figs. 2e and 2f). At first glance, each cross section of the mode beam contains only two singular points corresponding to the dipole vortices. However, for relatively small values of $F < 1$, but with $G > 10$, the vortex trajectories possess four branches, two of which intersect the focal plane (Fig. 2e). Therefore, some of the beam cross sections contain four singular points. As the parameter F increases at a constant G, the four branches merge to form a single closed trajectory with an involved shape (Fig. 2f). Now, if the parameter F increases for a G value corresponding to the working point occurring inside the region II, the initial trajectory smoothly transforms into a quasi-elliptical. If the F value is fixed and G increases, the trajectories transform into quasi-hyperbolic vortex trajectories intersecting the focal plane. Thus, two vortices are born near the focal plane at $Z < 0$. These vortices propagate in the negative direction of the optical axis, exhibit reflection from the allowed zone boundary, intersect the focal plane, and eventually (after reflections from the opposite boundaries of the allowed zone) annihilate near the focal plane.

In concluding, it should be noted that a topologically neutral combined mode beam not carrying free optical vortices always has a large domain of parameters $\tilde{F}$ and $\tilde{G}$, for which a light field free of the bound vortex states exists in the vicinity of the focal plane $Z = 0$. Apparently, we may expect that, provided a unit optical vortex exists in the initial radiation and a topological dipole appears in the beam as a result of perturbation, the dipole vortices would annihilate in the vicinity of the focal crossover so as to restore the initial wave field.

REFERENCES

1. A. V. Volyar and T. A. Fadeeva, Opt. Spektrosk. **85** (2), 295 (1998) [Opt. Spectrosc. **85**, 272 (1998)].
2. B. Ya. Zel'dovich, N. F. Pilipetskiĭ, and V. V. Shkunov, *Wave Front Reversal* (Nauka, Moscow, 1985).
3. M. V. Berry, J. Mod. Opt. **45**, 1845 (1998).
4. A. V. Ilyenkov, L. V. Kreminskaya, M. S. Soskin, and M. V. Vasnetsov, J. Nonlinear Opt. Phys. Mater. **6** (2), 169 (1997).
5. A. V. Volyar, Pis'ma Zh. Tekh. Fiz. **26** (13), 71 (2000) [Tech. Phys. Lett. **26**, 573 (2000)].

Translated by P. Pozdeev

Large-Scale Magnetohydrodynamic Instability of a Conducting Liquid Surface

N. B. Volkov, N. M. Zubarev, and O. V. Zubareva

Institute of Electrophysics, Ural Division, Russian Academy of Sciences, Yekaterinburg, Russia
e-mail: nick@ami.uran.ru
Received July 2, 2001

Abstract—The stability of a current-carrying rectangular liquid metal conductor with respect to small longitudinal surface perturbations was theoretically studied. It is shown that the instability increment tends to zero in both short- and longwave limits and, hence, passes through a maximum at a finite wavenumber. The characteristic times of instability development are estimated. © *2001 MAIK "Nauka/Interperiodica".*

As is known [1, 2], the surface of a liquid metal conductor carrying electric current is unstable, predominantly featuring the development of shortwave perturbations. Our previous investigations [3–5] also showed that the action of Lorentz forces may lead to the convective magnetohydrodynamic instability development under certain conditions in conductors possessing a fixed boundary. In this case, perturbations with a wavelength on the order of a minimum characteristic size of the system will predominantly develop. The question as to how the possible nucleation of convective structures can influence the behavior of a conducting liquid with a free surface naturally arises. In this context, the purpose of our study was to analyze the dynamics of the boundary of a current-carrying liquid for a geometry where this influence can be significant and, in particular, to reveal mechanisms responsible for the development of large-scale surface instabilities.

Consider a liquid-metal conductor with a rectangular $2b \times 2a$ cross section ($a \ll b$) and sides a and b corresponding to the x and y coordinate axes, respectively. Let a constant electric current to flow in the direction of the conductor symmetry axis z (see figure). The liquid metal is assumed to be incompressible and possessing a constant conductivity σ. The magnetic hydrodynamic equations of this system are as follows:

$$\partial_t \mathbf{v} + (\mathbf{v} \cdot \nabla)\mathbf{v}$$
$$= -\rho^{-1}\nabla P + (4\pi\rho)^{-1}((\nabla \times \mathbf{H}) \times \mathbf{H}), \tag{1}$$

$$\partial_t \mathbf{H} + (\mathbf{v} \cdot \nabla)\mathbf{H} = (\mathbf{H} \cdot \nabla)\mathbf{v} + \nu_m \nabla^2 \mathbf{H}, \tag{2}$$

$$\nabla \cdot \mathbf{v} = 0, \quad \nabla \cdot \mathbf{H} = 0, \tag{3}$$

where $\mathbf{v} = \{v_x, v_y, v_z\}$, $\mathbf{H} = \{H_x, H_y, H_z\}$, and P are the velocity, magnetic field strength, and pressure, respectively; ρ is the density; $\nu_m = c^2(4\pi\sigma)^{-1}$ is the magnetic viscosity; and c is the speed of light. Let us represent the magnetic field and pressure as

$$\mathbf{H} = \mathbf{H}_0 + \mathbf{h}, \quad P = P_0 + p,$$

where $\mathbf{H}_0$ and P_0 are unperturbed (i.e., corresponding to the condition $\mathbf{v} = 0$) distributions of the magnetic field strength and pressure, respectively, and $\mathbf{h}$ and p are small perturbations. The $\mathbf{H}_0$ value is determined by the Biot–Savart law [6],

$$\mathbf{H}_0(x, y) = 2c^{-1}\int_s r^{-2}[\mathbf{j} \times \mathbf{r}_\perp]dS,$$

where $\mathbf{j} = \{0, 0, I/(4ab)\}$ is the current density (assumed to be homogeneously distributed), I is the total electric current through the conductor, $\mathbf{r}_\perp$ is the projection of the radius vector onto the conductor cross section ($\{x, y\}$ plane), and dS is the area element in this cross section. According to Eq. (1), in combination with the condition of constant pressure on the liquid surface, the function $P_0(x, y)$ is uniquely determined by the unperturbed distribution $\mathbf{H}_0$.

Assuming that the symmetry relative to the $y = 0$ plane is retained during the instability development (see [7]) and using relationships (1)–(3) in a linear
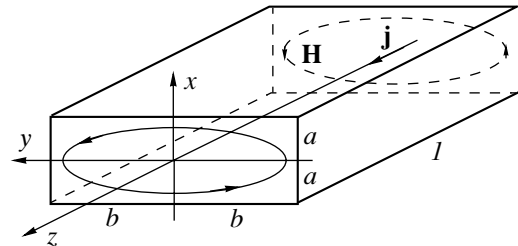
A schematic diagram illustrating the geometry of a rectangular liquid metal conductor ($2a \ll 2b \ll l$); curves with arrows represent the magnetic field lines.

approximation with respect to the perturbations **v**, p, and **h**, we obtain

$$\partial_t(\partial_z v_x - \partial_x v_z) = (4\pi\rho)^{-1}\partial_y H_{0x} \cdot \partial_z h_y,$$
$$y = 0, \tag{4}$$

$$\nabla^2(4\pi p + H_{0y}h_y)/2$$
$$= -(\partial_y H_{0x} - \partial_x H_{0y})\partial_y h_x + \partial_y H_{0x}\partial_z h_y, \quad y = 0, \tag{5}$$

$$(\partial_t - \nu_m\nabla^2)h_y = H_{0y}\partial_y v_y - v_x\partial_x H_{0y}, \quad y = 0, \tag{6}$$

where relationships (4) and (5) are obtained by applying "rot" and "div" operations, respectively, to Eq. (1). The boundary conditions for this system of equations are as follows:

$$h_y = \pm\partial_a H_{0y} \cdot \eta, \quad \partial_t\eta = \pm v_x, \quad p = \mp\partial_x P_0 \cdot \eta,$$
$$x = \pm a, \tag{7}$$

$$\pm 4\pi\rho\partial_t^2\eta = h_y\partial_x H_{0x} + H_{0y}\partial_y h_x - \partial_x(4\pi p + H_{0y}h_y),$$
$$x = \pm a, \tag{8}$$

where $\pm\eta(z, t)$ are small perturbations of the conductor surfaces $x = \pm a$ in the cross section by the plane $y = 0$.

Now, we will employ the presence of a small parameter a/b in the problem. In the main order of expansion with respect to a/b, the unperturbed magnetic field and pressure at the conductor symmetry plane $y = 0$ are as follows:

$$\mathbf{H}_0 = \left\{-\frac{2Iy}{cb^2}, \frac{\pi I x}{abc}, 0\right\}, \quad P_0 = \frac{\pi I^2(a^2 - x^2)}{2abc}. \tag{9}$$

Taking into account that the motion of liquid near the plane $y = 0$ can be considered as virtually two-dimensional (the characteristic scale of variation in y is much greater than the corresponding scales in the x and z axes), we introduce the current function $\psi(x, z, t)$ such that $\partial_z\psi = -v_x|_{y=0}$ and $\partial_x\psi = v_z|_{y=0}$. In addition, we introduce the functions $h(x, z, t) = h_y|_{y=0}$ and $4\pi\tilde{p}(x, z, t) = (4\pi p + H_{0y}h_y)_{y=0}$. Let us also neglect dependence of the magnetic field perturbation **h** on the variable y and omit the derivative $\partial_y h_x$ in Eqs. (5) and (8) (this derivative cannot be self-consistently determined from system (4)–(9)). Note that this is the only assumption adopted not following from the problem symmetry considerations. Upon converting equations into a dimensionless form with the aid of substitutions

$$\mathbf{r} \longrightarrow (2\rho\nu_m^2 ab^3 c^2 I^{-2})^{1/4}\mathbf{r}, \quad t \longrightarrow (2\rho ab^3 c^2 I^{-2})^{1/2}t,$$

$$\tilde{p} \longrightarrow \left(\frac{2\rho\nu_m^2 I^2}{ab^3 c^2}\right)^{1/2}\tilde{p}, \quad h \longrightarrow \left(\frac{2\pi^4\rho\nu_m^2 I^2}{a^3 bc^2}\right)^{1/4}h,$$

we exclude the spatial coordinate y and reduce Eqs. (4)–(6) to the following system of equations (in the main order of expansion with respect to a/b):

$$\partial_t\Delta_\perp\psi = \partial_z h, \tag{10}$$

$$\Delta_\perp\tilde{p} = -\partial_x h, \tag{11}$$

$$\partial_t h - \Delta_\perp h = \partial_z\psi, \tag{12}$$

where $\Delta_\perp = \partial_x^2 + \partial_z^2$ is the two-dimensional Laplace operator. The boundary conditions (7) and (8) at $x = \pm\alpha$ acquire the form

$$\tilde{p} = 0, \quad h = \mp\eta, \quad \partial_t\eta = \mp\partial_z\psi,$$
$$\partial_t^2\eta = \eta \mp 2\partial_x\tilde{p}, \tag{13}$$

where the quantity $\alpha = [(I^2 a^3)/(2\rho\nu_m^2 b^3 c^2)]^{1/4}$ plays the role of an external control parameter. Equations (10)–(13) form a closed system describing the instability development in a current-carrying liquid-metal conductor in the vicinity of the symmetry plane $y = 0$.

Let us turn to the linear analysis of instability of the liquid surface. For this purpose, the functions $\tilde{p}$, h, ψ, and η are conveniently presented in the following form:

$$\tilde{p}(x, z, t) = p'(x)e^{ikz + \delta t} + \text{c.c.},$$

$$h(x, z, t) = h'(x)e^{ikz + \delta t} + \text{c.c.},$$

$$\psi(x, z, t) = \psi'(x)e^{ikz + \delta t} + \text{c.c.},$$

$$\eta(z, t) = \eta'e^{ikz + \delta t} + \text{c.c.},$$

where k is the wavenumber and δ is the instability increment. Below, we assume δ to be real, which implies that the consideration is restricted to aperiodic surface instabilities. Substituting these expressions into Eqs. (10)–(13), we obtain a system of ordinary linear equations

$$d_x^2\psi' - k^2\psi' = ik\delta^{-1}h',$$

$$d_x^2 p' - k^2 p' = -d_x h',$$

$$d_x^2 h' - (k^2 + \delta)h' = -ik\psi'$$

with the boundary conditions at $x = \pm\alpha$

$$p' = 0, \quad h' = \mp\eta', \quad \psi' = \pm i\eta' k^{-1}\delta,$$
$$d_x p' = \pm\eta'(1 - \delta^2)/2.$$

Solving these equations, we find a relationship between the quantities δ and k (i.e., a dispersion relationship for the surface waves),

$$2k\tanh(k\alpha)\sum_{j=1}^{2}A_j\coth(s_j\alpha) = 1 - \delta^2, \tag{14}$$

where $s_{1,2} = (\delta/2 + k^2 \pm \sqrt{\delta^2/4 + k^2/\delta})^{1/2}$ and

$$A_1 = \frac{s_1(s_2^2 - k^2)}{(s_1^2 - k^2)(s_2^2 - s_1^2)}, \quad A_2 = -\frac{s_2(s_1^2 - k^2)}{(s_2^2 - k^2)(s_2^2 - s_1^2)}.$$

The complexity of the transcendental equation (14) hinders investigation of the general case, but we may find an explicit expression for the increment as a function of the wavenumber in the long- and shortwave approximations. Expanding Eq. (14) in powers of k or k^{-1}, respectively, we obtain in these limits, to within the terms of a higher order of smallness,

$$\delta = (\alpha/\pi)^4 k^2, \quad k \longrightarrow 0, \tag{15}$$

$$\delta = 2^{-1} k^{-2/3}, \quad k \longrightarrow \infty. \tag{16}$$

Here, we assumed $\delta \geq 0$; that is, we considered the unstable branch of the dispersion relationship. As can be seen from Eqs. (15) and (16), the instability increment δ tends to zero for both $k \longrightarrow 0$ and $k \longrightarrow \infty$. From this, we infer that δ is a nonmonotonic function of k and, hence, the increment acquires a maximum value δ_{max} (determined by the problem parameter α) at a certain finite wavenumber k.

Let us estimate the $\delta_{max}(\alpha)$ value. A rough estimate from above can be obtained from the intersection of asymptotes (15) and (16). The increments corresponding to these expressions coincide at $k = 2^{-3/8}(\pi/\alpha)^{3/2}$ and, hence,

$$\delta_{max}(\alpha) < 2^{-3/4} \pi^{-1} \alpha.$$

In order to estimate the δ_{max} value from below, we may compare the instability increments for the free-boundary problem under consideration and the fixed-boundary problem obtained from Eqs. (10)–(13) by putting $\eta = 0$. In the latter case, we may assume that $h' \sim \psi' \sim \sin(\pi x/\alpha)$. Substituting these relationships into Eqs. (10) and (12), we obtain the following algebraic characteristic equation:

$$\delta^2 + [k^2 + (\pi/\alpha)^2]\delta - k^2/[k^2 + (\pi/\alpha)^2] = 0. \tag{17}$$

For a positive root of this equation, determining the instability dynamics, the main-order asymptotics in the longwave limit coincides with (15) and in the short-wave limit, is represented by $\delta \longrightarrow k^{-2}$. This result implies that the maximum instability increments of the fixed-boundary problem, as well as that of Eq. (14), corresponds to a certain finite wavenumber k. Note that the increment for $k \longrightarrow \infty$ in this problem decays more rapidly than the increment (16) in the free-boundary problem. The same conclusion follows from a comparison of the higher orders of expansion in the power of k for the two increments in the limit of $k \longrightarrow 0$. From this, we may infer that, at any fixed k, the instability increment in the free-boundary problem under consideration is greater than that in the fixed-boundary problem. In other words, the possibility of deformation of the liquid surface accelerates the development of per-turbations. Therefore, the instability increment corresponding to (14) can be estimated from below as

$$\delta_{max}(\alpha) > \delta_0(\alpha),$$

where δ_0 is the maximum increment for Eq. (17). The δ_0 values and the wavenumbers k_0 for the most rapid spatial harmonics can be determined by jointly solving Eq. (17) with the condition $\partial_k \delta = 0$. In particular,

$$\delta_0 = (\alpha/2\pi)^2, \quad k_0 = \pi/\alpha, \quad \alpha \longrightarrow 0,$$

$$\delta_0 = 1, \quad k_0 = (\pi/\alpha)^{1/2}, \quad \alpha \longrightarrow \infty,$$

which implies that a characteristic scale of the convective excitation structure for small values of the control parameter ($\alpha \sim I^{1/2}$) is comparable to the conducting layer thickness a, while for large values of α, the small-scale spatial modes are most rapid. This conclusion is applicable to the case of a current-carrying liquid with the free boundary considered in our problem.

Thus, an analysis of stability of a rectangular liquid metal conductor showed that there exists a mechanism of development of the large-scale surface instability related to a convective magnetohydrodynamic instability of the current-carrying medium. Note that, in the case of a cylindrical conductor (in description of the stratification development in the initial stage of an electric explosion), it is necessary to take into account the surface tension in order to eliminate a divergence of the dispersion relationship in the shortwave limit [1, 2].

REFERENCES

1. K. B. Abramova, V. P. Valitskii, Yu. V. Vandakurov, *et al.*, Dokl. Akad. Nauk SSSR **167**, 778 (1966) [Sov. Phys. Dokl. **11**, 301 (1966)].

2. K. B. Abramova, N. A. Zlatin, and B. P. Peregood, Zh. Éksp. Teor. Fiz. **69**, 2007 (1975) [Sov. Phys. JETP **42**, 1019 (1975)].

3. N. B. Volkov, N. M. Zubarev, O. V. Zubareva, and V. T. Shkatov, Pis'ma Zh. Tekh. Fiz. **22** (13), 43 (1996) [Tech. Phys. Lett. **22**, 538 (1996)].

4. N. B. Volkov, N. M. Zubarev, O. V. Zubareva, and V. T. Shkatov, Physica D (Amsterdam) **109**, 315 (1997).

5. A. M. Iskoldsky, N. B. Volkov, N. M. Zubarev, and O. V. Zubareva, Chaos **6** (4), 568 (1996).

6. L. D. Landau and E. M. Lifshitz, *Course of Theoretical Physics,* Vol. 8: *Electrodynamics of Continuous Media* (Nauka, Moscow, 1982; Pergamon, New York, 1984).

7. N. B. Volkov, N. M. Zubarev, and O. V. Zubareva, Pis'ma Zh. Tekh. Fiz. **25** (10), 1 (1999) [Tech. Phys. Lett. **25**, 380 (1999)].

Translated by P. Pozdeev

High-Temperature Superconductor Based Composites: Large Magnetoresistance in Weak Magnetic Fields

D. A. Balaev[a,*], D. M. Gohfeld[a,b], S. I. Popkov[a,c], K. A. Saihutdinov[a], and M. I. Petrov[a]

[a] *Kirensky Institute of Physics, Siberian Division, Russian Academy of Sciences, Krasnoyarsk, Russia*
[b] *Siberian Aerospace Academy, Krasnoyarsk, Russia*
[c] *Krasnoyarsk State University, Krasnoyarsk, Russia*
* e-mail: smp@iph.krasnoyarsk.su
Received June 26, 2001

Abstract—It was found that high-temperature superconductor (HTSC) based composites of the 1–2–3 (YBCO) + dielectric and YBCO + normal metal types exhibit large magnetoresistances in weak magnetic fields in a broad temperature range. This behavior is qualitatively explained using the concept of the irreversibility line in HTSCs and the mechanism of thermal fluctuations in the network of weak bonds of the Josephson type realized in HTSC composites. The HTSC-based composites exhibit a much higher sensitivity (as compared to that in the usual HTSC ceramics) to weak magnetic fields (below 300 Oe) at liquid-nitrogen temperatures, which is important for practical applications. © *2001 MAIK "Nauka/Interperiodica".*

The resistivity ρ of polycrystalline high-temperature superconductors (HTSCs) at temperatures below the superconducting transition temperature T_c is highly sensitive to weak magnetic fields [1, 2]. This sensitivity is explained by dependence of the resistive state of such HTSCs on the state of grain boundaries representing weak bonds of the Josephson type [1–3] known to be very sensitive to external magnetic fields [4]. However, the temperature interval in which the HTSC ceramics exhibit a large magnetoresistance in weak magnetic fields is very narrow, typically amounting to several degrees (e.g., 85–90 K for the yttrium ceramics and 90–100 K for the bismuth ceramics [2]). This circumstance probably accounts for the fact that the above magnetoresistance effect in HTSC ceramics is insufficiently studied from the standpoint of practical applications. At the same time, extensively studied are the related materials such as the HTSC-based composites (see, e.g., [5–12]). These materials exhibit interesting transport [5, 6, 10, 12] and magnetic [9] properties. Below, we report on the results of our investigation of the magnetoresistance effect in weak magnetic fields in bulk composites of the HTSC + normal metal and HTSC + dielectric types.

The samples of composites were synthesized as follows. The 1–2–3 HTSC composition $Y_{3/4}Lu_{1/4}Ba_2Cu_3O_7$ (referred to below as YBCO) was prepared using a standard technology.[1] In the YBCO + dielectric composites,

the dielectric component was CuO of a special purity grade [13]. $BaPbO_3$ oxide obtained by solid-state synthesis from BaO_2 and PbO was used as the normal metal [14]. The mixtures of powdered components taken in stoichiometric proportions were thoroughly mixed in an agate mortar and pressed into tablets. The tablets were annealed according to the following schedule: 5min at 930°C and 6 h at 400°C for the composites with $BaPbO_3$; 2 min at 910°C and 3 h at 350°C for the composites with CuO. After the final annealing stage at 350–400°C, the samples were cooled down to room temperature with the furnace (for detail, see [10, 11]).

The X-ray diffraction investigation of HTSC-based composites showed only the reflections due to phases of the initial components, which was evidence of the absence of chemical interactions between these components. The electron-microscopic observation of HTSC-normal metal composites showed that an average size of the YBCO grains in this material was ~1.5 μm. The transport properties (resistivity below T_c, critical current, current–voltage characteristics) of the composites were reported in detail elsewhere [10–12]. The experimental data on the effect of a magnetic field on the resistivity of these materials are presented for the first time.

The $\rho(T)$ curves were measured using a standard four-point-probe method in the sample heating mode, with a magnetic field H applied perpendicularly to the current direction. The samples were cooled in the Earth magnetic field. Figures 1 and 2 show the $\rho(T)$ curves of the composites measured at a constant value of the probing transport current (indicated in the legends to
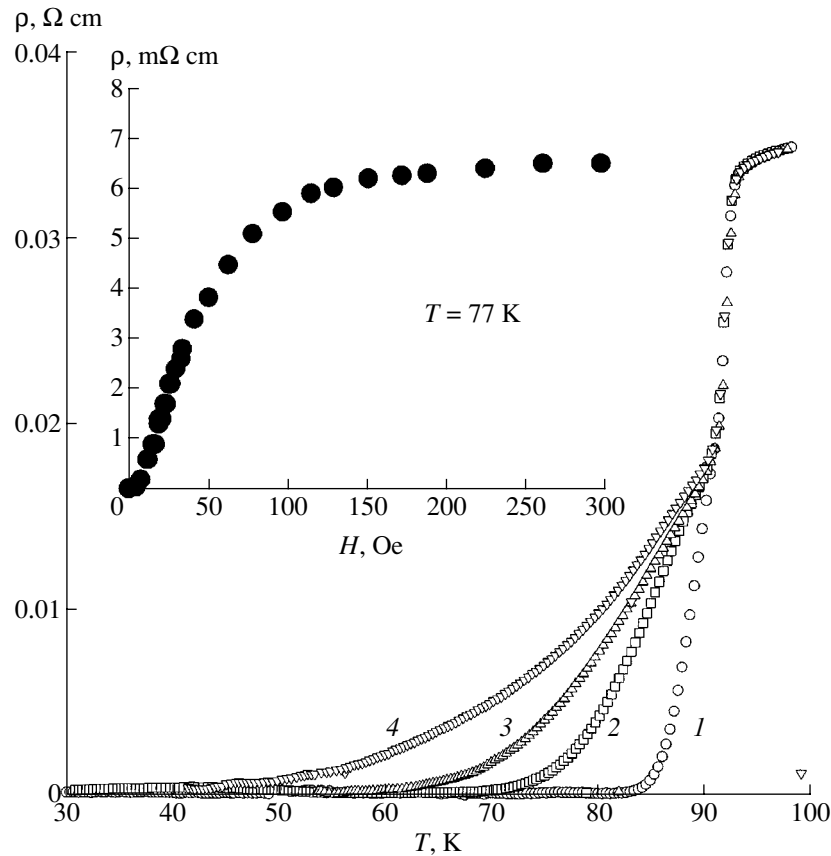
---

[1] We selected the yttrium ceramics with lutetium because this base composition was employed for the preparation of HTSC- based composites in [10–12]. The character of the experimental data is generally the same for pure $YBa_2Cu_3O_7$ based composites.

Fig. 1. Temperature dependences of the resistivity ρ of a 85 vol % YBCO + 15 vol % BaPbO$_3$ composite measured at various values of the applied magnetic field strength $H = 0$ (*1*), 38 (*2*), 79 (*3*), and 270 Oe (*4*) using a probing current density of 50 mA/cm^2. The inset gives the plot of ρ versus H at $T = 77$ K.

figures) and variable magnetic field. The jump in ρ at $T = 93.5$ K corresponds to a transition to the supercon-ducting state in HTSC grains. This temperature coin-cides with T_c of the composites and the initial YBCO determined from the results of magnetic measurements. The relative magnitude of the resistivity jump depends neither on the transport current (as established in [10, 11]) nor on the applied magnetic field (see Figs. 1, 2) and varies only with the bulk ratio of the components. The transition of a composite sample into the state with "zero" resistance (measured with an accuracy of ~10^{-6} Ω cm) is manifested by an extended ρ(T) branch ("tail"). Such behavior of ρ(T) reflects the influence of the grain boundaries, the role of which in the composite is played by the non-HTSC component. This branch of the ρ(T) curve of the composite exhibits a strong dependence on the transport current [10, 11] and the magnetic field strength.

The insets to Figs. 1 and 2 show the plots of ρ(H) measured at $T = 77$ K. Below the magnetic field strength of $H \approx 40$ Oe, the initial (forward) and reverse branches of the ρ(H) dependence coincide. For $H > 40$ Oe, the reverse branch of ρ(H) is lying below the initial curve. When the external field strength is decreased down to

$H \approx 0$ (the Earth's magnetic field was not shielded), the resistance is greater than that before switching the field on (these data are not depicted in the figures). Such a behavior of the ρ(H) is related to the effect of vortex pinning in the HTSC grains. The results of a detailed investigation of ρ(H) at various temperatures will be reported separately. Here, we would like only to emphasize that ρ is highly sensitive to relatively weak magnetic fields (below ~300 Oe) at 77 K. As the H value is increased further, the ρ(H) value at 77 K grows rather weakly, as can be seen from the plots of ρ(H) measured at $H = 1$, 10, and 60 kOe for the sample of 70 vol % YBCO + 30 vol % CuO (Fig. 2). Note that the resistivity transition in HTSC grains also exhibits smearing when the field increases to $H \sim 10–60$ kOe (Fig. 2), the magnitude of this effect in the composite at ~10 K for $H = 60$ kOe being comparable to that in YBCO single crystals [15].

Using the concept of the irreversibility line in HTSCs and the mechanism of thermally activated phase slippage [16] in the Josephson junction, Tin-kham [15] theoretically derived an expression for the resistivity transition width as a function of the applied magnetic field strength: $\Delta T_c(R = 0) = CH^{2/3}$ and indi-cated that this result is applicable both to HTSC single
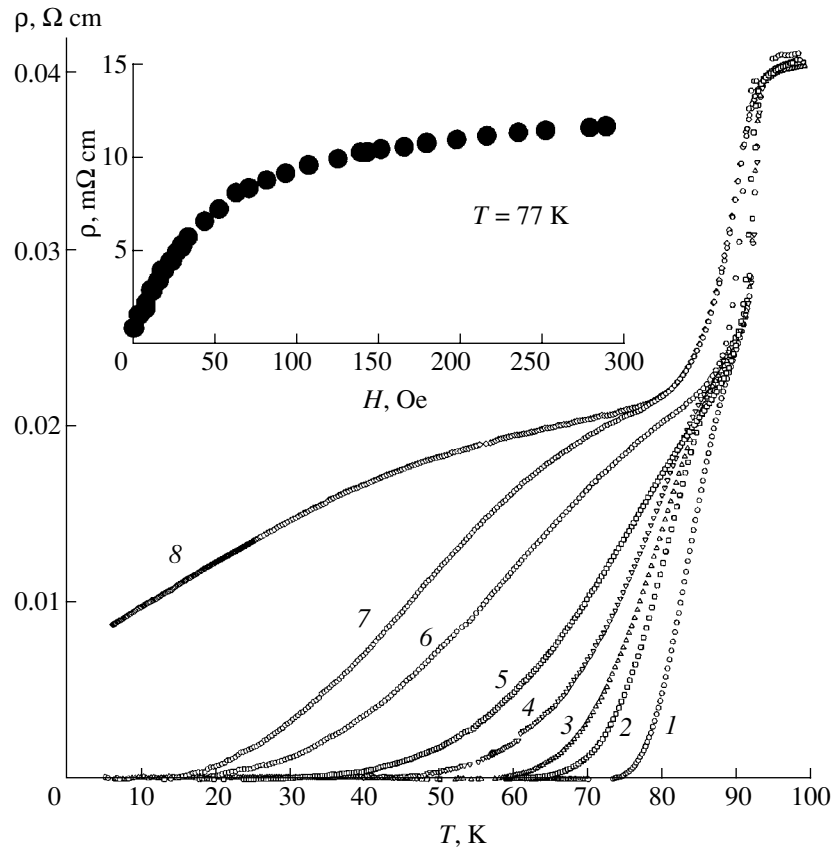
Fig. 2. Temperature dependences of the resistivity ρ of a 70 vol % YBCO + 30 vol % CuO composite measured at various values of the applied magnetic field strength $H = 0$ (*1*), 38 Oe (*2*), 79 Oe (*3*), 183 Oe (*4*), 1 kOe (*5*), 10 kOe (*6*), 60 kOe (*7*) using a probing current density of 50 mA/cm^2 and $H = 60$ kOe (*8*) using a probing current density of 0.5 A/cm^2. The inset gives the plot of ρ versus H at $T = 77$ K.

crystals and to a network of weak contacts of the Josephson type realized in polycrystalline HTSCs. However, the constant factor C in the latter case must be greater than that for the single crystal, which implies that the magnetoresistance effect will be manifested in weak magnetic fields.

Figure 3 shows the plots of $\Delta T_c = T_c(H, R = 0) - T_c(H = 0, R = 0)$ versus $H^{2/3}$. As can be seen, the experimental points fit well to the straight lines constructed in the coordinates of the Tinkham relationship for the field strengths below $H \sim 300$ Oe. The temperatures of zero resistance at $H = 1$, 10, or 60 kOe do not obey this relationship: the experimental curves of $R(H)$ and $R(T, H)$ differ from those calculated by the model proposed in [15]. This can be related to the fact that this mechanism is applicable only in the case of low resistivity and small field strengths. In our composites, it is probably necessary to take into account the distribution of grain boundaries with respect to thickness. It must be noted that the ρ(T) curves for HTSC + CuO composites [10] at various values of the transport current were successfully described within the framework of a mechanism [16] based on the thermoactivated phase slip in the Josephson junction. The behavior of the ρ(T, H)

function in a range of both weak and strong magnetic fields will be considered in a special publication.

Thus, the YBCO + CuO and YBCO + BaPbO$_3$ bulk composites exhibit a greater magnetoresistance effect
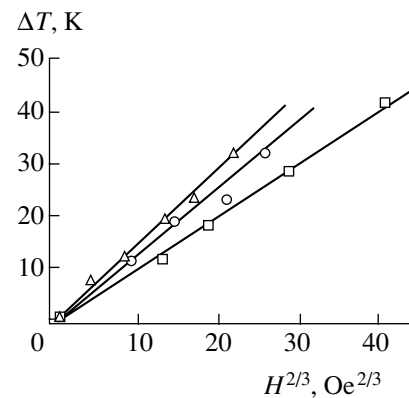

Fig. 3. The plots of $\Delta T_c = T_c(H, R = 0) - T_c(H = 0, R = 0)$ versus $H^{2/3}$ for various HTSC composites: (squares) 85 vol % YBCO + 15 vol % BaPbO$_3$; (triangles) 85 vol % YBCO + 15 vol % CuO; (circles) 70 vol % YBCO + 30 vol % CuO.

than HTSC ceramics in weak magnetic fields (below 300 Oe) at liquid nitrogen temperature. This behavior is of interest for practical applications.

REFERENCES

1. M. A. Dubson, S. T. Herbet, J. J. Calabrese, *et al.*, Phys. Rev. Lett. **60** (11), 1061 (1988).

2. A. C. Wright, K. Zhang, and A. Erbil, Phys. Rev. B **44** (2), 863 (1991).

3. J. Mannhart, P. Chaudhari, D. Dimos, *et al.*, Phys. Rev. Lett. **61** (21), 2476 (1988).

4. A. Barone and G. Paterno, *Physics and Applications of the Josephson Effect* (Wiley, New York, 1982; Mir, Moscow, 1984).

5. J. K. Thomas, J. Koshi, J. Kurian, *et al.*, J. Appl. Phys. **76** (4), 2376 (1994).

6. Chan-Joong Kim, Ki-Baik Kim, Il-Hyun Kuk, and Gye-Won Hong, Physica C (Amsterdam) **255**, 95 (1995).

7. P. E. Kazin, V. V. Poltavets, Y. D. Tretyakov, *et al.*, Physica C (Amsterdam) **280**, 253 (1997).

8. D. Berling, B. Loegel, A. Mehdaoui, *et al.*, Supercond. Sci. Technol. **11**, 1292 (1998).

9. E. Bruneel and S. Hoste, Int. J. Inorg. Mater. **1**, 385 (1999).

10. M. I. Petrov, D. A. Balaev, K. A. Shaĭkhutdinov, and K. S. Aleksandrov, Fiz. Tverd. Tela (St. Petersburg) **41** (6), 969 (1999) [Phys. Solid State **41**, 881 (1999)].

11. M. I. Petrov, D. A. Balaev, S. V. Ospishchev, *et al.*, Phys. Lett. A **237**, 85 (1997).

12. M. I. Petrov, D. A. Balaev, D. M. Gohfeld, *et al.*, Physica C (Amsterdam) **314**, 51 (1999).

13. B. A. Gizhevskiĭ, A. A. Samokhvalov, N. M. Chebotaev, *et al.*, Sverkhprovodimost: Fiz., Khim., Tekh. **4** (4), 827 (1991).

14. D. P. Moiseev, S. K. Uvarova, and M. B. Fenik, Fiz. Tverd. Tela (Leningrad) **23** (8), 2347 (1981) [Sov. Phys. Solid State **23**, 1371 (1981)].

15. M. Tinkham, Phys. Rev. Lett. **61** (14), 1658 (1988).

16. V. Ambegaokar and B. I. Halperin, Phys. Rev. Lett. **22** (25), 1364 (1969).

Translated by P. Pozdeev

The Formation of a Voltage–Luminance Characteristic of Zinc Sulfide Based Electroluminescent Thin-Film Emitters

N. T. Gurin, A. V. Shlyapin, and O. Yu. Sabitov*

Ul'yanovsk State University, Ul'yanovsk, Russia
* e-mail: soy@sv.uven.ru
Received June 28, 2001

Abstract—The formation of a voltage–luminance characteristic of zinc sulfide based electroluminescent thin-film emitters was studied by measuring the instantaneous brightness and current kinetics in an active regime together with the mean field kinetics in the phosphor layer, the charge dependence of the instantaneous brightness, and the current–voltage characteristics. The appearance of a saturation region on the voltage–luminance characteristic is explained in terms of a decrease in the effective phosphor layer and a change in the mechanism of charge carrier scattering. © *2001 MAIK "Nauka/Interperiodica"*.

One of the main features of electroluminescent thin-film (ELTF) emitters is the presence of a saturation portion on their voltage–luminance diagrams presenting the average (apparent) brightness as a function of the amplitude of an alternating-sign excitation voltage [1]. This behavior can be explained by (i) saturation of the voltage across that part of the device structure where excitation of the electroluminescence takes place, (ii) devastation of the source of electrons injected into a string field region of the phosphor, and (iii) increase in the fraction of nonradiative transitions in the phosphor probably accompanied by a decrease in the quantum yield and the luminous efficiency [1].

The purpose of this work was to study the factors determining the ELTF brightness saturation with increasing excitation voltage by measuring the instantaneous kinetics of luminance L and current I_p passing through the phosphor layer in an active regime together with variation of the mean field F_p in the phosphor layer, the charge dependence of the instantaneous brightness, and the current–voltage and some other characteristics.

The experiments were performed on ELTF emitters with an MISIM type structure, where M layers represent a lower transparent 0.2-μm-thick SnO_2-based electrode deposited onto a glass substrate and the upper nontransparent thin-film Al electrode with a thickness of 0.15 μm and a diameter of 1.5 mm, S is the 0.48-μm-thick electroluminescent ZnS:Mn (0.5 wt %) layer, and I are the 0.17-μm-thick insulating ZrO_2–Y_2O_3 (13 wt %) layers. The ZnS:Mn phosphor layer was obtained by thermal evaporation in a quasi-closed volume in vacuum and deposition onto a substrate heated to 250°C, followed by the annealing for 1 h at 250°C. The upper nontransparent metal electrode was also obtained by thermal deposition in vacuum, and thin insulating layers were prepared using the electron-beam deposition technique.

We have experimentally measured the time variation of the instantaneous luminance L and current I_e of ELTF emitters excited with alternating-sign voltage pulses of a triangular shape $V(t)$. The excitation signal was supplied from a G6-34 generator equipped with an additional shaping amplifier and controlled by a G5-89 master generator. The maximum pulse amplitude was $V_m = 160$ V at a nonlinearity coefficient not exceeding 2%. A single excitation cycle represented a train of two-period triangular pulses with a repetition rate of $f = 10$ Hz. In the first half-period, either positive or negative excitation half-wave can be applied to the upper electrode, which is referred to as the +Al and –Al regimes, respectively. The time interval between single excitation cycles was 1 s. The I_e value was measured in a 10 kΩ resistor connected in series with the ELTF emitter structure (the voltage drop on this resistor did not exceed 1 V). The instantaneous luminance was measured with a photoelectron multiplier tube of the FEU-84-3 type.

The patterns of excitation voltage $V(t)$, ELTF emitter current $I_e(t)$ and instantaneous luminance $L(t)$ were recorded with the aid of a two-channel storage oscillograph of the S9-16 type linked via an interface to a personal computer. The system ensured the measurement and storage of 2048 experimental points at a preset discretization period in each channel and 256 levels of the amplitude quantization. The data were mathematically processed and graphically displayed using the application program packages MAPLE V (Release 4, Version 4.00b) and GRAPHER (Version 1.06, 2-D Graphing System).

The time variation of the mean field $F_p(t)$, the current $I_p(t)$, and the charge transferred through the phosphor layer $Q_p(t)$ during the ELTF operation were mea-

sured as described elsewhere [2] for the insulator layer capacitance $C_i = 730$ pF and the phosphor layer capacitance $C_p = 275$ pF determined with the aid of an E7-14 immitance meter for the known ELTF emitter geometry. The average luminance was calculated by the Talbot law for a pulsed radiation source

$$L_e = \frac{2}{T} \int_0^{T/2} L(t)dt, \qquad (1)$$

where $T = 1/f$ is the excitation voltage period.

The total body of experimental data obtained as described above allowed us to consider the formation of the voltage–luminance characteristic in detail and determine the factors responsible for the average brightness L_e saturation with increasing excitation voltage amplitude V_m. The families of various characteristics illustrating a variation of the electroluminescence kinetics with increasing V_m are presented in Fig. 1. As can be seen from these data, one ("fast") region of the $L(t)$ buildup [2, 3] to the upper point *1* is observed for the excitation voltage amplitude up to $V_m = 120$–125 V (Fig. 1a), under which conditions the $I_p(t)$ and $Q_p(t)$ curves also exhibit a single region of fast increase (Figs. 1b, 1g). All these buildup kinetics are described by exponents with the same time constant and the $L(I_p)$ plot is close to linear (Fig. 1d). Here, the character of the mean field variation kinetics $F_p(t)$ in the phosphor layer (Fig. 1c) closely follows the law of the excitation voltage variation $V(t) = V_m t/t_m$. This fast region corresponds to a weak hysteresis of the current–voltage characteristic $I_p(F_p)$ of the phosphor layer (Fig. 1e) and to a sharp increase in the average luminance L_e on the voltage–luminance characteristic close to $\log L_e \sim V_m$ (Fig. 1h).

When V_m is increased by 5–10 V, the second ("slow") region of increase appears on the $I_p(t)$ curve in which the rate of the current buildup changes sign. The analogous region appears on the $L(t)$, $L(I_p)$, and $L(Q_p)$ curves as well. The $F_p(t)$ plot more significantly deviates from linear. The current–voltage characteristic $I_p(F_p)$ of the phosphor layer exhibits a more pronounced hysteresis, which is explained by the recharge of deep donor and acceptor centers and the corresponding change of the space-charge fields of these centers in the near-anode and near-cathode regions of the phosphor layer [2, 4]. The voltage–luminance characteristic exhibits a transition to the saturation behavior. With further increase in V_m, the "slow" buildup regions are completely manifested in the $L(t)$ and $L(I_p)$ curves. The $F_p(t)$ curve strongly deviates from linear. The current–voltage characteristic $I_p(F_p)$ of the phosphor layer measured at a given frequency f shows the appearance of an S-shaped region and exhibits a considerable hysteresis. The voltage–luminance characteristic $L_e(t)$ reaches saturation (Fig. 1h, curve VIII). Here, the point *1'* corre-

sponds to the onset of a significantly weaker variation of $L(t)$, $I_p(t)$, and $F_p(t)$ for $V_m = 160$ V; point *1"* corresponds to the onset of formation of the S-shaped region on the current–voltage characteristic; and point *2* corresponds to $V(t_m) = V_m$ (Fig. 1f).

The +Al regime is characterized by higher L values and somewhat different $L(t)$ shape as compared to the –Al regime (see Fig. 1a), while the $I_p(t)$ shapes in the two regimes are close, in agreement with [2, 3]. Accordingly, the $L(I_p)$, $L(Q_p)$, and $L(F_p)$ curves (see Figs. 1d, 1e, and 1g), as well as the voltage–luminance characteristic $L_e(t)$ (see Fig. 1h, curve VIII) for the +Al variant, are lying above those for the –Al regime. The total voltage–luminance characteristic over the entire excitation period $V(t)$, obtained by averaging the curves for the two partial regimes +Al and –Al, occupies an intermediate position (Fig. 1h, curve IX).

It should be noted that the shape of $L(I_p)$ in the region between points *1* and *2* significantly depends on the excitation voltage frequency and the application regime (+Al versus –Al). As the frequency increases, both sublinear and superlinear portions may appear, which are related to a change in the relationship between the rates of variation of the luminance $L(t)$ and current $I_p(t)$ in this region and is explained by modification of the current–voltage characteristic of the phosphor layer.

The shapes of the $L(t)$, $I_p(t)$, $L(F_p)$, $I_p(F_p)$, $L(Q_p)$, and $L(I_p)$ curves suggest that the main reason for the appearance of the saturation region on the voltage–luminance characteristic is a change in the charge carrier transfer through the phosphor layer. This change is caused by modification of the electric field distribution in this layer, which results in a decrease in the rate of growth (or even in the absolute value) of the luminance L with increasing current I_p or charge Q_p (see Figs. 1d and 1g). This is indicative, on the one hand, of a decrease in the number $N_1(t)$ of emission centers excited by one electron passing through the phosphor layer [1], since the luminance $L(t)$ is related to $N_1(t)$ and the concentration of excited emission centers $N^*(t)$ by the formula [1, 3]

$$L(t) = \frac{AN_1(t)N^*(t)P_r}{\tau^*}, \qquad (2)$$

where A is a constant, τ^* is the emission center lifetime in the excited sate, P_r is the probability of radiative relaxation of the emission center,

$$N_1(t) = d_p(t)\sigma N, \qquad (3)$$

$d_p(t)$ is the effective thickness of the phosphor layer in which the impact ionization of the emission centers takes place, σ is the impact ionization cross-section, and N is the concentration of the emission centers.

The decrease in $N_1(t)$ is probably explained by a decrease in $d_p(t)$ related to the recharge of deep donor centers formed by the zinc vacancies V_{Zn} at the anode,
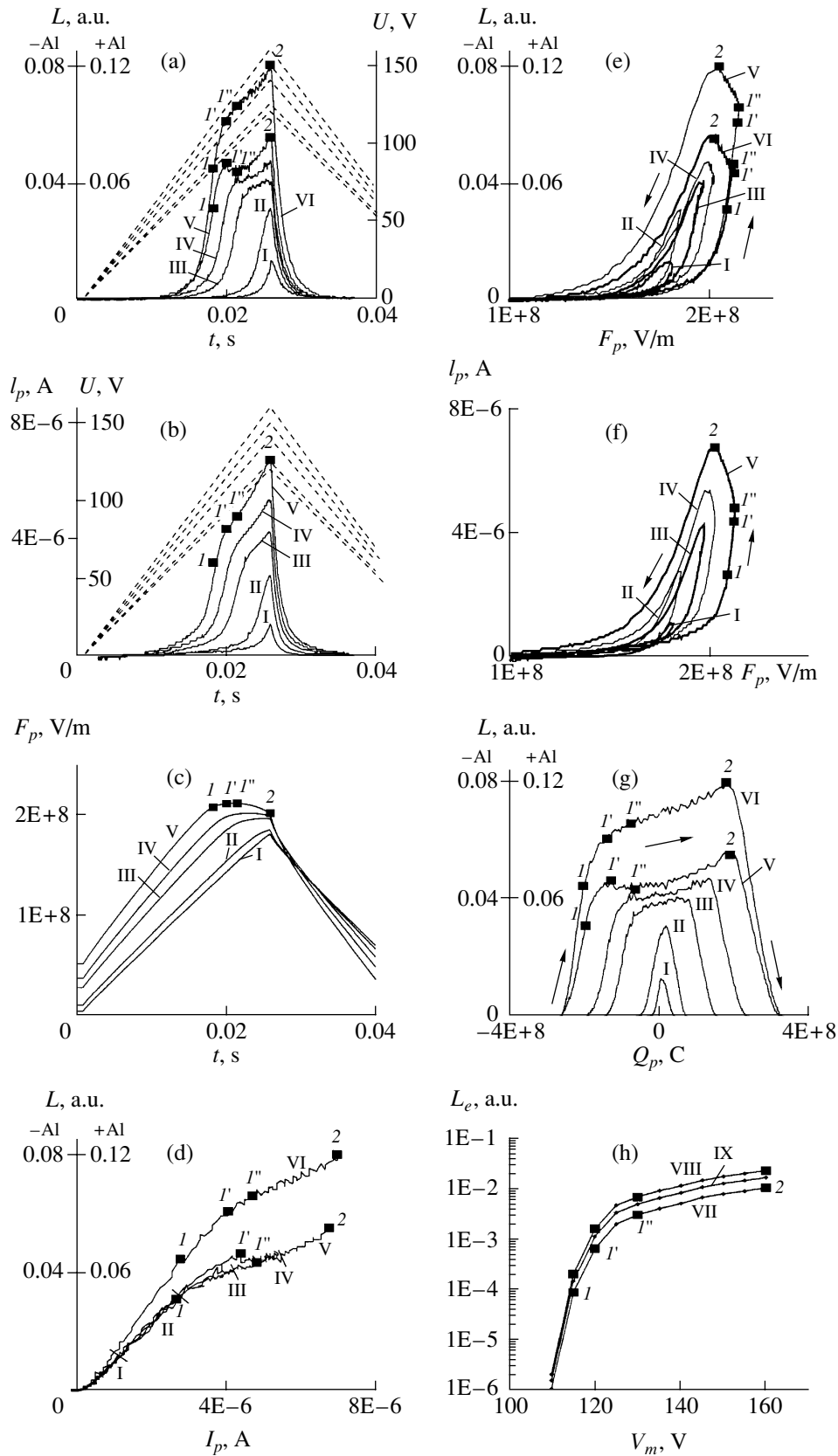
Fig. 1. The formation of a voltage–luminance characteristic of a zinc-based ELTF emitter illustrated by the (a) $L(t)$, (b) $I_p(t)$, (c) $F_p(t)$, (d) $L(I_p)$, (e) $L(F_p)$, (f) $I_p(F_p)$, (g) $L(Q_p)$ and (h) $L_e(V_m)$ curves (V_m, regime): (I) = 120 V, –Al; (II) 125 V, –Al; (III) 140 V, –Al; (IV) 150 V, –Al; (V) 125 V, –Al; (VI) 160 V, +Al; (VII) $L_e(V_m)$, –Al; (VIII) $L_e(V_m)$, +Al; (IX) L_e averaged over the period $V(t)$.

which is accompanied by a decrease in the field strength near the anode and the mean field strength F_p in the phosphor layer [2, 5, 6] and by the appearance of an S-shaped portion in the current–voltage characteristic (Fig. 1f). As a result, the energy of the free electrons at the anode may become insufficient to excite the Mn^{2+} emission centers.

On the other hand, the concentration of the excited emission centers $N*(t)$ is proportional to the probability of excitation per unit time $\alpha(t)$. This probability is determined in the general case by the expression

$$\alpha(t) = \sigma n(t) v(t), \tag{4}$$

where $n(t)$ and $v(t)$ is the concentration and velocity of the free electrons accelerated to the energy of excitation of the emission centers. In the region between points 1 and 2 (see Fig. 1), the system features processes related to the ionization of deep centers. This is accompanied by scattering of the charge carriers (and dissipation of their energy) on these centers, leading to a decrease in the $n(t)$ and $v(t)$ values and, hence, in the probability $\alpha(t)$.

On the whole, the appearance of the saturation region on the voltage–luminance characteristics of ELTF emitters can be related to both mechanisms considered above, since the underlying processes are interrelated.

REFERENCES

1. *Electroluminescent Light Sources*, Ed. by I. K. Vereshchagin (Énergoatomizdat, Moscow, 1990).
2. N. T. Gurin, O. Yu. Sabitov, and A. V. Shlyapin, Zh. Tekh. Fiz. **71** (8), 48 (2001) [Tech. Phys. **46**, 977 (2001)].
3. N. T. Gurin, O. Yu. Sabitov, A. V. Shlyapin, and A. V. Yudenkov, Pis'ma Zh. Tekh. Fiz. **27** (4), 12 (2001) [Tech. Phys. Lett. **27**, 138 (2001)].
4. N. T. Gurin, O. Yu. Sabitov, and A. V. Shlyapin, Zh. Tekh. Fiz. **71** (3), 72 (2001) [Tech. Phys. **46**, 342 (2001)].
5. A. A. Douglas, J. F. Wager, D. C. Morton, *et al.*, J. Appl. Phys. **73** (1), 296 (1993).
6. A. Abu-Dayah, J. F. Wager, and S. Kobayashi, J. Appl. Phys. **74** (9), 5575 (1993).

Translated by P. Pozdeev

On the Scaling Properties of Two Unidirectionally Coupled Period-Doubling Systems in the Presence of Noise

Yu. V. Gulyaev, Yu. V. Kapustina, A. P. Kuznetsov, and S. P. Kuznetsov

Saratov Branch, Institute of Radio Engineering and Electronics,
Russian Academy of Sciences, Saratov, Russia
e-mail: alkuz@sgu.sgu.ru
Received July 2, 2001

Abstract—The results of numerical experiments reveal and illustrate the scaling properties manifested under the noise action at a bicritical point situated at the chaos boundary in a system of two unidirectionally coupled subsystems featuring the period doubling. © *2001 MAIK "Nauka/Interperiodica".*

In recent years, the attention of researchers has been drawn to problems related to the synchronization of systems with complex dynamics. Many situations of this type are of interest from both the theoretical standpoint and in applications involving hidden communication systems, control of chaos, and various phenomena in biological objects [1].

Let us turn to one of the interesting situations involving two partial systems capable of passing to chaos via a cascade of period-doubling bifurcations. We will assume that one partial system acts upon the other, while the reverse action is absent. In this case, a special type of complex dynamics, called bicritical [2], may take place at the chaos threshold. According to this, a bicritical point exists on the plane of control parameters that belongs to the chaos boundary in both subsystems. The vicinity of this point exhibits a universal behavior characterized by several features established based on the renormalization group analysis [3–5]. Such a bicritical behavior was found by numerical calculations for nonautonomous oscillators [6] and the Chua schemes with unidirectional (one-way) coupling [7] and was experimentally observed for a system of two nonautonomous nonlinear oscillatory circuits [2, 8]. In real systems, the phenomena of complex dynamics always take place on the noise background. Therefore, the study of the effect of noise on the bicritical behavior is a task of importance.

Below, we will establish the properties of self-similarity (scaling) for the systems with bicritical dynamics in the presence of noise. This study can be considered as a generalization of the results of Crutchfield *et al.* [9], which cover the effect of noise on the transition to chaos according to Feigenbaum in systems featuring period doubling, to the case of bicritical behavior.

The simplest model exhibiting bicritical behavior is offered by a system of two logistic maps with unidirectional coupling [3–5, 10]:

$$x_{n+1} = 1 - \lambda x_n^2 + \gamma n_n,$$
$$y_{n+1} = 1 - A y_n^2 - B x_n^2 + \varepsilon \xi_n. \quad (1)$$

Here, x and y are the dynamic variables of two subsystems with the control parameters λ and A, respectively; B is the system coupling parameter; γ and ε are the noise amplitudes in the two systems; and η_n and ζ_n are random sequences. According to Kim [5], the bicritical point of system (1) with $B = 0.45$ in the absence of noise has the coordinates $\lambda_C = 1.4011552$ and $A_C = 1.0900943$. The renormalization group analysis indicates that the vicinity of this point possesses a self-similar structure (scaling) with the scaling constants $\delta_F = 4.669201$ and $\delta_B = 2.392724$. In the presence of noise, the degree of its action upon the fractal structure in the plane of parameters and in the phase space must obviously increase at higher resolution levels, which will result in violation of the self-similarity. Crutchfield *et al.* [9] demonstrated that, in the case of a Feigenbaum cascade of the period-doubling bifurcations, the observation of each next doubling level would require the noise level to be reduced by a factor of $\mu_F = 6.619036...$ Let us consider the question as to the factor μ_B by which the level of noise introduced to the second subsystem has to be reduced in order to observe the new level of the fractal structure associated with the bicritical behavior.

Let us rewrite in a generalized form the equations for the systems with unidirectional coupling so as to take into account the noise added only to the second subsystem:

$$x_{n+1} = G(x_n), \quad y_{n+1} = F(x_n, y_n) + \varepsilon V(x_n, y_n)\eta_n. \quad (2)$$

In particular, for model (1), $G(x) = 1 - \lambda x^2$, $U(x) = 1$, $F(x, y) = 1 - A y^2 - B x^2$, and $V(x, y) = 1$. The stochastic

map (2) describes the evolution of the system during one step of discrete time. Applying this operation twice, we obtain the two-step map. Assuming that the noise parameter is small ($\varepsilon < 1$), we may neglect the terms higher than the first order in ε. Substituting variables $x \longrightarrow x/\alpha$ and $y \longrightarrow y/\beta$, we eventually obtain

$$x_{n+2} = \alpha G(G(x_n/\alpha)),$$

$$y_{n+2} = \beta F(G(x_n/\alpha), F(x_n/\alpha, y_n/\beta))$$
$$+ \beta\varepsilon[F_y'(G(x_n/\alpha), F(x_n/\alpha, y_n/\beta))V(x_n/\alpha, y_n/\beta)\eta_n \quad (3)$$
$$+ V(G(x_n/\alpha), F(x_n/\alpha, y_n/\beta))\eta_{n+1}].$$

Assuming now that elements of the random sequence η_n are independent (white noise), we may redefine the random process acting upon the system so as to rewrite Eqs. (3) in a form analogous to Eq. (2):

$$x_{n+2} = G_1(x_n),$$
$$y_{n+2} = F_1(x_n, y_n) + \varepsilon V_1(x_n, y_n)\eta_n. \quad (4)$$

Then, we can multiply repeat the above procedure to obtain a sequence of the functional relationships:

$$G_{k+1} = \alpha G_k(G_k(x/\alpha)),$$
$$F_{k+1}(x, y) = \beta F_k(G_k(x/\alpha), F_k(x/\alpha, y/\beta)),$$

$$V_{k+1}(x, y) \quad (5)$$

$$= |\beta|[(F_{k,y}'(G_k(x/\alpha), F_k(x/\alpha, y/\beta))V_k(x/\alpha, y/\beta))^2$$
$$+ (V_k(G_k(x/\alpha), F_k(x/\alpha, y/\beta)))^2]^{1/2},$$

where the subscript "y" indicates the derivative of F with respect to the second argument.

At the bicritical point, selecting the renormalization constants equal to $\alpha = -2.502907\ldots$ and $\beta = -1.505318\ldots$ makes the functions $G_k(x)$ and $F_k(x, y)$ converging to the limits $g(x)$ and $f(x, y)$ satisfying the following equations [3, 4]:

$$g(x) = \alpha g(g(x/\alpha)),$$
$$f(x, y) = \beta f(g(x/\alpha), f(x/\alpha, y/\beta)). \quad (6)$$

The first equation coincides with the known Feigenbaum–Cvitanovic equation [11]. The results obtained by numerically solving the second equation in (6) were reported elsewhere [3, 4].

The function playing the role of the random perturbation amplitude for $k \longrightarrow \infty$ behaves asymptotically as $V_k(x, y) \cong \sqrt{\Theta^k \Psi(x, y)}$, where $\Theta = \mu_B^2$ is the maxi-

mum eigenvalue and Ψ is the corresponding eigenfunction for the linear functional equation

$$\Theta\Psi(x, y) = \beta^2[(f_y'(g(x/\alpha), f(x/\alpha, y/\beta)))^2\Psi(x/\alpha, y/\beta) \quad (7)$$
$$+ \Psi(g(x/\alpha), f(x/\alpha, y/\beta))].$$

Using known data for the functions g and f [11, 4], we can realize the functional transformation in the right-hand part of Eq. (7) in the form of a computer program. The unknown function $\Psi(x, y)$ is represented by a table of values in the sites of a rectangular lattice on the square $-1 \leq x \leq 1$, $-1 \leq y \leq 1$ with a fourth-order polynomial interpolation between the lattice sites. Setting arbitrary initial conditions for $\Psi(x, y)$, we multiply repeat the functional transformation and normalize the resulting function to unity at the origin, $\Psi^0(x, y) = \Psi(x, y)/\Psi(0, 0)$. The procedure has to be repeated until the $\Psi(0, 0)$ value converges (prior to normalization) to a certain limit. As a result of these calculations, we determined the desired constant $\mu_B = 2.713708\ldots$

Now, let us consider the results of computer calculations. Figure 1 shows a chart of the Lyapunov exponent for the second subsystem on the plane of control parameters (λ, A). The Lyapunov exponent value is coded by the grey color gradation, light and black regions corresponding to the periodic regimes and chaos, respectively. The noise amplitudes are $\gamma = 0$ and $\varepsilon = 0.005$. The fragments presented in the bottom and top rows are magnified by a factor of $\delta_F = 4.669201$ and $\delta_B = 2.392724$ relative to the bicritical point $\lambda_C = 1.4011552$ and $A_C = 1.0900943$. The top row illustrates scaling in the case when the noise amplitude is recalculated using a factor of $\mu_B = 2.713708\ldots$ The bottom row demonstrates the absence of similarity for the small-scale structure on the plane of parameters in a situation when the noise amplitude remains the same on the passage from one pattern to another.

Owing to the universality associated with the renormalization group approach, the properties of scaling with respect to the noise are dependent essentially neither on the distribution law nor on the correlation properties of the acting noise (cf. [12]). Although the illustrations of Fig. 1 were calculated for the simplest binary noise, similar results are obtained upon setting other distribution laws (at least for a limited noise amplitude).

Figure 2 illustrates scaling in the phase space. The initial pattern shows a phase portrait of the attractor of system (2) with $\gamma = 0$ and $\varepsilon = 0.0015$. In the two magnified attractor fragments, the x scale was recalculated with a constant factor of $\alpha_F = -2.502907$ (determined by Feigenbaum for the standard period doubling [11]) and the y scale, with a constant factor of $\beta = -1.505318$ [3, 4]. The noise amplitude was recalculated on the passage from one pattern to another with a factor of $\mu_B = 2.713708$. As can be seen, the scaling is provided with a sufficiently high precision.
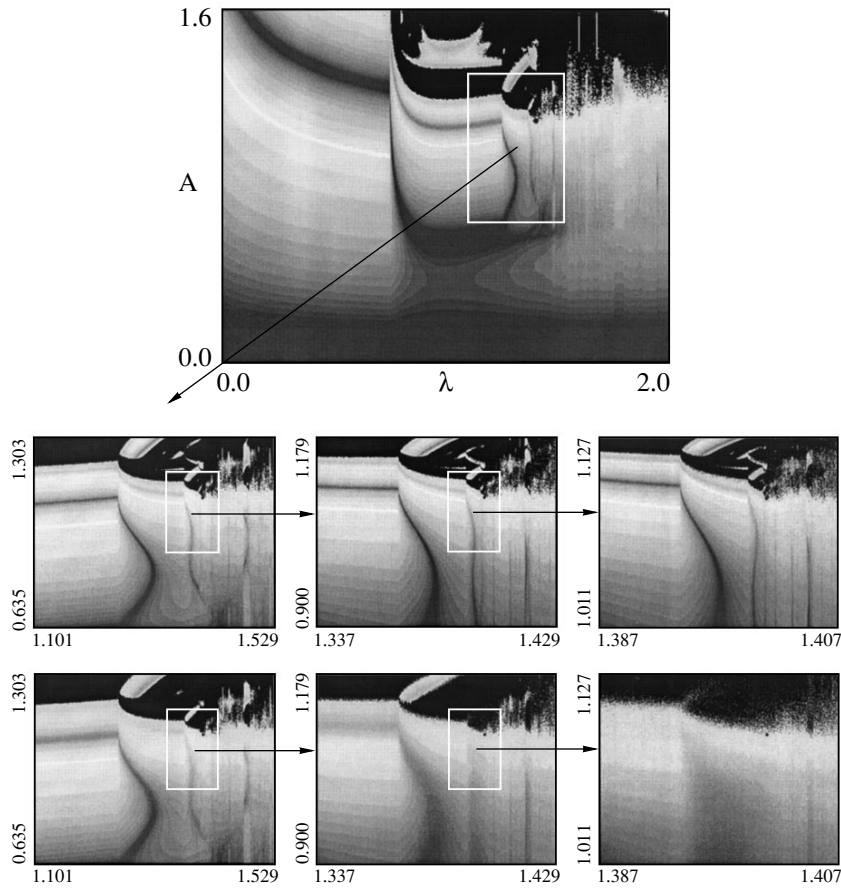
Fig. 1. The pattern of Lyapunov chart and its fragments scaled with and without noise reduction.
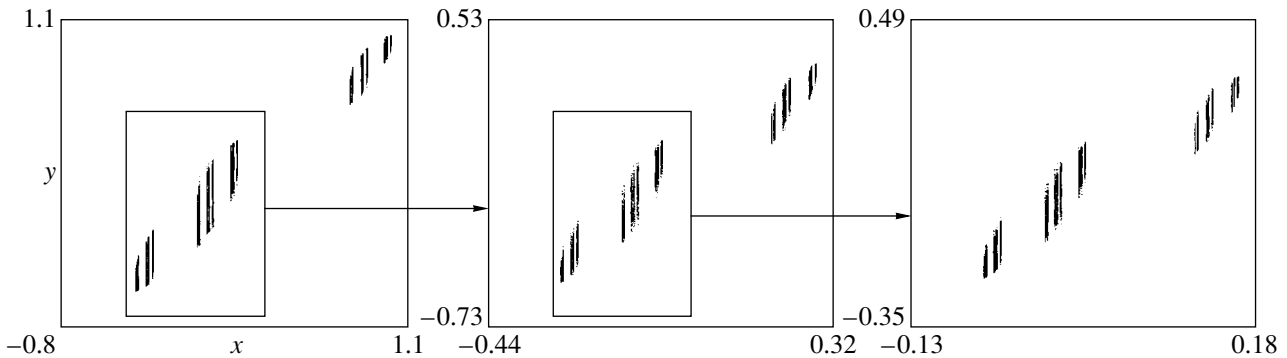

Fig. 2. An example of scaling in the phase portrait.

The above illustrations correspond to the case when no noise is introduced into the first subsystem. However, it follows from the renormalization group analysis and is confirmed by the results of computer calculations that the established scaling properties are valid for the noise present in both subsystems. In this case, the observation of each next level of the fractal structure requires the noise amplitude in the first subsystem to be reduced by the Crutchfield factor μ_F and in the second subsystem, by the factor μ_B. By virtue of the universality principle, the scaling properties with respect to noise in real systems exhibiting bicritical behavior will be the same as in the model system described by Eqs. (1).

REFERENCES

1. A. Pikovsky, M. Rosenblum, and J. Kurths, *Synchronization: A Universal Concept in Nonlinear Sciences* (Cambridge Univ. Press, Cambridge, 2001).

2. B. P. Bezruchko, Yu. V. Gulyaev, S. P. Kuznetsov, *et al.*, Dokl. Akad. Nauk SSSR **287** (3), 619 (1986) [Sov. Phys. Dokl. **31**, 258 (1986)].

3. S. P. Kuznetsov, Izv. Vyssh. Uchebn. Zaved., Radiofiz. **33** (7), 788 (1990).

4. A. P. Kuznetsov, S. P. Kuznetsov, and I. R. Sataev, Int. J. Bifurcation Chaos Appl. Sci. Eng. **1** (4), 839 (1991).

5. S.-Y. Kim, Phys. Rev. E **59** (6), 6585 (1999).

6. S.-Y. Kim and W. Lim, Phys. Rev. E **63** (3), 036223 (2001).

7. A. P. Kuznetsov, S. P. Kuznetsov, I. R. Sataev, *et al.*, Int. J. Bifurcation Chaos Appl. Sci. Eng. **6** (1), 119 (1996).

8. B. P. Bezruchko and O. B. Pudovochkin, Izv. Vyssh. Uchebn. Zaved., Radiofiz. **35** (1), 39 (1992).

9. J. Crutchfield, M. Nauenberg, and J. Rudnich, Phys. Rev. Lett. **46**, 933 (1981).

10. A. P. Kuznetsov, S. P. Kuznetsov, and I. R. Sataev, Int. J. Bifurcation Chaos App. Sci. Eng. **3** (1), 139 (1993).

11. M. J. Feigenbaum, J. Stat. Phys. **21** (6), 669 (1979).

12. D. Fiel, J. Phys. A **20**, 3209 (1987).

Translated by P. Pozdeev

Broken-Gap Heterojunction
in the p-GaSb–n-InAs$_{1-x}$Sb$_x$ ($0 \leq x \leq 0.18$) System

S. S. Kizhaev[a,*], S. S. Molchanov[a], N. V. Zotova[a], E. A. Grebenshchikova[a],

Yu. P. Yakovlev[a], E. Hulicius[b,], T. Šimeček[b], K. Melichar[b], and J. Pangrác[b]**

[a] *Ioffe Physicotechnical Institute, Russian Academy of Sciences, St. Petersburg, 194021 Russia*
[b] *Institute of Physics, Academy of Sciences of the Czech Republic, 18221 Prague 8, Czech Republic*
*e-mail: * serguie@mail.ru; ** hulicius@fzu.cz*
Received June 28, 2001

Abstract—Epitaxial InAs$_{1-x}$Sb$_x$ layers with the Sb content $0 \leq x \leq 0.18$ were grown by metalorganic vapor phase epitaxy (MOVPE) on p-GaSb and n-InAs substrates. The photoluminescence (PL) spectra of the heterostructures were measured at $T = 77$ K. The experimental PL data were used to study variation of the bandgap as a function of the InAsSb solid solution composition. The energy difference between the GaSb valence band top and the InAs$_{0.82}$Sb$_{0.18}$ conduction band bottom was calculated. It was established that GaSb/InAs$_{1-x}$Sb$_x$ with $0 \leq x \leq 0.18$ represents a broken-gap heterojunction of type II. © 2001 MAIK "Nauka/Interperiodica".

In recent years, special properties of the broken-gap heterojunction of type II based on InAs and GaSb solid solutions have been widely used in various optoelectronic devices. In particular, the phenomenon of interfacial electroluminescence was employed in tunneling-injection light-emitting diodes (LEDs) and lasers [1]. The luminescent, photoelectric, and magnetotransport properties of the lattice matched system In$_x$Ga$_{1-x}$As$_y$Sb$_{1-y}$/GaSb obtained by liquid phase epitaxy (LPE) are studied in sufficient detail [2, 3]. Recently, Voronina *et al.* [4] studied the magnetotransport in the lattice matched system In$_x$Ga$_{1-x}$As$_y$Sb$_{1-y}$/GaSb with various In content in the solid solution ($x = 0.85–0.95$) grown by LPE.

The system InAs$_{1-x}$Sb$_x$/GaSb is also of interest, representing the heterojunction of type II with a bandgap that can be either broken or staggered, depending on the Sb content in the solid solution. In the case of a broken-gap p–n junction, the system is always characterized by an ohmic behavior (due to a strong flow of carriers across the heteroboundary under applied external bias), while the directly biased staggered junction is

rectifying with recombination on both sides of the heterojunction [2]. However, the system InAs$_{1-x}$Sb$_x$/GaSb is still insufficiently studied, especially in the case of heterostructures obtained by metalorganic vapor phase epitaxy (MOVPE) technique. The purpose of our study was to determine the type of the p–n junction formed in the MOVPE p-GaSb–n-InAs$_{1-x}$Sb$_x$ system with a Sb content in the solid solution within $0 \leq x \leq 0.18$.

We have studied the epitaxial InAsSb layers grown by MOVPE in a horizontal reactor of the AIXTRON 200 type. The p-GaSb substrates were doped with Ge to a level of $\sim 3 \times 10^{18}$ cm^{-3}. Before the epitaxial growth stage, the substrates were rinsed in acetone and etched in a chromium oxide–based etching solution. The sources of indium, antimony, and arsenic were trimethylindium (TMIn, +16°C), tertiary butylarsine (TBAsH$_2$, +5°C), and triethylantimonide (TESb, +16°C). The growth was conducted in an atmosphere of hydrogen flowing at a total rate of 4 l/min and a reactor pressure of 150 Torr. The flow rates and the growth temperatures for each sample are presented in the table. Several InAsSb layers were obtained on InAs substrates ($n \sim 2 \times 10^{16}$ cm^{-3}) in

InSb/InAs$_{1-x}$Sb$_x$ MOVPE layer growth conditions and PL peak parameters

Sample no.	Growth temperature, °C	H$_2$ flow rate (cm^3/min) through			Sb content, % (solid phase)	$h\nu_m$, meV	$\Delta h\nu_{1/2}$, meV
		TMIn	TESb	TBAsH$_2$			
859	500	292	113	25	18	325	47
860	600	292	113	25	4.2	390	35
861	600	292	180	23	7.1	351	33
862	600	292	248	21	9	345	33

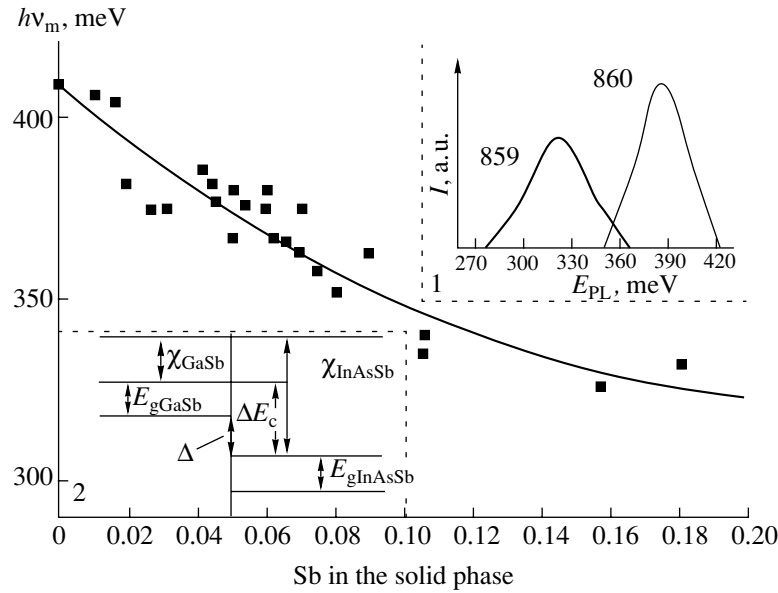**Fig. 1.** The plot of PL peak ($T = 77$ K) position versus Sb content (x) in the InAs$_{1-x}$Sb$_x$ solid solutions. Inset 1 shows the PL spectra of samples Nos. 859 and 860 (see table). Inset 2 shows a schematic energy band diagram of the GaSb/InAs$_{0.82}$Sb$_{0.18}$ system before bringing the two semiconductors in contact.

an epitaxial growth system operating at atmospheric pressure. The growth conditions for these samples will be reported in a special publication.

The elemental composition of the InAsSb solid solution was determined using a Camebax electron-probe microanalyzer (Cameca, France). Using the values of lattice constants for the binary compounds GaSb (6.0959 Å), InAs (6.0584 Å), and InSb (6.4794 Å) [5], we calculated the composition of a solid solution lattice matched with the GaSb substrate: Sb ~ 9%.

The epitaxial heterostructures were characterized by photoluminescence (PL) spectra measured at 77 K with a GaAs diode laser ($\lambda = 0.8$ μm) operating in a pulsed mode at a pulse power of $P = 10$ W, pulse duration $\tau = 5$ μs, and repetition frequency 500 Hz. The current–voltage (I–V) characteristics were studied using mesa diode samples with a diameter of 300 μm prepared by a standard photolithographic method. An areal ohmic contact was created on the n-InAsSb layer side. The point contact on the substrate side had a diameter of 100 μm. The ohmic contacts were obtained by depositing gold with tellurium (on the n-type layer) or gold with zinc (on the p-type layer).

Now, let us consider the experimental results. Figure 1 shows a plot of the PL peak energy position $h\nu_{\mathrm{m}}$ versus Sb content x in the InAsSb solid solution; inset 1 shows the PL spectra of samples 859 ($x = 18\%$) and 860 ($x = 4.2\%$) measured at 77 K. For samples 861 and 862 (characterized by a minimum lattice mismatch with the GaSb substrate), the PL linewidth at half maximum ($h\nu_{1/2}$) was 33 meV. As the mismatch increases, the PL linewidth grows (see table).

Assuming that PL is due to the direct transitions between conduction and valence bands, the bandgap width E_{g} of a nondegenerate solid solution can be calculated by the formula

$$E_{\mathrm{g}} = h\nu - 1/2kT. \tag{1}$$

For $T = 77$ K, $E_{\mathrm{g}} \cong h\nu$ and, hence, approximating the plot of $h\nu_{\mathrm{m}}$ versus x by a quadratic polynomial and using the temperature coefficient of E_{g} in InAs $\Delta E_{\mathrm{g}}/\Delta T = 2.8 \times 10^{-4}$ eV/K, we obtain the following expression for the room-temperature bandgap of the InAs$_{1-x}$Sb$_x$ solid solution ($x = 0$–0.18):

$$E_{\mathrm{g}} \text{ [eV]} = 0.36 - 0.77x + 1.72x^2. \tag{2}$$

This expression is in good agreement with the model proposed by Adachi [5] for calculating the bandgaps of solid solutions. In particular, the room-temperature bandgap of the InAs$_{1-x}$Sb$_x$ solid solution is calculated in this model by the formula

$$E_{\mathrm{gInAsSb}} = xE_{\mathrm{gInSb}} + (1-x)E_{\mathrm{gInAs}} + Cx(x-1), \tag{3}$$

where $E_{\mathrm{gInSb}} = 0.18$ eV and $E_{\mathrm{gInAs}} = 0.36$ eV are the bandgaps in InSb and InAs, respectively, and $C = 0.58$ eV is the empirical bowing parameter. In order to determine the heterojunction type (alignment), it is necessary to calculate the energy band diagram of the system. Consider a schematic diagram of the GaSb/InAs$_{0.82}$Sb$_{0.18}$ system before bringing the two semiconductors in contact (Fig. 1, inset 2). The energy difference between the conduction band bottoms ΔE_{c} at the boundary is calculated using the electron affinity values of the semiconductors: $\Delta E_{\mathrm{c}} = \chi_1 - \chi_2$. For GaSb at $T = 300$ K, $\chi =$
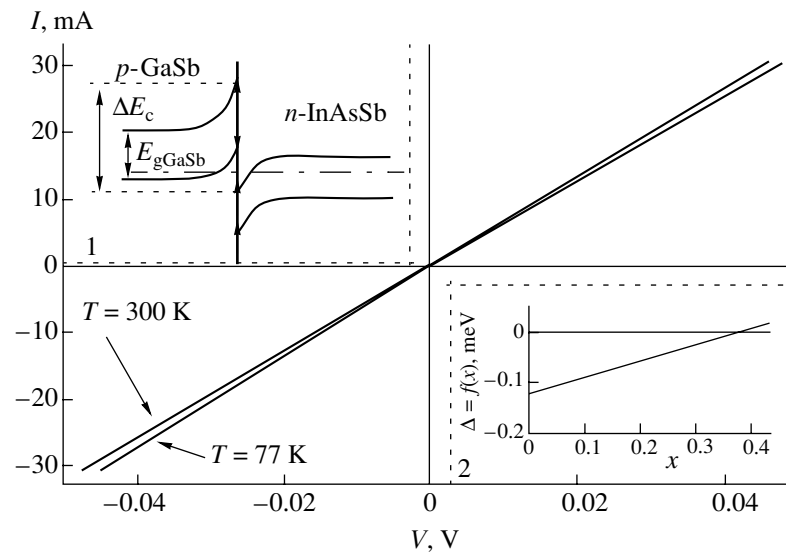
Fig. 2. The current–voltage characteristics of mesa diodes based on the *p*-GaSb/*n*-InAsSb heterostructure measured at $T = 77$ and 300 K. Inset 1 shows a schematic energy band diagram of the *p*-GaSb–*n*-InAsSb broken-gap heterojunction in the state of thermodynamic equilibrium. Inset 2 shows a plot of the energy difference $\Delta = f(x)$.

4.06 eV [6]. The electron affinity of an $InAs_{1-x}Sb_x$ solid solution can be calculated by the formula

$$\chi_{InAsSb} = x\chi_{InSb} + (1-x)\chi_{InAs}, \qquad (4)$$

where $\chi_{InSb} = 4.6$ eV and $\chi_{InAs} = 4.9$ eV are the electron affinities of InSb and InAs, respectively, at $T = 300$ K [6]. For an InAsSb solid solution containing 18% Sb, the electron affinity calculated by this formula is $\chi = 4.84$ eV and the corresponding energy difference is

$$\Delta E_c = \chi_{GaSb} - \chi_{InAs_{0.82}Sb_{0.18}} = -0.78 \text{ eV}. \qquad (5)$$

Since the bandgap of GaSb ($E_{gGaSb} = 0.72$ eV [5]) is smaller than the ΔE_c value, the energy difference between the GaSb valence band top and the $InAs_{0.82}Sb_{0.18}$ conduction band bottom is

$$\Delta = \Delta E_c + E_{gGaSb} = -0.06 \text{ eV}. \qquad (6)$$

This result indicates that the given system represents a broken-gap heterojunction of type II.

Figure 2 shows the current–voltage characteristics of a *p*-GaSb/*n*-$InAs_{0.82}Sb_{0.18}$ heterostructure diode. As can be seen, the plot is linear both at room temperature and at $T = 77$ K. This behavior is indicative of an ohmic character of the contact between the two semiconductors GaSb/$InAs_{1-x}Sb_x$ for $0 \le x \le 0.18$. If the heterojunction were staggered, the diode current–voltage characteristic would be different. The absence of nonlinearities on the ohmic characteristic of the *p–n* structure at small bias voltages at temperatures as low as 77 K is evidence of a low density of states at the heterojunction. The energy band diagram of the broken-gap *p*-GaSb–*n*-$InAs_{1-x}Sb_x$ heterojunction in the state of thermodynamic equilibrium is depicted in inset 1 on Fig. 2; inset 2 shows the plot of $\Delta = f(x)$.

Thus, we have grown by MOVPE and characterized by PL measurements at $T = 77$ K the $InAs_{1-x}Sb_x$ layers with the Sb content $0 \le x \le 0.18$ on *p*-GaSb and *n*-InSb substrates. Using the experimental PL data, the E_g value was studied as a function of the composition of the InAsSb solid solution. The energy difference Δ between the GaSb valence band top and the $InAs_{0.82}Sb_{0.18}$ conduction band bottom was calculated for $x = 0.18$. The ohmic character of the experimental current–voltage characteristics confirms the results of the calculation and shows direct evidence of the type II alignment of this broken-gap heterojunction.

REFERENCES

1. M. P. Mikhailova, K. D. Moiseev, Y. A. Berezovets, *et al.*, IEE Proc.: Optoelectron. **145** (5), 268 (1998).
2. M. P. Mikhailova and A. N. Titkov, Semicond. Sci. Technol. **9**, 1279 (1994).
3. K. D. Moiseev, M. P. Mikhailova, N. D. Stoyanov, *et al.*, J. Appl. Phys. **86** (11), 6264 (1999).
4. T. I. Voronina, B. E. Zhurtanov, T. S. Lagunova, *et al.*, Fiz. Tekh. Poluprovodn. (St. Petersburg) **35** (3), 345 (2001) [Semiconductors **35**, 331 (2001)].
5. S. Adachi, J. Appl. Phys. **61** (10), 4869 (1987).
6. *Handbook of Physical Quantities*, Ed. by I. S. Grigoriev and E. Z. Meilikhov (Énergoizdat, Moscow, 1991; CRC Press, Boca Raton, 1997).

Translated by P. Pozdeev

The Influence of Vacuum Conditions on the Microwave Generation in a Vircator

V. D. Selemir, A. E. Dubinov*, B. G. Ptitsyn, A. A. Evseenko, V. A. Letyagin, R. K. Nurgaliev, V. G. Suvorov, and A. V. Sudovtsov

Institute of Experimental Physics, Russian Federal Nuclear Center, Sarov, Russia
* e-mail: dubinov@ntc.vniief.ru
Received July 2, 2001

Abstract—The effect of residual gases on the lifetime of a virtual cathode (VC) was studied. Dependence of the output pulse energy of a high-power vircator on the vacuum conditions was studied. It is demonstrated that a rough vacuum of 5×10^{-4} Torr achieved with a mechanical pump is sufficient for a vircator operation without significant loss of the output radiation energy. The experimental data agree with a model of the mechanism of VC degradation as a result of the gas ionization. © *2001 MAIK "Nauka/Interperiodica".*

At present, microwave generators with virtual cathodes (VCs)—vircators—are among the most popular devices employed in superhigh-power relativistic microwave electronics. The principle of the vircator operation consists in creating a VC drifting in a vacuum tube, the oscillations of which account for the microwave generation. A review of the vircator physics and technology can be found in [1].

As a rule, the vacuum cavities of a vircator are evacuated to a pressure from 10^{-4} to 10^{-5} Torr, which is usually achieved with the aid of a two-stage pumping system. The first-stage mechanical pump reduces the pressure to a level of 10^{-3} Torr, and then an oil-diffusion pump decreases the residual gas pressure to a preset level. Apparently, an important technical question as to what residual pressure is actually necessary for vircator operation in the optimum regime to be solved for each particular oscillator type.

The purpose of this experimental study was to determine the influence of vacuum conditions in the working volume of a high-power vircator on the output radiation characteristics.

Before passing to the description of our experiments, let us consider some known facts that might allow us to predict the results. According to the previously developed theory [2], injection of an overthreshold electron beam into the drift tube of a vircator containing residual gases at a low pressure leads to the formation of a VC, near which an intense gas ionization takes place (in the vicinity of the VC, the electron velocity is small and their density is many times that at the injection plane). Saturated with the gas ions, the VC exhibits charge neutralization and shifts in the direction of transit electrons. The gas ionization continuing in the new position maintains the VC drift. Thus, the VC performs directed motion and a part of the residual gas ions can be trapped in an acceleration regime. When the

moving VC with trapped ions reaches the opposite end of the drift tube (collector), the microwave generation process ceases.

Thus, the microwave generation period of the vircator is determined by the VC lifetime, which depends on the gas ionization rate and the VC pathlength to collector. If the VC lifetime exceeds the vircator high-voltage power supply pulse duration, the gas ionization process must not affect the output radiation characteristics of the microwave oscillator.

Volosov and Chirikov [3] studied a vircator with a nonrelativistic electron beam and showed that the VC lifetime τ can be described by a simple formula

$$\tau = \frac{\alpha}{p}\left(1 - \frac{I_{\lim}}{I}\right), \qquad (1)$$

where p is the gas pressure, I is the injected beam current, $I_{\lim}$ is the limiting (threshold) current for a given drift tube geometry, and α is a constant depending on the gas composition (e.g., for air $\alpha \sim 2 \times 10^{-10}$ Torr). Malyshev and Rybas [4] specified the above relationship by taking into account nonuniformity of the charge neutralization process along the drift tube, which decreased the τ value by a factor of about 1.5. It should be noted that the results obtained in [3, 4] provided the scientific background for using the finite VC lifetime τ as a probe for ultrahigh vacuum. The τ value can be measured by determining the time instant of the transit current jump or the microwave radiation ceasing. For example, Lloyd [5] proposed a gas pressure sensor for a range from $p = 5 \times 10^{-5}$ to 4×10^{-9} Torr based on an electron beam with VC and determined the α values for hydrogen, nitrogen, and argon.

Now, let us consider the influence of the residual gas pressure on the microwave generation characteristics of a high-power relativistic vircator. The vircator studied
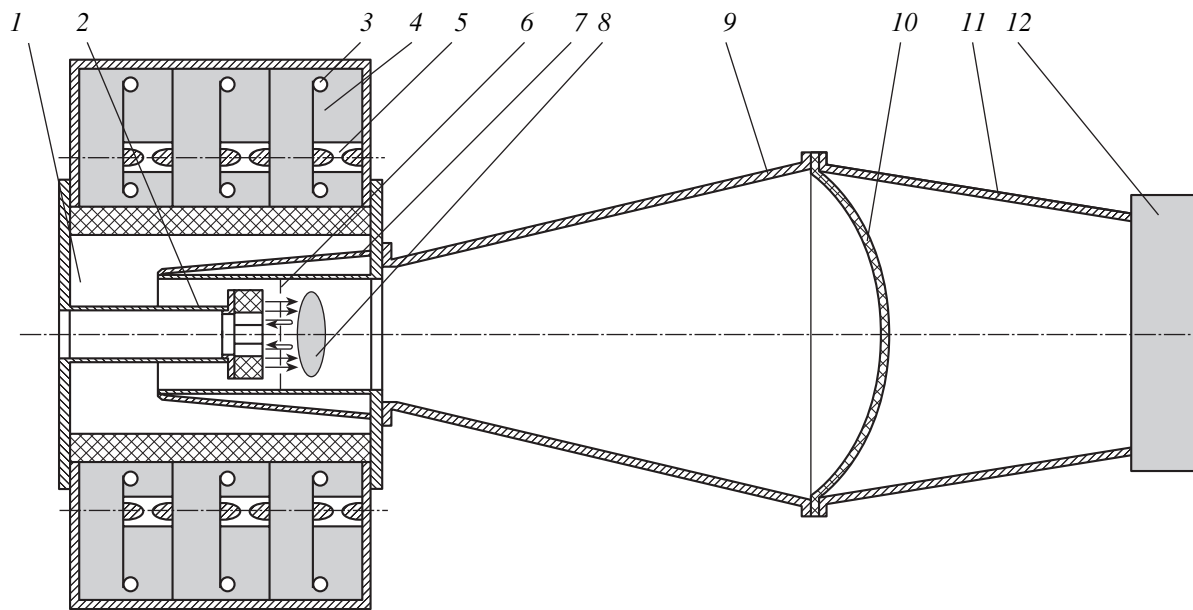
Fig. 1. A schematic diagram of the vircator system based on an iron-free induction linac: (*1*) linac vacuum chamber; (*2*) vircator cathode; (*3*) high-voltage electrode of the inductor unit; (*4*) deionized water; (*5*) gas-filled controlled discharge gap; (*6*) anode grid; (*7*) vircator anode; (*8*) virtual cathode (VC); (*9*) output horn antenna; (*10*) output window; (*11*) matching waveguide; (*12*) input window of the microwave calorimeter (MWC).

in our experiments was based on an iron-free linear induction electron accelerator (linac) implementing radial water-filled KORVET lines (previously employed as an injector of the LIU-10 plant [6]). A schematic diagram of the linac–vircator system is presented in Fig. 1. The vircator contained coaxial cathode (inner) and anode (outer) electrodes. The cathode system comprised a cathode holder, representing a thin-wall (0.2 mm thick) stainless-steel tube, and a steel substrate welded on the side facing anode. The substrate held graphite cylindrical elements (20 mm in diameter, 40 mm long) fastened with screws, which served as emitters. The substrate could accommodate 8, 10, or 12 closely spaced emitter elements forming the cathode assembly with an outer diameter of 72, 92, or 112 mm, respectively.

The anode electrode comprised a hollow cylinder with a diameter of 160 mm and a length of 380 mm. A metal ring inserted inside the cylinder carried a grid anode (made of a 0.3-mm nichrome wire and attached by electric welding) with 3-mm square cells. The ring with the grid anode could be moved along the vircator axis so as to change the cathode–anode spacing of the vircator. In a given setup design, this interelectrode spacing could be varied from 8 to 13 mm. The anode electrode terminated with a cone-shaped horn antenna with an opening angle of 10°. The output organic-glass window, separating the vacuum vircator chamber from the external air space, had a diameter of 700 mm. The amplitude of the voltage developed in the vircator diode at a maximum inductor unit charging was 1 MV. The diode current amplitude at this voltage reached 35 kA

for a pulse duration of 40 ns. According to estimates, this is about two times the limiting beam current in the anode region behind the grid (15–20 kA). By varying the cathode–anode (grid) spacing, cathode diameter, and cathode holder length, the vircator geometry was optimized so as to generate a maximum output power reaching 520 MW (as measured by the hot-carrier semiconductor detectors [7]) at a wavelength of ~3 cm.

The output radiation pulse energy was measured with a microwave calorimeter (MWC) designed and constructed at the Institute of Applied Physics of the Russian Academy of Sciences. The MWC comprises a vacuum-tight cylindrical case with flanges, an input waveguide, energy-absorbing section, thermal decoupling (insulation) unit, and lid. The energy-absorbing section pressed between the input waveguide and thermal insulator represents a polyethylene disk with mount holes keeping 236 thermocouple units each comprising an absorbing element and a thermal transducer. The output voltage of the serially connected thermocouple units is fed via an SR75 connector to a Hewlett-Packard Model 34790A microvoltmeter. The MWC is intended for measuring the microwave radiation energy of a single pulse or pulse trains in super-large-sized waveguide lines. The measurable energy interval extends from 0.1 to 100 J in a frequency range from 6 to 11 GHz. The MWC has a sensitivity of 34 ± 3 μV/J at a voltage standing-wave ratio (SWR) not exceeding 1.65 and a response time of 55–60 s. The output horn antenna of the vircator was matched to the MWC input window of different diameter by a 1.4-m-long truncated-cone waveguide made of a
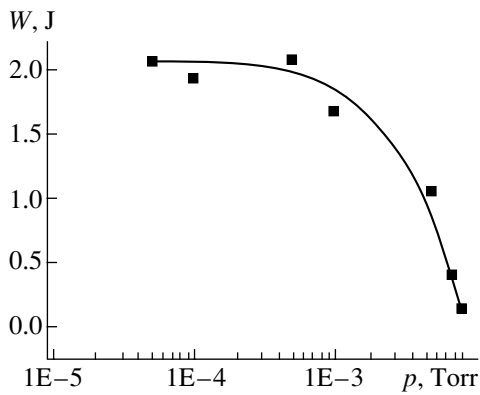
Fig. 2. A plot of the output microwave radiation pulse energy W versus residual air pressure p in the vircator chamber.

1-mm-thick sheet metal. The MWC input window diameter is 550 mm.

The total microwave radiation pulse energy of the vircator operating at a maximum output power was ~2 J. Dependence of the output microwave pulse energy on the residual gas pressure in the vircator volume was measured as follows. When the pumping stage was switched off, the air was allowed to leak inside the vircator volume to a certain residual pressure monitored with an ionization gauge of the PMI-10 type and a thermocouple gauge of the VIT-3 type. Several vircator pulses generated at this pressure were measured with the MWC and the results were averaged. The results of these measurements are presented in Fig. 2. As can be seen from these data, the energy of the output microwave pulses virtually does not change for a residual air pressure in the vircator chamber not exceeding 5×10^{-4} Torr. From this, we may conclude that no oil-diffusion pump is necessary for the experimental vircator operation and a vacuum level provided by the roughing (mechanical) pump stage is sufficient. This circumstance significantly reduces the experimental time consumption. However, it must be noted that our conclusion may be inapplicable to vircators operating at a longer current pulse duration.

Another important circumstance to be pointed out is that increasing the pressure in the vircator volume may give rise to ion oscillations at a frequency on the order of a few tens of megahertz [8], which may influence the output radiation characteristics of long-pulse vircators. In our case, with the vircator pulse duration being significantly shorter than the possible ion oscillation period, this effect can be ignored. In addition, estimates obtained using formula (1) for a pressure of 5×10^{-4} Torr indicate that the VC lifetime is about ~40 ns and becomes shorter than the current pulse duration (40 ns) at a greater pressure. These estimates agree with the model notions of the mechanism of VC degradation as a result of the residual gas ionization.

REFERENCES

1. A. E. Dubinov and V. D. Selemir, Zarubezhn. Radioélektron., No. 4, 54 (1995).

2. K. V. Khodataev and E. V. Shakhanova, Preprint No. 79, IPM AN SSSR (Moscow, 1986).

3. V. I. Volosov and B. V. Chirikov, Zh. Tekh. Fiz. **27** (2), 2624 (1957) [Sov. Phys. Tech. Phys. **2**, 2437 (1957)].

4. I. F. Malyshev and K. P. Rybas, Élektrofiz. Appar., No. 2, 179 (1964).

5. O. Lloyd, Br. J. Appl. Phys. **17** (3), 357 (1966).

6. A. I. Pavlovskiĭ, V. S. Bosamykin, V. A. Savchenko, *et al.*, Dokl. Akad. Nauk SSSR **250** (5), 1117 (1980) [Sov. Phys. Dokl. **25**, 120 (1980)].

7. M. D. Rayzer and L. É. Tsopp, Radiotekh. Élektron. (Moscow) **20** (8), 1691 (1975).

8. V. A. Balakirev, A. M. Gorban', I. I. Magda, *et al.*, Fiz. Plazmy **23** (4), 350 (1997) [Plasma Phys. Rep. **23**, 323 (1997)].

Translated by P. Pozdeev

Exothermal and Endothermal Effects in Porous Titanium–Nickel Alloys

V. N. Khodorenko, V. É. Gyunter*, A. N. Monogenov, and Yu. F. Yasenchuk

Institute of Medical Materials and Shape-Memory Implants, Siberian Physicotechnical Institute,
Tomsk State University, Tomsk, Russia
* e-mail: guntsme@elefot.tsu.ru
Received June 25, 2001

Abstract—It was found that the phase transitions in porous titanium–nickel alloys are characterized by an extended temperature interval of heat release (on cooling) and heat absorption (on heating). The total heat released and absorbed in porous titanium–nickel alloys markedly exceeds that in the analogous cast alloys. The maximum exothermal and endothermal effects are manifested in the alloys with fine pores. The extended temperature interval and increased amount of released and absorbed heat during the phase transitions in porous TiNi alloys, as compared to the analogous cast alloys, is determined by the degree of porosity, the character of inhomogeneity of the porous alloy structure, and the width of the martensite transformation interval. © 2001 MAIK "Nauka/Interperiodica".

The wide use of biocompatible titanium–nickel alloys in medicine requires a wide and thorough investigation of the mechanical properties and structure characteristics of these materials. Previously [1, 2], we reported that the porous titanium–nickel alloys are characterized by a broad hysteresis and extended temperature intervals of the phase transitions. Possessing high elastic properties, these porous alloys behave much like permeable tissues of the organism [3] and are capable of functioning under real living organism conditions. In addition, a porous titanium–nickel alloy is an effective thermostat that changes its internal energy in response to the external temperature variation, thus maintaining the system temperature. In the region of phase transitions, the permeable porous titanium–nickel alloys behave as a highly inertial system, exhibiting delayed reaction to sharp external temperature changes and showing stable properties in a broad temperature interval.

This study aimed at establishing the qualitative and quantitative characteristics of the heat release and absorption processes accompanying the martensite transformation in porous and nonporous titanium–nickel alloys.

The experiments were performed on the samples of cast and porous titanium–nickel alloys with a diameter of 6 mm and a height of 12 mm. The porous samples with an average pore size from 110 to 355 μm and the relative porosity varied from 26 to 72% were prepared by self-propagating high-temperature synthesis (SHS) as described elsewhere [4, 5]. The process of heat release and absorption in both cast and porous samples was studied differential thermal analysis (DTA). The DTA measurement procedure involves automated monitoring of the sample temperature and a temperature difference between the sample and standard. The standard must exhibit no phase transitions in the temperature interval studied and possess a heat capacity close to that of the sample. The sample structure was studied by X-ray diffraction on a DRON-3 diffractometer equipped with low- (KRN-190) and high-temperature (GPTV-1500) chambers. The temperature dependence of the sample resistivity was measured by a standard four-point-probe potentiometric technique.

It was experimentally established that the phase transitions in porous titanium–nickel alloys are characterized by an extended temperature interval of heat release (on cooling) and heat absorption (on heating). The total heat released and absorbed in a porous titanium–nickel alloy markedly exceeds that in the analogous cast alloy (Fig. 1). The maximum exothermal and endothermal effects are manifested in the samples with fine pores. These results are in agreement with features of the martensite transformation previously studied in porous titanium–nickel alloys, which showed evidence for a significantly extended temperature interval of the phase transitions. The presence of a broad temperature interval corresponding to the martensite transformation is also manifested in the temperature dependence of resistivity, which are strongly "smeared" for the porous samples (Fig. 2). The X-ray diffraction study of the phase composition and the calculation of a change in the volume fraction of the B19' martensite phase indicated that the martensite transformation in porous titanium–nickel alloys takes place in a brad temperature interval and is not completed, since only about 60% of the high-temperature B2 phase transforms into the low-temperature B19' martensite phase.

The X-ray diffraction measurements performed at various temperatures on our porous titanium–nickel

alloys (which are close in composition to the TN-10 cast alloy) [6], as well as the results obtained by electron microscopy, metallography, and electron-probe microanalysis, showed the presence of B2 phase at low temperatures. There is a broad temperature interval of coexistence of the B2 + B19' two-phase mixture containing Ti_2Ni, $TiNi_3$, and $Ti_4Ni_2O(N,H,C)$ components. The content of Ti_2Ni amounted to approximately 5–8% at all temperatures. The electron-microscopic examination of "massive" porous alloy domains also confirmed the presence of Ti_2Ni in the form of large spherical inclusions (with an average size of ~300 μm) and fine dispersed particles (~20 μm). The regions between pores contained needlelike crystalline precipitates of the B19' martensite phase.

The temperatures of phase transitions in titanium–nickel alloys are highly sensitive to the alloy composition. A change in the content of components in the homogeneity region shifts the phase transition onset temperatures by several tens of degrees [1]. It should be noted that preparation of the porous titanium–nickel alloy samples is affected by features of the SHS method. In particular, it is very difficult to provide for the conditions under which the fusion of Ti and Ni particles during the SHS process would lead to the formation of homogeneous (uniformly distributed) TiNi composition over the whole sample. The particles of $TiNi_3$ and $Ti_4Ni_2O(N,H,C)$ precipitates incorporated in the alloy structure lead to increased local stresses and plastic deformations both in the martensite crystals and in the B2 matrix phase (including the regions between pores). These precipitates also significantly affect the motion of interphase boundaries and shift the temperature interval of the martensite transformation.

Another important influence is related to the size factor, since the martensite transformation proceeds differently in thin regions between pores and in massive porous alloy domains. These reasons (inhomogeneous TiNi concentration distribution over a sample and the size factor) account for the phase transitions in various parts of the pore alloy structure proceeding at different temperatures. As a result, the hysteresis loop of the martensite transformation extends in the temperature axis, thus expanding the temperature intervals of the phase transitions as well as the shape memory effect and superelasticity manifestations. This is reflected by increasing temperature intervals of the heat release and absorption during these phase transitions. The degree of heating of a porous material may be several times that of an analogous cast TiNi alloy. The increasing degree of heating of the porous titanium–nickel alloys in comparison to the cast material is probably due to the fact that the regions between pores are in contact with a thermoinsulating medium (air) filling the pores and the rate of heat transfer from one pore wall to another is limited. In the cast alloys, the formation of differently oriented martensite plates results in an averaging of the
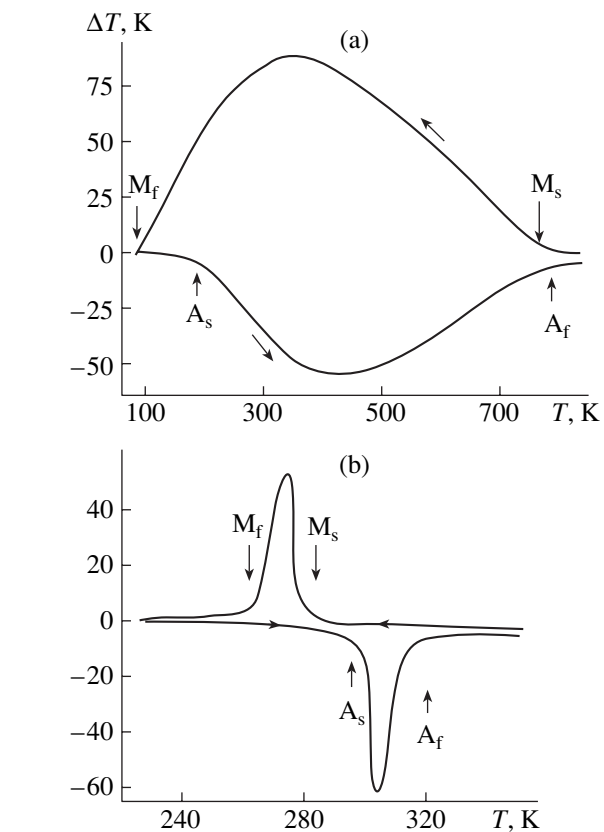

Fig. 1. DTA curves showing the heat release and absorption in (a) porous and (b) cast titanium–nickel alloys during martensite transformations (subscripts "s" and "f" indicate the martensite transformation start and finish, respectively).
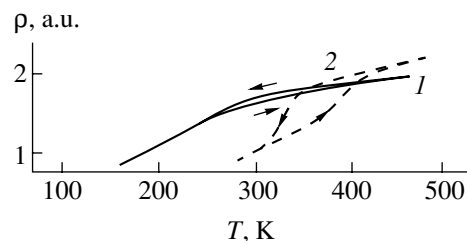

Fig. 2. Temperature dependence of the electric resistivity ρ of (*1*) porous and (*2*) cast titanium–nickel alloys (arrows indicate the direction of temperature variation).

heat release. Moreover, a part of such plates transforms into the high-temperature B2' phase as a result of the local heat supply. This increases the heat dissipation and reduces the overall level of heat release in the cast alloy sample.

Thus, the extended temperature interval of the phase transitions and increased level of the heat release and absorption during these transitions in porous titanium–nickel alloys in comparison to the analogous cast alloys is determined by the degree of porosity, the character of inhomogeneity of the porous alloy structure, and the width of the martensite transformation interval. This behavior of the porous TiNi alloys influences manifes-

tations of the shape memory effect in a broad temperature range and significantly affects the properties of articles and structures made of such porous alloys.

REFERENCES

1. V. É. Gyunter, G. Ts. Dambaev, P. G. Sysolyatin, *et al.*, *Medicinal Materials and Implants with Shape Memory* (Tomsk. Gos. Univ., Tomsk, 1998).

2. V. É. Gyunter, Yu. F. Yasenchuk, A. A. Klopotov, and V. N. Khodorenko, Pis'ma Zh. Tekh. Fiz. **26** (1), 71 (2000) [Tech. Phys. Lett. **26**, 35 (2000)].

3. V. É. Gyunter, Author's Abstract of Doctoral Dissertation in Technical Sciences (Tomsk, 1989).

4. V. I. Itin and Yu. S. Naĭborodenko, *High-Temperature Synthesis of Intermetallic Compounds* (Tomsk. Gos. Univ., Tomsk, 1989).

5. V. É. Gyunter, V. I. Itin, L. A. Monasevich, *et al.*, *Memory Effects and Their Applications in Medicine* (Nauka, Novosibirsk, 1992).

6. V. É. Gyunter, V. V. Kotenko, M. Z. Mirgazizov, *et al.*, *Alloys with Shape Memory in Medicine* (Tomsk. Gos. Univ., Tomsk, 1986).

Translated by P. Pozdeev

Liquid Phase Epitaxy of $(GaAs)_{1-x}(ZnSe)_x$ Solid Solution Layers from a Lead-Based Solution Melt

A. S. Saidov, A. Sh. Razzakov, and K. G. Gaimnazarov

Physical Engineering Institute, "Solar Physics" Research and Production Corporation,
Academy of Sciences of the Republic of Uzbekistan, Tashkent, Uzbekistan
e-mail: atvi@physic.ursci.net
Received July 2, 2001

Abstract—Epitaxial layers of $(GaAs)_{1-x}(ZnSe)_x$ solid solutions were grown from a tin-based solution melt confined between GaAs substrates. The solid solution layers were characterized with respect to composition, homogeneity, and some physical characteristics. © *2001 MAIK "Nauka/Interperiodica"*.

The rapid development of the micro- and optoelectronics stimulates the synthesis of new materials in the form of solid solutions, including those based on the $A^{III}B^V$ and $A^{II}B^{VI}$ compounds, the bandgap width and lattice constants of which may vary within certain limits. This possibility is important for increasing the range of useful electrical and photoelectrical characteristics, especially in the case of devices involving heterojunctions, where the maximum film–substrate lattice matching is of key significance.

A promising group of materials offering this possibility are the GaAs–ZnSe solid solutions characterized by a continuous mutual solubility of the components in both solid and liquid state [1]. While the lattice parameters of GaAs (5.65 Å) and ZnSe (5.653 Å), as well as their thermal expansion coefficients, are very close, their bandgap widths differ rather significantly ($E_{gGaAs} = 1.45$ eV versus $E_{gZnSe} = 2.67$ eV), which makes these solid solutions promising materials for optoelectronics.

Shevchenko *et al.* [2] studied the growth of $(GaAs)_x(ZnSe)_{1-x}$ solid solutions on ZnSe substrates from a gallium-based (Ga–As–Zn–Se) solution melt cooled at a rate of 5–7 K/min in a temperature range from 950 to 850°C. The thicknesses of epitaxial $(GaAs)_{1-x}(ZnSe)_x$ layers were 20–25 μm, while the bandgap width ranged within 1.41–2.0 eV. This was indicative of the formation of a transition layer from ZnSe to GaAs but did not provide unambiguous evidence for the existence of a true $(GaAs)_{1-x}(ZnSe)_x$ solid solution with $0 < x < 1$.

The main condition for a solid solution crystallization in the system studied is a high oversaturation with respect to three components in the crystallization front. This condition is met in the temperature interval from 850–860 to 750–760°C, selected based on the phase diagram of the Pb–GaAs—ZnSe system. The solution melt composition corresponding to this temperature

interval ensures the necessary oversaturation with respect to three components. If the process starts at a temperature of 870°C and terminates at 770°C, the melt will be oversaturated with respect to ZnSe and the epitaxy will begin at a large content of this component in the growing layer. Under these conditions, the layer structure will be imperfect because the content of ZnSe does not gradually vary with thickness so as to provide for a smooth matching between GaAs and ZnSe lattices. As a result, a large number of misfit dislocations is formed at the heterojunction and a part of these dislocations grow into the epitaxial layers. If the crystallization starts at 840°C and terminates at 740°C, the solution melt is unsaturated and the growth will be preceded by etching of the substrate. In this case, the growth starts inhomogeneously, in the form of islands. We performed special preliminary investigation aimed at finding the conditions favoring the growth of crystallographically perfect epitaxial layers of the solid solution.

Here, we report on the possibility of a low-temperature epitaxial process leading to the growth of the $(GaAs)_{1-x}(ZnSe)_x$ solid solution on GaAs substrates from a limited volume of a lead-based three-component (Zn–GaAs–Se) solution melt under conditions of forced cooling in the temperature range from 870 to 730°C. We obtained epitaxial layers with a thickness of 15–20 μm on (100)-oriented GaAs substrates with a diameter of 20 mm. Investigation of the scanning images obtained using the characteristic X-ray radiation of the $(GaAs)_{1-x}(ZnSe)_x$ solid solution confirmed homogeneity of the sample surface and showed the presence of Ga, As, Zn, and Se in the sample composition. An analysis of the sample surface with the aid of a Cameca microanalyzer showed the following elemental composition of the $(GaAs)_{1-x}(ZnSe)_x$ epitaxial layer (at. %): Ga, 47.5; As, 45.5; Se, 3.6; Zn, 3.4.

The crystal perfection of the epitaxial layers of $(GaAs)_{1-x}(ZnSe)_x$ grown as described above was studied by X-ray diffraction on a DRON-UM1 diffractome-

ter. These measurements were performed using specially grown thin (4–5 μm thick) epitaxial layers. The results of these measurements showed that, because of close values of the lattice parameters of GaAs and ZnSe, the X-ray diffraction peaks in the diffractograms are also very much alike. The absence of other peaks is evidence of a single-crystal structure of the epitaxial layers. An analysis of the results obtained for various samples showed that the crystal perfection of the epitaxial layers depends on the substrate arrangement in the growth apparatus. The epitaxial layers grown on the lower substrates are more perfect than those obtained on the upper substrates (when the gap between substrates increases to $h > 0.7$ mm). This is probably related to convective flows in the solution melt, which appear in the gravitational field due to a difference between the densities of solvent and solid solution.

In addition, we determined some electrical properties of the epitaxial layers, including resistivity, conductivity type, the Hall mobility, and the charge carrier concentration. At 77 K, $n = 1.72 \times 10^{19}$ cm^{-3}; $R_H = 3.63 \times 10^2$ cm^3/K; $\rho = 2.04 \times 10^{-2}$ Ω cm; $\mu_H = 1780$ cm^2/(V s). At 300 K, $n = 7.64 \times 10^{19}$ cm^{-3}; $R_H = 8.18 \times 10^{-2}$ cm^3/K; $\rho = 0.292 \times 10^{-3}$ Ω cm; $\mu_H = 27.9$ cm^2/(V s). The epitaxial films studied exhibit electron conductivity.

Thus, using the proposed method, it is possible to obtain relatively cheap variband epitaxial layers of a $(GaAs)_{1-x}(ZnSe)_x$ solid solution. Until now, such layers with variable bandgap width were not grown from lead-based solution melts. These $(GaAs)_{1-x}(ZnSe)_x$ heterostructures can be used in semiconductor devices.

REFERENCES

1. N. A. Goryunova and N. N. Fedorova, Fiz. Tverd. Tela (Leningrad) **1**, 344 (1959) [Sov. Phys. Solid State **1**, 307 (1959)].
2. E. G. Shevchenko *et al.*, Izv. Akad. Nauk SSSR, Neorg. Mater., No. 9, 35 (1973).

Translated by P. Pozdeev

Electric Field Induced Wavelike Instability in Smectic C Liquid Crystals

A. N. Chuvyrov and O. A. Denisova

Bashkir State University, Ufa, Bashkortostan, Russia
e-mail: ChuvyrovAN@bashedu.ru

Received July 3, 2001

Abstract—We studied 4-*p*-decyloxybenzoic acid 4'-*p*-hexyloxyphenyl ester liquid crystals of the smectic C (smC) type in which a wavelike instability is induced by an external electric field in the vicinity of the smC–smA phase transition. The smectic layers in a liquid-crystal sample placed in a sandwich type cell were parallel to the cell plates and the director was oriented at an angle θ to the layer normal. The second-order smC–smA phase transition exhibits a critical character. A wavelike instability in the form of a band structure was observed in both alternating and constant electric fields. The band structure period depends on the electric field strength. © *2001 MAIK "Nauka/Interperiodica".*

Smectic liquid crystals comprise a set of parallel layers freely moving relative to each other. Molecules in the layers can be oriented parallel to each other, making an arbitrary angle θ with the layer plane. Depending on the orientation of molecules, the liquid crystals are called smectic A (smA) for θ = 0 or smectic C (smC) for θ ≠ 0.

To our knowledge, the problem of a wavelike instability development in liquid crystals of the smA type was originally theoretically studied by Rapini [1] and later analyzed by Barratt and Duffy [2]. In smC* liquid crystals, the wavelike instability developed under the action of tensile stresses was considered by Jakli *et al.* [3]. Estimates of the instability threshold showed that this phenomenon is difficult to observe even in rather thick samples ($d = 10^{-2}$ m). For this reason, no experimental observations of the wavelike instability in external fields have been reported so far. For an external magnetic field, the threshold field strength $H_c^2 = 2\pi K_1/\chi_a \lambda d$ is determined by the magnetic permeability anisotropy χ_a and the parameter $\lambda = (K_1/C_{33})^{-\frac{1}{2}}$. In smA samples, the latter parameter is on the order of the layer thickness ($C_{33} \sim 10^4$ erg/cm³ and $K_1 \approx 10^{-6}$ erg/cm are the elastic moduli). To reduce the wavelike instability threshold, it is necessary to increase λ and χ_a or the liquid crystal layer thickness d, which is hardly possible in a real experiment.

Application of an external magnetic field to smA liquid crystals usually leads to another transition (the Parodi effect) related to the formation of a dislocation structure upon a change in the orientation of molecules [2]. Probably, an electric analog of this effect was described in [4]. Pikin [6] pointed out that analogous instabilities in the external fields can take place in smC as well, but no reliable experimental evidence of such behavior is available. However, liquid crystals of the smC type apparently allow the parameter λ to attain sufficiently large values in the vicinity of the smC–smA phase transition, provided that the system exhibits a critical behavior. Under these conditions, the phase transition must be formally analogous to the phase transition in liquid helium [5].

Let us estimate the value of λ in the vicinity of the smC–smA phase transition. With an allowance of the small elastic deformation, the thermodynamic potential of a smC liquid crystal is [5, 6]

$$F_c = \frac{1}{2}C_{33}\left(\frac{\partial U}{\partial z}\right)^2 + q\left(\frac{\partial U}{\partial z}\right)\theta^2 + a\theta^2 + c\theta^4, \quad (1)$$

where θ is the angle of molecular orientation in the smectic layer and U is the layer displacement. In the equilibrium state, this yields

$$\theta^2 = -C^{-1}\left(q\left(\frac{\partial U}{\partial z}\right) + a\right), \quad (2)$$

where $C \longrightarrow C^1[T_{CA} - T]^{\gamma - 2\beta}$ and $a \longrightarrow a^1[T_{CA} - T]^\gamma$ (β ≈ 0.35; γ ≈ 1.3) for the critical behavior of the system. Taking into account that $C_{33}^1 = \dfrac{\partial^2 F_c}{\partial U_{zz}^2}$, we obtain

$C_{33}^1 = C_{33}^0 - A(T_{CA} - T)^{-\gamma + 2\beta} \geq 0$, where $A = 2qC^{-1}$; thus, $C_{33}^1 \longrightarrow 0$ for $T \longrightarrow T_{CA}$ and, hence, $\lambda \longrightarrow \infty$.

Based on these considerations, we aimed at studying a wavelike instability induced by an external electric field in smC liquid crystals in the vicinity of the smC–smA second-order phase transition. The instability development was experimentally studied in a cell of the sandwich type with a liquid crystal confined
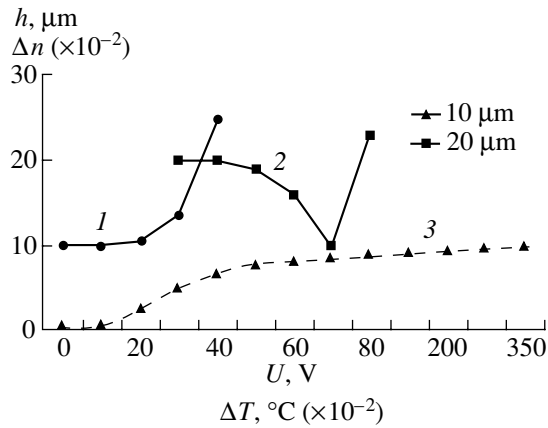
Fig. 1. Wavelike instability in smC liquid crystals: (*1, 2*) plots of the domain width *h* versus applied voltage *U* (for the liquid crystal layer thickness 10 and 20 μm, respectively); (*3*) birefringence *n* versus temperature difference *T*.
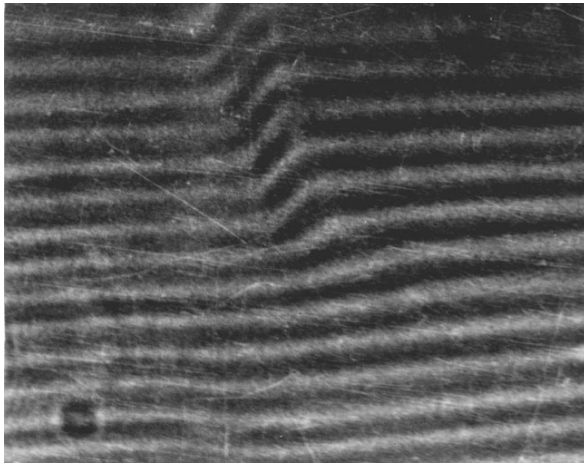

Fig. 2. The pattern of a wavelike instability in an smC liquid crystal, showing the formation of domains.

between glass plates coated from both sides with conducting tin dioxide (SnO$_2$) films. The smC liquid crystal placed between the plates was oriented so that the smectic layers were parallel to the cell plates. The director *C* was oriented at an angle θ to the vertical *OZ* axis (normal to the smectic layer).

The experiments were performed with 4-*p*-decyloxybenzoic acid 4'-*p*-hexyloxyphenyl ester (DOBA-HOPE) liquid crystals of the smC type characterized by the smC–smA phase transition temperature $T_{CA} = 62°C$. According to Eq. (2), the angle of orientation θ of the director *C* gradually decreases on approaching the phase transition point. Since the birefringence is $\Delta n = n_{\parallel} - n_{\perp} \approx \theta^2$, the temperature dependence presented in Fig. 1 shows that the smC–smA transition in DOBA-HOPE is a second-order phase transition possessing a critical character with $\gamma \approx 1.3$.

The wavelike instabilities having the form of a band structure with the wavevector parallel to the horizontal axis *OX* were observed in smC liquid crystals (DOBA-HOPE) exposed to both alternating and constant electric fields (Fig. 2). The band structure period varied with the field strength. An analysis of this dependence revealed a rather complicated pattern comprising three parts. In the fields having a small strength, the band period is independent (to within 10%) of the field and coincides with the liquid crystal thickness. As the field strength exceeds a certain critical level, the band period begins to decrease, passes through a minimum h_c, and then sharply grows with the field strength (Fig. 1).

The observed variation of the band structure period with the field strength can be qualitatively explained as follows. Let an electric field be applied perpendicularly to layers of an smC liquid crystal possessing a negative dielectric anisotropy ε_a. The field-induced reorientation of molecules leads to deformation of the layers and the formation of a modulated band structure [1]. In contrast to the case of an smA liquid crystal, the elastic energies of the modulated smC liquid crystal regions on the right and left sides of the domain axis are different (Fig. 1). At large deformations, molecules on the right side are oriented perpendicularly to the field; domains with this homogeneous orientation grow with increasing field strength. This corresponds to an increase in the band structure period at high voltages.

Let us evaluate dependence of the wavevector on the applied field strength. The free energy of an smC liquid crystal exposed to an external electric field can be expressed as [1]

$$F = \frac{1}{2}K_1\left(\frac{\partial^2 U}{\partial x^2}\right)^2 + \frac{1}{2}C'_{33}\left(\frac{\partial U}{\partial z}\right)^2$$
$$+ \varepsilon_a E^2\left[\cos\theta_0 - \sin\theta_0\left(\frac{\partial U}{\partial x}\right)\right]^2. \tag{3}$$

Using this expression, we obtain a relationship between the wavevector and the field strength:

$$q^4 + \frac{C'_{33}}{K_1}q_0^2 - q^2\frac{\varepsilon_a E^2}{K_1}\sin\theta_0 = 0.$$

According to this, a threshold for the wavelike structure formation corresponds to the critical field strength

$$E_c^2 = \frac{4C'_{33}}{3\varepsilon_a K_1}q_0\sin\theta_0.$$

For $q \approx q_0 = 2\pi/d$. In the vicinity of the smC–smA phase transition, $C'_{33} \longrightarrow 0$ and, hence, E_c acquires realistic values. This conclusion agrees with the experimental data presented in Fig. 1, where the wavevector near the threshold is $q_0 \approx 2\pi/d$ and the threshold voltage varies with the liquid crystal thickness as $U_c \approx \sqrt{d}$.

Thus, we have observed and studied a wavelike instability in smC liquid crystals. Apparently, the possibility of observing this phenomenon in liquid crystals of the DOBAHOPE type is related to the fact that the elastic modulus C_{33} of this medium decreases in the vicinity of the smC–smA phase transition, which leads to a decrease in the threshold voltage. This is consistent with the absence of a wavelike instability in smC liquid crystals of some alkoxybenzoic acids, where the smC–smA phase transformation is close to the first-order transition [4]. It should be noted that the wavelike instability observed in smC liquid crystals differs from that predicted for smA: at large deformations, an smC system features a homogeneous state, in contrast to a defect structure formed in smA [2].

REFERENCES

1. A. Rapini, J. Phys. (Paris) **33**, 237 (1972).
2. P. J. Barratt and B. R. Duffy, J. Phys. A **30**, 891 (1997).
3. A. Jakli, R. Bartolino, and N. Scaramuzza, J. Phys. (Paris) **50** (11), 1313 (1989).
4. P. de Gennes, *The Physics of Liquid Crystals* (Clarendon Press, Oxford, 1974; Mir, Moscow, 1977).
5. F. Pusnih, M. Schara, and M. Sentjure, J. Phys. (Paris) **36**, 665 (1975).
6. S. A. Pikin, *Structural Transformations in Liquid Crystals* (Nauka, Moscow, 1981; Gordon and Breach, New York, 1991).

Translated by P. Pozdeev

Information for Contributors

The journal *Pis'ma v Zhurnal Tekhnicheskoĭ Fiziki* (Technical Physics Letters) is devoted to various directions in general and applied physics. The journal is published semimonthly and is translated into English as *Technical Physics Letters* by the International Academic Publishing Company (IAPC) Nauka/Interperiodica. *Technical Physics Letters* is distributed abroad by the American Institute of Physics. The two versions, Russian and English, are issued simultaneously.

On submitting a manuscript to the editor, the authors thereby give to the Founders and Editorial Board the right to publish the Russian version and hand the manuscript to the IAPC to be translated and published in English. The authors retain all other rights as owners of the manuscript.

The manuscript should be accompanied by a copyright transfer statement letter in the following form:

We, undersigned as the authors,

… (full names of all authors)

hereby give the Founders and Editorial Board of the journal *Pis'ma v Zhurnal Tekhnicheskoĭ Fiziki*

the right to publish the paper entitled

… (full title)

in Russian and English.

We confirm that this publication does not interfere with the copyright of other persons or organizations.

Date …; Signature(s) …

The Editorial Board of the journal *Pis'ma v Zhurnal Tekhnicheskoĭ Fiziki* (*Technical Physics Letters*) asks contributors submitting their papers to obey the following rules. Manuscripts not conforming to these rules are not accepted for publication and are returned to the sender for revision. Then, the date of receipt will be when the revised version is received by the editor.

1. The manuscript should include a cover letter briefly explaining the need to urgently publish the paper in this particular journal.

The paper must be undersigned by all the authors. The accompanying material should contain the address, phone number (work and/or home), and e-mail of an author (hereinafter referred to as the author) to whom all correspondence from the editor should be sent.

2. The paper length should not typically exceed four standard (21×30-cm or $8^{1/2} \times 11$-in) double-spaced pages (plus the list of references and figure captions, both on separate sheets) and (typically) two figures.

Figures composed of separate independent parts should be avoided. The printed text should be neatly typed, employing a font size of 12 or 14 on white paper with double line spacing and ample margins. All pages should be sequentially numbered.

3. Sequentially arranged on the title sheet should be the following items:

Title

Initials and surnames of all the authors

Names (without abbreviations) and addresses (zip code, city, country, e-mail) of the institutions where the work was performed

Abstract (not exceeding one-third of a standard page)

4. The paper manuscripts and figures are to be submitted in duplicate. The figure size must not exceed the standard A4 page size and should contain the minimum necessary amount of details. Resolution of the computer-generated figures should be no worse than 600 dpi.

Half-tone figures (photographs) are to be submitted in duplicate as carefully prepared high-quality glossy prints; one copy must be provided with captions indicating the figure top, first author of the paper, and figure number. The figures should contain only notations using letters and numbers; all the necessary explanations should be given in the text or in the figure captions.

Tables should give the units of measure for all quantities.

5. Abbreviations, even conventional ones, should be avoided in the text and are unacceptable in the title, except for the formulas of complicated chemical compounds. The first use of an abbreviation in the text should be clearly explained.

6. The references must be numbered consecutively in order of appearance in the text and given in a separate list at the end of the text. References within the text are indicated by numbers in square brackets. The list of references must indicate the initials and surnames of all authors of the source cited (unless there are more than four; in this case, the third author's name is followed by *et al.*); for journals, the journal title (in the conventional abbreviated form), year, volume number, issue number, and pages (from first to last); for books, the full title, publisher, city, year of publication, and pages.

7. The author may submit a paper, in addition to the printed version, as a computer text file on diskette. The text of the paper should be written in an article LATEX2e style. All formulas must be written only using the standard TEX fonts of the Computer Modern (CM) family and the "msam" and "msbm" fonts of the American Mathematical Society (AMS).

8. An author from abroad may submit papers and accompanying material in English. The translation from English into Russian for publication in the Russian version of the Journal *Pis'ma v Zhurnal Tekhnicheskoĭ Fiziki* is executed by the Editorial Board and the Publisher.

9. If the paper is returned to the author for revision to take into account the referee's remarks and suggestions, the revised manuscript has to be returned to the editor within two months of the sending date. Otherwise, the date of first receipt is not mentioned and only the date of receiving the revised version is indicated.

10. Papers in English submitted for publication in the Journal *Pis'ma v Zhurnal Tekhnicheskoĭ Fiziki* (*Technical Physics Letters*) by authors from an English-speaking country (Great Britain, USA, Canada, New Zealand, Australia), or by an author participating in a collective work, are not subject to the style editing at the IAPC prior to publication in the *Technical Physics Letters* (Licensed Edition) unless the language quality is recognized as unacceptably poor.

11. Papers in English submitted for publication in the Journal *Pis'ma v Zhurnal Tekhnicheskoĭ Fiziki* (*Technical Physics Letters*) by authors who are not native speakers are subject to style editing at the IAPC. The proofs of all papers subjected to style editing at the IAPC are sent to the author for approval. The author has to return the proofs with necessary remarks to the editor within five days. After the elapse of the five-day period, the editor has the right to consider all changes in the paper as agreed and publish the edited paper.

12. When accepted, papers submitted in English are accompanied by the footnote: "This article was submitted by the author(s) in English."

13. The contributors are paid fees only for their publications appearing in English in the *Technical Physics Letters* (Licensed Journal).